University of Minho
School of Sciences

Francisco Ricardo Lobo Ribeiro

Excitonic properties of hBN from a time-dependent Hartree-Fock mean-field theory

august 2023

Excitonic properties of hBN from a time-dependent Hartree-Fock mean-field theory

Francisco Lobo

UMinho | 2023

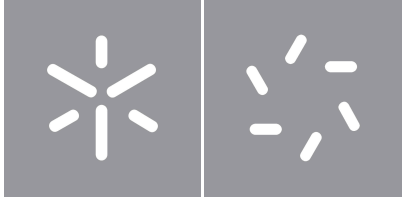

University of Minho
School of Sciences

Francisco Ricardo Lobo Ribeiro

Excitonic properties of hBN from a time-dependent Hartree-Fock mean-field theory

Masters Dissertation
Master's in Physics

Dissertation supervised by
Doctor Bruno Amorim
Doctor Nuno Peres

october 2023

Copyright and Terms of Use for Third Party Work

License granted to users of this work:

Acknowledgements

First and foremost, I show my appreciation to University of Minho, in particular to the Department of Physics, for the institutional support and, most importantly, for its amazing and kind professors who guided me not only through my Bachelor's and Master's degree, but also through life.

I would also like to express my gratitude towards my advisor Doctor Bruno Amorim and my co-advisor Doctor Nuno Peres. Both of them are, without a doubt, one of the best professors and mentors one could have. I thank them for their pedagogical, kind and friendly attitude and for the patience and support shown throughout the realization of this dissertation and also in the courses they taught me. I attribute much of my academic background, specifically in condensed matter physics, to them.

Lastly but not least, I'm grateful for my family and girlfriend Sofia who always have shown me their unconditional love. I thank my six month old nephew Tomás for accompanying the writing of the thesis and for useful discussions on exciton physics, i.e sleeping on my bed while I externalize thoughts whilst writing the dissertation. I specially thank my good friends and colleagues Marcelo Barreiro and Tiago Antão for all the great memories we lived together and for all the help and fruitful debates in our academic years.

This work was supported by Fundação para a Ciência e a Tecnologia, I.P., (FCT-Portugal) through project EXPL/FIS-MAC/0953/2021.

Fundação
para a Ciência
e a Tecnologia

Statement of Integrity

I hereby declare having conducted this academic work with integrity.

I confirm that I have not used plagiarism or any form of undue use of information or falsification of results along the process leading to its elaboration.

I further declare that I have fully acknowledged the Code of Ethical Conduct of the University of Minho.

University of Minho, Braga, october 2023

Assinado por: **Francisco Ricardo Lobo Ribeiro**
Num. de Identificação: 30286406
Data: 2023.11.03 20:12:33+00'00'

Francisco Ricardo Lobo Ribeiro

Abstract

In this work we perform a generic derivation on how collective excitations emerge from a many-body system of interacting particles within a time-dependent Hartree-Fock mean-field theory at zero-temperature. To this end, we study the linear response of the system's reduced density matrix in a many-body perturbation theory and demonstrate that it can be expressed in terms of a generalized eigen-problem of the effective two-particle Hamiltonian of the electron-hole interaction. We then specify this formalism for the case of a crystal system and an atomistic electron-electron interaction, structuring the generalized eigen-problem in terms of the Bloch momentum and spin degrees of freedom. At last, we apply this theory to the case of hexagon boron nitride structures in a nearest-neighbor tight-binding model for the electronic Bloch states. We then solve the generalized eigen-problem numerically and obtain the excitonic states energies and wave-functions. Also, we comment on the role of screening in the Hartree and Fock interaction, on the numerical details of the generalized eigen-problem and on the reliability of the Tamm-Dancoff approximation.

Keywords time-dependent, mean-field approximation, Hartree-Fock, screening, reduced density matrix, zero temperature, linear response, effective two-particle Hamiltonian, generalized eigen-problem, crystal, tight-binding model, exciton, hexagonal boron nitride

Resumo

Neste trabalho realizamos uma derivação genérica sobre como excitações colectivas emergem de um sistema de muitos-corpos de partículas interactuantes numa teoria de Hartree-Fock de campo médio dependente do tempo a temperatura zero. Para tal, estudamos a resposta linear da matriz de densidade reduzida do sistema numa teoria de perturbação de muitos-corpos e demonstramos que esta pode ser expressa em termos de um problema generalizado aos valores próprios do Hamiltoniano efetivo de duas partículas da interação eletrão-buraco. Em seguida, especificamos este formalismo para o caso de um sistema cristalino e de uma interação eletrão-eletrão atomística, estruturando o problema generalizado aos valores próprios em termos dos graus de liberdade do momento de Bloch e do spin. Por fim, aplicamos esta teoria ao caso de estruturas de nitreto de boro hexagonal num modelo de tight-binding ao vizinho mais próximo para os estados de Bloch electrónicos. Em seguida, resolvemos numericamente o problema generalizado aos valores próprios e obtemos as energias e as funções de onda dos estados excitónicos. Para além disso, comentamos também no papel da blindagem na interação de Hartree e de Fock, nos pormenores numéricos do problema aos valores próprios e na fiabilidade da aproximação de Tamm-Dancoff.

Palavras-chave dependente do tempo, aproximação de campo médio, Hartree-Fock, blindagem, matriz de densidade reduzida, temperatura zero, resposta linear, Hamiltonian efetivo de dois-partículas, model de tight-binding, problema generalizado aos valores próprios, cristais excitão, nitreto de boro hexagonal

Contents

Chapter 1

Introduction

1.1 Exciton basics

1.1.1 Definition and characterization

An exciton is a bound state of an electron and a hole, which are attracted to each other by the electrostatic force. Consider the semi-classical picture of an electron transitioning from a filled valence band to a vacant conduction band, either through the absorption of a photon or some another excitation method, in a two-band model of semiconductor crystal. After the electron is promoted, it leaves behind in the valence band a hole, an abstraction for the location from which the electron was moved, which all the remaining electrons will see as a positive charge. The negatively-charged electron in the conduction band and the positively-charged hole in the valence band are then electrostatically attracted to each other forming a neutral bound state [(1)]. Furthermore, the presence of the positively-charged hole in the electron filled valence band causes all of the electrons to begin to swarm the hole. However, since all these valence electrons will also interact with each other, the attraction felt for each individually electron to the hole will actually be screened. The electron in the conduction band is then less attracted to this hole due to the repulsive electric forces from large numbers of electrons surrounding the hole. These repulsive forces provide a stabilizing energy balance. Consequently, the exciton has slightly less energy than the unbound electron and hole pair [(2)].

Concerning the value of the binding energy and the spread of the wavefunction, excitons in condensed matter can be classified under different regimes, *Wannier-Mott* and *Frenkel* [(3)]. Wannier-Mott excitons capture the hydrogen-like nature of the electron–hole interaction in semiconductors where the coupling is delocalized over several unit cells of the real space lattice due to the high dielectric constant reducing the screening of the Coulomb interaction. It's description can be obtained through the Wannier equation which is essentially a Schrödinger equation with an effectively reduced mass of the electron-hole pair and

a modified (screened) potential. The other extreme is represented by *Frenkel* excitons, which correspond to a correlated electron-hole pair localized on a single lattice site and mostly prevail in organic materials.

1.1.2 Excitons in 2D materials

Exciton physics are especially relevant in two-dimensional (2D) materials, such as transition metal dichalcogenide (TMD) semiconductors or hexagonal boron nitrite (hBN). Their 2D nature leads to a reduced screening effect and thus to an enhanced Coulomb interaction, following the formation of more strongly bound excitons. In a cruder explanation, the screening is reduced because the electrostatic field lines that bound the electron and the hole are, for the most of it, within the vacuum outside the 2D semiconductor, resulting in a more weakly screened interaction compared to that of a bulk system. The suitable choice of the electrostatic potential to describe this 2D screening is known as the *Rytova-Keldish potential* [(4), (5)]. Although 2D material excitons cannot be genuinely described as either in the Wannier-Mott or Frenkel limit, being understood as an intermediate nature of both regimes, the Wannier-Mott description in the effective mass approximation appears to be largely appropriate even for quantitative prediction [(6)]. Furthermore, despite being a rather young research field, there is extensive research on exciton 2D physics and its application in optics and optoelectronics such as more efficient photo-voltaic cells, photo-detectors, valley-dependent optoelectronics and novel quantum coherent phases [(7), (8)]. Seek the articles [(9), (10)] for an in-deep review on 2D exciton physics and its applications.

1.1.3 Exciton coupling to light

Concerning the coupling of the excitons to light, we can classify the excitons as being either *bright* or *dark*. Bright excitons are associated to optically permitted transitions while dark excitons are associated to optically forbidden transitions. Bright excitons can form/recombine from a single photon absorption/emission, while dark excitons must also have some additional scattering (with other excitons, electron, phonons, defects, etc...) that can induce, for example, considerable changes in the exciton center of mass momentum [referring to non-vertical transition, as illustrated in Fig.(1)(a)] and/or spin flips [referring to spin-forbidden transition, as illustrated in Fig.(1)(b)]. Since dark excitons cannot recombine via direct emission of a photon, they have much longer radiative lifetimes than bright excitons. This highly stable non-radiative nature of dark excitons makes them attractive for many applications such as optically controlled information processing [(11), (12), (13)]. However, in order to eventually access the dark exciton's information, one needs first to make it respond to light. As compiled in the review article [(14)], some studies have attempted to this "brightening" of dark excitons in various ways. Regarding the "brightening"

of non-vertical transition dark excitons, the studies [(15), (16), (17), (18)] used near-field spectroscopy to induce a coupling to surface plasmon-polaritons such that the light dispersion "opens up", making optical transitions at lower frequencies accessible for non-zero center of mass momentum excitons. On the other hand, regarding the "brightening" of spin-forbidden transitions, the authors of [(19)] applied an in-plane magnetic field that does not perturb the material's electronic structure but can still alter the spin alignment of the carries, which relaxes the spin-selections rule and makes dark excitons optically detectable. With the dark exciton photoluminescence response effectively "switched" on, the probing of the (isolated) dark excitons dynamics is made possible, for example, by using strain to funnel the long-living dark excitons to the high-strain regions (while the bright excitons decay naturally during the funneling) such that they are the principal participants in drift and diffusion, as discussed in [(20), (21), (22)].

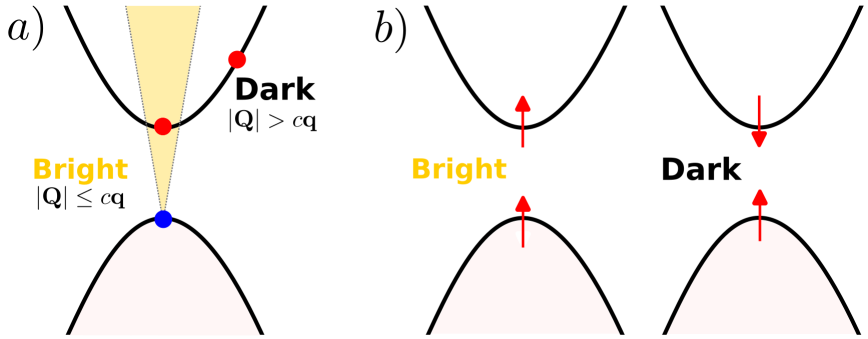

Figure 1: Schematic illustration of the optically allowed and forbidden electronic transitions in a two-band model for the bright and dark excitons concerning **(a)** the exciton center of mass momentum Q and **(b)** the spin of the electron. The electron is depicted in red, the hole in blue and the light dispersion cone in yellow. Note that, the occupied spin state in the valence band, corresponds to the spin of the electron that *originally* occupied the state, the spin of the hole would be its negative.

1.2 Collective excitations in a many-body system

We now make a short overview of some of the commonly used approaches to theoretically study excitonic physics and the main struggles of trying to account for the many-body electron interactions.

We start by mentioning the workhorse of ground-state mean-field electronic properties, known as *density-functional theory* (DFT), belonging to the family of first principles (ab initio) methods. DFT provides a way to map the many-body electron problem (where the electron-electron (e-e) interaction term couples the single-particle equations together) onto a single-body problem. This is done by considering the ground-state expectation value of some observable $\mathcal{O}$ as a function of the electron density $n(\boldsymbol{r})$. A successful

minimization of the energy functional will yield the ground-state density $n^{(0)}(\boldsymbol{r})$ and thus all others ground-state observables. First, one considers an energy functional that does not explicitly have an e-e interaction but has instead some other effective single-particle potential V_{s} that "bathes" the system and is felt by every electron individually. The corresponding system of Schrodinger's equations for the electrons wavefunction φ_i (where i denotes the electron) is know as the *Kohn-Sham* (KS) equations. This effective potential is generally composed of three terms: some applied external potential V, an Hartree term V_H describing the e-e Coulomb repulsion and an *exchange-correlation potential* V_{xc} introduced as mean to include all the many-body interactions that are otherwise not accounted for. Of course, the exact form of V_{xc} is not known and it must be approximated. Since both V_H and V_{xc} depend on $n(\boldsymbol{r})$, which depends on φ_i, which in turn depend on V_s, the problem of solving the KS equation has to be done in a self-consistent, iterative, way. Usually one starts with an initial guess for $n(\boldsymbol{r})$, then calculates the corresponding V_s and then solves the KS equations for the φ_i's. From these, one can calculate a new density and start all over again. This procedure is then repeated until convergence is reached.

There are, for example, several other ground-state mean-field approaches who use instead the (time-orded) single-particle Green's functions (GF) G as their building block, as apposed to the single-particle density in DFT. In this perturbation theory formalism, the broad strokes are still very similar: one obtains the non-interacting electron propagator G_0 in a mean field approximation and introduces a self-energy term Σ as basically a black box that contains all the unaccounted many-body interactions. Then, through the so called *Hedin's iterative scheme* depicted in Fig.(2) and a series of approximations, one can calculate G and, from there, obtain all the ground-state properties. Following Hedin's equations in Fig.(2), one of the most common approximations, known as the GW, makes the initial ansatz $\Sigma \approx 0$ such that $G \approx G_0$, leading to $\Gamma \approx 1$ which circles back to the self energy becoming $\Sigma = GW$ (hence the name). The corresponding screened potential W contains some of the effects of the dielectric screening (or polarization in a quantum chemist language) established by the rearrangement of the remaining electrons as a response to the removal of one of the electrons. As a follow-up approximation, one usually considers only a first-order perturbation theory with the self-energy reading $\Sigma = G_0W_0$.

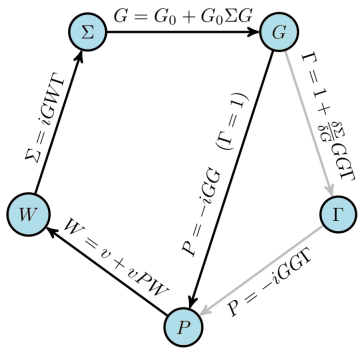

Figure 2: Hedin's iterative method composed of five, connected, integro-differential equation for the system's Green's function G, with G_0 its non-interacting counterpart, the irreducible vertex function Γ, the irreducible polarizability P, the screened Coulomb potential W and the self-energy Σ. The path made of black arrows shows the GW, process which bypasses the computation of Γ (gray arrows).

While DFT, GW and similar ground-state mean-field theories are extremely useful for ground-state properties they fail to attain the emergence of collective excitations from the residual interaction between the excited electron and the remaining hole. This should not surprise us since a variational mean-field theory is based on minimization [of the energy (at zero temperature) or of the free energy (at finite temperature)] and therefore it can only give reliable results for the quantities which we are minimizing. Since we are approximating a system of interacting particle to a system of independent particles, one would naively expect that a (mean-field) excited state could be obtained just by removing an electron from one of the occupied states $|o\rangle$ in the (mean-field) ground-state $|0\rangle_{\text{mf}}$, and promoting it to an empty state $|e\rangle$. Such excited state could then be written as $|e,o\rangle = c_e^\dagger c_o |0\rangle_{\text{mf}}$ and would have an energy equal to $\epsilon_e^{\text{mf}} - \epsilon_o^{\text{mf}} + E_0^{\text{mf}}$ with E_0^{mf} the (mean-field) ground-state energy. However this do not always apply since some states could have their energies bellow the quasi-particle (mean-field) bandgap. This is the case for excitons in insulators or plasmon-polaritons in metals. We emphasize that this inability in describing collective excitations is not a breakdown of mean-field theory, only of *ground-state* mean-field theory. If one instead describes the system using *time-dependent* mean-field theory this collective excitations do naturally emerge. Of course, there are other well established equivalent ways to describe this kind of collective excitation, for example via Configuration Interaction Singles (CIS), commonly employed in Quantum Chemistry, where we write the excited state as a linear combination $|X\rangle = \sum_{eo} \Psi_{eo}^X c_e^\dagger c_o |0\rangle_{\text{mf}}$ where Ψ_{eo}^X are the coefficients to be determined. As another example, one could obtain this kind of collective excitation via a time-dependent many-body perturbation theory, by resuming an infinite series of ladder and bubble (Feynman) diagrams in the two-particle propagator, which leads to the so called *Bethe-Salpeter equation* (BSE). Another possibility is using time-dependent Density Functional Theory (TD-DFT). For a comprehensive guide on all this for-

malism see [(23)]. In particular, if one is interested in pedagogical discussion of the BSE for a two-particle Green's function see also [(24)].

1.3 Thesis Structure

We perform a generic derivation on how the collective excitation of a many-body electron system are captured within a time-dependent Hartree-Fock mean-field theory for the special case of insulators at zero-temperature. We then apply this formalism to the case of a hBN isolated monolayer and a hBN-metal hetero-structure.

Specifically, in Sec.II, we introduce a general theoretical description of excitons. We start by considering a many-body system of electron described by an Hamiltonian expressed in second quantization containing a single-particle term H_0 and an interaction term H_{int} with a generic potential $V^{\alpha\beta}_{\gamma\delta}$ of symmetry $V(\boldsymbol{r} - \boldsymbol{r}') = V(\boldsymbol{r}' - \boldsymbol{r})$. We then perturb this system with a external applied force such that the equilibrium Hamiltonian is driven out-of-equilibrium. The perturbation Hamiltonian is described as a single-particle term coupled to the external force through some linear operator as usually done in linear response theory. From here, we study the time evolution of the system's reduced density matrix within a time-dependent Hartree-Fock mean-field scheme Then we expand the reduced density matrix in a power series and retain only first order term in order to study the system's linear response. This is done in the special case of an insulator at zero temperature such that the single-particle states can be described as being either occupied or empty. Finally, we show that the linear response can be obtained by solving instead a generalized eigenvalue problem for the effective two-particle (electron-hole) Hamiltonian $\boldsymbol{H}_{\text{e-h}}$.

Secondly, in Sec.III, we derive the specific form of $\boldsymbol{H}_{\text{e-h}}$. We start by specifying the focus on crystals systems and derive the explicit form of the potential $V^{\alpha\beta}_{\gamma\delta}$ for an atomistic e-e interaction written in a Bloch basis assuming ultra-localized Wannier functions. Using those results we then show the structure of the eigen-problem (still for an insulator at zero temperature) in the Bloch momentum degree of freedom and in the spin degree of freedom, commenting on the role of screening on the Hartree and Fock terms.

In Sec.IV we give an example on how to solve the generalized eigen-problem numerically, giving the broad strokes of said numerical implementation while discussing on some important details.

Finally, in Sec.V, we solve the generalized eigen-problem to the specific case of an isolated hBN monolayer and obtain its complete excitonic band structure and respective wave-functions. For this, we first show how to obtain the electronic single-particle Bloch states in a nearest-neighbor tight-binding model. We then consider the case of a hBN-metal hetero-structure in order to study the effects of (bulk) metal

screening on the excitonic energy levels.

Chapter 2

Theoretical description of excitons

2.1 Introduction to Linear Response Theory

All local physical measurements of a many-body system amount, in practice, to a process in which a *perturbation* is created by an applied external force, in the neighborhood of some point $\boldsymbol{r}'$ at some time t', and then the *response* of the system is measured at some other point $\boldsymbol{r}$ at some later time $t > t'$. Consider the case of a many-body system H which is *weakly* coupled to a one-particle external perturbation H_{ext} through some operator B such that the total system is described by $H = H + H_{\text{ext}}$. In first order perturbation theory, the expectation value of some local observable $A(\boldsymbol{r}, t)$ perturbed by the external force/source $F(\boldsymbol{r}, t)$ can be written as

$$\langle A(\boldsymbol{r}, t)\rangle = \langle A(\boldsymbol{r}, t)\rangle_0 - \int d\boldsymbol{r}' \int dt' \chi_{AB}\left(\boldsymbol{r}, t; \boldsymbol{r}', t'\right) F\left(\boldsymbol{r}', t'\right), \tag{2.1}$$

where $\langle A(\boldsymbol{r}, t)\rangle_0$ is the initial equilibrium expectation value and the "coefficient" of proportionality between the change in the expectation value and the force is the so called *generalized susceptibility.* On the other hand, the expectation value of $A(\boldsymbol{r}, t)$ in a given initial state $|\alpha\rangle$ of H, under the action of the weak perturbation H_{ext} is modified as $\langle A\rangle \equiv \langle\alpha| A |\alpha\rangle \to \langle\alpha| U^{-1} A U |\alpha\rangle$ where $U(t)$ is the evolution operator in the interaction representation of H_{tot}. By expanding $U(t)$ to first (linear) order in the perturbation H_{ext}, the change in the expectation value yields

$$\delta \langle A(\boldsymbol{r}, t)\rangle = \frac{i}{\hbar} \int_{-\infty}^{t} dt' \langle [H_{\text{ext}}(\boldsymbol{r}, t'), A(\boldsymbol{r}, t)]\rangle . \tag{2.2}$$

This expression is known as the *generalized Kubo formula.* From here we find that the general expression for the generalized susceptibility reads as

$$\chi_{AB}\left(\boldsymbol{r}, t; \boldsymbol{r}', t'\right) = -\frac{i}{\hbar}\Theta(t - t') \langle [A(\boldsymbol{r}, t), B(\boldsymbol{r}', t')]\rangle , \tag{2.3}$$

$$\overset{\mathcal{F}\text{ourier}}{\longrightarrow} \chi_{AB}\left(\boldsymbol{p}, \omega\right) = \frac{\langle A(\boldsymbol{p}, \omega)\rangle}{F(\boldsymbol{p}, \omega)} = \frac{\text{"response"}}{\text{"force"}}. \tag{2.4}$$

Therefore, if one can express and calculate the commutator $[A(\boldsymbol{r},t), B(\boldsymbol{r}',t')]$, the susceptibility in know and consequently the expectation value of A. However, this is not always such an easy task. In an alternative approach, one can always write a one-particle observable as

$$A = \sum_{ab} A_{ab} c_a c_b^\dagger \tag{2.5}$$

and consequently its expectation value as $\langle A \rangle = \sum_{ab} A_{ab} \left\langle c_a(t) c_b^\dagger(t) \right\rangle$. The last term is nothing more that the system's time-dependent one-particle reduced density matrix,

$$\rho_{ba}(t) = \left\langle c_a(t) c_b^\dagger(t) \right\rangle, \tag{2.6}$$

which can be obtained by solving its equation of motion in the Heisenberg picture of quantum mechanics. This is exactly the topic of this work. We show how formulate a time-dependent Hartree-Fock theory with the reduced density matrix as the central object.

2.2 Time-dependent Hartree-Fock mean-field theory

Consider a many-body system of electrons whose equilibrium state is described by the Hamiltonian H, written in an arbitrary electronic basis $\{\phi_\alpha\}$, as

$$H = H_0 + H_{\text{int}} = \sum_{\alpha\beta} h_{\alpha\beta} c_\alpha^\dagger c_\beta + \frac{1}{2} \sum_{\alpha\beta\gamma\delta} V_{\gamma\delta}^{\alpha\beta} c_\alpha^\dagger c_\beta^\dagger c_\gamma c_\delta, \tag{2.7}$$

where the operators $c_\alpha^\dagger$ (c_α) create (annihilate) an electron in the state described by the wavefunction $\phi_\alpha(\boldsymbol{r})$ with $\boldsymbol{r}$ the electron's positions vectors, and the greek indices are generic degrees of freedom that the system might have (momentum $\boldsymbol{k}$, band λ, spin σ, etc...). Also $h_{\alpha\beta}$ describes the single-particle matrix elements,

$$h_{\alpha\beta} = \int d^3\boldsymbol{r} \phi_\alpha^*(\boldsymbol{r}) \left[\frac{\boldsymbol{p}^2}{2m} + U(\boldsymbol{r}) \right] \phi_\beta(\boldsymbol{r}), \tag{2.8}$$

with $U(\boldsymbol{r})$ a generic static potential (for example a crystal lattice potential) and $V_{\gamma\delta}^{\alpha\beta}$ describes the two-particle interaction matrix elements,

$$V_{\gamma\delta}^{\alpha\beta} = \int d^3\boldsymbol{r} d^3\boldsymbol{r}' \phi_\alpha^*(\boldsymbol{r})\, \phi_\beta^*(\boldsymbol{r}') V(\boldsymbol{r} - \boldsymbol{r}') \phi_\gamma(\boldsymbol{r}') \phi_\delta(\boldsymbol{r}), \tag{2.9}$$

with $V(\boldsymbol{r})$ a generic electrostatic potential. As usual in electrostatic potentials, we assume that $V(\boldsymbol{r})$ has the symmetry $V(\boldsymbol{r} - \boldsymbol{r}') = V(\boldsymbol{r}' - \boldsymbol{r})$ and consequently the interaction matrix elements obey the symmetries

$$V_{\gamma\delta}^{\alpha\beta} = V_{\delta\gamma}^{\beta\alpha}, \tag{2.10}$$

$$\left(V_{\gamma\delta}^{\alpha\beta} \right)^* = V_{\alpha\beta}^{\gamma\delta}, \tag{2.11}$$

as shown in Appendix A.1. Consider now that we add a time-dependent perturbation to the system's equilibrium Hamiltonian, switched on at $t = t_0$, which is generally described by a one-particle term,

$$H_{\text{ext}} = \sum_{\alpha\beta} B_{\alpha\beta} c_\alpha^\dagger c_\beta F(t), \tag{2.12}$$

where $B_{\alpha\beta}$ are matrix elements of a one-particle operator which couples to the time-dependent external (force) field $F(t)$. This term will drive the system out-of-equilibrium by inducing transitions from a given state denoted by the degree of freedom β to another state α. Examples of perturbations can be the charge density coupled to a scalar potential, the current density coupled to a vector potential or the dipole moment coupled to an electric field. The Hamiltonian of the perturbed system reads

$$H(t) = \sum_{\alpha\beta} \left(h_{\alpha\beta} + B^i_{\alpha\beta} F^i(t) \right) c_\alpha^\dagger c_\beta + \frac{1}{2} \sum_{\alpha\beta\gamma\delta} V_{\gamma\delta}^{\alpha\beta} c_\alpha^\dagger c_\beta^\dagger c_\gamma c_\delta. \tag{2.13}$$

As discussed previously, in order to determine a specific property of a material, we can study its linear response to a given external perturbation by monitoring the time-evolution of the expectation value of a related one-particle observable,

$$A = \sum_{ab} A_{ab} c_a c_b^\dagger, \tag{2.14}$$

which in turn can be written in terms of the system's time-dependent reduced density matrix (rDM),

$$\rho_{ba}(t) = \left\langle c_a(t) c_b^\dagger(t) \right\rangle. \tag{2.15}$$

Our work is thus to study the time-evolution of the rDM, specifically in a time-dependent Hartree-Fock scheme. We start by its equation of motions written as

$$\frac{d}{dt}\rho_{ab}(t) = \frac{i}{\hbar} \left\langle \frac{dc_b^\dagger(t)}{dt} c_a(t) \right\rangle + \frac{i}{\hbar} \left\langle c_b^\dagger(t) \frac{dc_a(t)}{dt} \right\rangle, \tag{2.16}$$

where, in the Heisenberg picture of quantum mechanics, the fermionic operators evolve accordingly to the Heisenberg equation

$$\frac{d}{dt}\hat{\mathcal{O}}(t) = \frac{i}{\hbar}[H, \hat{\mathcal{O}}(t)]. \tag{2.17}$$

Therefore the rDM equation of motion reads

$$\frac{d}{dt}\rho_{ab}(t) = \frac{i}{\hbar} \left\langle [H, c_b^\dagger(t)] c_a(t) \right\rangle + \frac{i}{\hbar} \left\langle c_b^\dagger(t) [H, c_a(t)] \right\rangle. \tag{2.18}$$

As shown in Appendix A.2, given the equal-time fermionic anti-commutator properties $\left\{ c_a, c_b^\dagger \right\} = \left\{ c_b^\dagger, c_a \right\} = \delta_{ab}$ and $\{c_a, c_b\} = \left\{ c_b^\dagger, c_a^\dagger \right\} = 0$, each of the commutators are evaluated to

$$[H, c_b^\dagger] = \left(h_{\alpha b} + B^i_{\alpha b} F^i(t) \right) c_\alpha^\dagger + \frac{1}{2} V_{\gamma b}^{\alpha\beta} c_\alpha^\dagger c_\beta^\dagger c_\gamma - \frac{1}{2} V_{b\delta}^{\alpha\beta} c_\alpha^\dagger c_\beta^\dagger c_\delta, \tag{2.19}$$

$$[H, c_a] = -\left(h_{a\beta} + B^i_{a\beta} F^i(t) \right) c_\beta + \frac{1}{2} V_{\gamma\delta}^{\alpha a} c_\alpha^\dagger c_\gamma c_\delta - \frac{1}{2} V_{\gamma\delta}^{a\beta} c_\beta^\dagger c_\gamma c_\delta, \tag{2.20}$$

where we have hidden the summations on repeated indices using Einstein's notation and omitted the time dependency in the fermionic operators for compactness. This practice is done throughout the remaining work with no further mention. Substituting Eqs.(2.19) and (2.20) back into Eq.(2.18) yields

$$\begin{aligned}-i\hbar\frac{d}{dt}\rho_{ab}(t) = \rho_{a\alpha}(t)\left(h_{\alpha b} + B^i_{\alpha b}F^i(t)\right) - \left(h_{a\beta} + B^i_{a\beta}F^i(t)\right)\rho_{\beta b}(t) \\ + \frac{1}{2}V^{\alpha\beta}_{\gamma b}\left\langle c^\dagger_\alpha c^\dagger_\beta c_\gamma c_a\right\rangle - \frac{1}{2}V^{\alpha\beta}_{b\delta}\left\langle c^\dagger_\alpha c^\dagger_\beta c_\delta c_a\right\rangle \\ + \frac{1}{2}V^{\alpha a}_{\gamma\delta}\left\langle c^\dagger_b c^\dagger_\alpha c_\gamma c_\delta\right\rangle - \frac{1}{2}V^{a\beta}_{\gamma\delta}\left\langle c^\dagger_b c^\dagger_\beta c_\gamma c_\delta\right\rangle,\end{aligned} \tag{2.21}$$

where we came back to the definition of the rDM in Eq.(2.15) for the first two terms. Notice, however, that the remaining interaction terms correspond to the expectation values of four-operators. Dealing with such terms is no easy task and thus, to simplify our model, we introduce a mean-field approximation where we assume the two-particle expectation value to simply behave as a product of two one-particle expectation values. From this mean-field decoupling we can then make use of *Wick's theorem*. This is done for the first term of Eq.(2.21) and then we just show the results for the other three. We start by making all the possible two operator contractions from the four operators:

$$\left\langle c^\dagger_\alpha c^\dagger_\beta c_\gamma c_a\right\rangle = \left\langle \overbracket{c^\dagger_\alpha c^\dagger_\beta} \overbracket{c_\gamma c_a}\right\rangle + \left\langle \overbracket{c^\dagger_\alpha \overbracket{c^\dagger_\beta c_\gamma} c_a}\right\rangle + \left\langle \overbracket{c^\dagger_\alpha \overbracket{c^\dagger_\beta c_\gamma c_a}}\right\rangle \tag{2.22}$$

with

$$\left\langle \overbracket{c^\dagger_\alpha c^\dagger_\beta} \overbracket{c_\gamma c_a}\right\rangle = \left\langle c^\dagger_\alpha c^\dagger_\beta\right\rangle \langle c_\gamma c_a\rangle, \tag{2.23}$$

$$\left\langle \overbracket{c^\dagger_\alpha \overbracket{c^\dagger_\beta c_\gamma} c_a}\right\rangle = -\left\langle c^\dagger_\alpha c_\gamma\right\rangle \left\langle c^\dagger_\beta c_a\right\rangle, \tag{2.24}$$

$$\left\langle \overbracket{c^\dagger_\alpha \overbracket{c^\dagger_\beta c_\gamma c_a}}\right\rangle = \left\langle c^\dagger_\alpha c_a\right\rangle \left\langle c^\dagger_\beta c_\gamma\right\rangle, \tag{2.25}$$

where the minus sign in the second contraction appears directly from the anti-commutation of the fermionic operators (one could also check for the a minus sign by counting the n times the Wick's contraction line intersects: if n is odd number then there will be a negative sign). Notice that the first term is actually zero since, for non-superconducting systems, we must have that $\left\langle c^\dagger c^\dagger\right\rangle = \langle cc\rangle = 0$. Coming back once more to the definition of the rDM in Eq.(2.15), the first four-operator expectation value in Eq.(2.21) within the mean-field approximation read

$$\left\langle c^\dagger_\alpha c^\dagger_\beta c_\gamma c_a\right\rangle = -\rho_{\gamma\alpha}(t)\rho_{a\beta}(t) + \rho_{a\alpha}(t)\rho_{\gamma\beta}(t). \tag{2.26}$$

Following the same treatment, once can easily see that the remaining terms read

$$\left\langle c_\alpha^\dagger c_\beta^\dagger c_\delta c_a \right\rangle = -\rho_{\delta\alpha}(t)\rho_{a\beta}(t) + \rho_{a\alpha}(t)\rho_{\delta\beta}(t), \tag{2.27}$$

$$\left\langle c_b^\dagger c_\alpha^\dagger c_\gamma c_\delta \right\rangle = -\rho_{\gamma b}(t)\rho_{\delta\alpha}(t) + \rho_{\delta b}(t)\rho_{\gamma\alpha}(t), \tag{2.28}$$

$$\left\langle c_b^\dagger c_\beta^\dagger c_\gamma c_\delta \right\rangle = -\rho_{\gamma b}(t)\rho_{\delta\beta}(t) + \rho_{\delta b}(t)\rho_{\gamma\beta}(t). \tag{2.29}$$

Putting these terms back together into Eq.(2.21), playing around with mute indices and using the symmetry properties of the potential in Eqs.(2.10) and (2.11), we can rewrite the expression more compactly as

$$\begin{aligned} i\hbar\frac{d}{dt}\rho_{ab}(t) = &\left(h_{a\beta} + B^i_{a\beta}F^i(t)\right)\rho_{\beta b}(t) - \rho_{a\alpha}(t)\left(h_{\alpha b} + B^i_{\alpha b}F^i(t)\right) \\ &+ \left(V^{a\alpha}_{\delta\gamma} - V^{a\alpha}_{\gamma\delta}\right)\rho_{\delta\alpha}(t)\rho_{\gamma b}(t) - \rho_{a\beta}(t)\left(V^{\beta\alpha}_{\delta b} - V^{\alpha\beta}_{\delta b}\right)\rho_{\delta\alpha}(t). \end{aligned} \tag{2.30}$$

We now identify the Hartree and Fock self-energy terms respectively as

$$\Sigma^H_{a\gamma}[\rho(t)] = V^{a\alpha}_{\delta\gamma}\rho_{\delta\alpha}(t), \tag{2.31}$$

$$\Sigma^F_{a\gamma}[\rho(t)] = -W^{a\alpha}_{\gamma\delta}\rho_{\delta\alpha}(t), \tag{2.32}$$

such that the rDM equation of motion can be written in a time-dependent Hartree-Fock scheme as

$$\begin{aligned} i\hbar\frac{d}{dt}\rho_{ab}(t) = &\left(h_{a\beta} + B^i_{a\beta}F^i(t)\right)\rho_{\beta b}(t) - \rho_{a\alpha}(t)\left(h_{\alpha b} + B^i_{\alpha b}F^i(t)\right) \\ &+ \left(\Sigma^H_{a\gamma}[\rho(t)] + \Sigma^F_{a\gamma}[\rho(t)]\right)\rho_{\gamma b}(t) - \rho_{a\beta}(t)\left(\Sigma^H_{\beta b}[\rho(t)] + \Sigma^F_{\beta b}[\rho(t)]\right). \end{aligned} \tag{2.33}$$

This can be written in a more compact and elegant manner as

$$i\hbar\frac{d}{dt}\boldsymbol{\rho}(t) = [\boldsymbol{H}_{\text{HF}}, \boldsymbol{\rho}(t)] \tag{2.34}$$

$$\text{with} \quad \boldsymbol{H}_{\text{HF}} = \boldsymbol{h} + \boldsymbol{B}\cdot\boldsymbol{F}(t) + \boldsymbol{\Sigma}^H[\boldsymbol{\rho}(t)] + \boldsymbol{\Sigma}^F[\boldsymbol{\rho}(t)] \tag{2.35}$$

where $\boldsymbol{H}_{\text{HF}}$ is defined as the *Hartree-Fock Hamiltonian.*

Notice that we purposely defined the Fock self-energy term in Eq.(2.32) as an attractive interaction (by inserting the negative sign) such that it lower the total energy of the system enabling the formation of bound electron-hole states. Conversely, the Hartree self-energy term will control details of the excitation spectrum, such as spin-splitting (which will be discussed further in the text). Furthermore, while there is no apparent distinction between this two terms in the time-dependent density matrix Hartree-Fock formalism, in many-body perturbation theory the Hartree and Fock interactions are actually screened in different manners. Thus, forecasting this result, we write Eq.(2.32) instead with an W, symbolizing a screened interaction instead of the bare interaction denoted by V. Further ahead, when discussing two-particle

interactions in a many-body perturbation theory, we explain in more detail as to why this is the case. For now, and to put it vaguely, we do not also screen the Hartree interaction (as one would naively expect) because we would be accounting for the screening twice, in the sense that the Hartree interaction already "naturally" screens itself.

On another subject, in general, the Hamiltonian $\boldsymbol{h}$ already contains interaction at some kind of mean-field level. Therefore, it is reasonable to subtract this contribution for the self-energy terms,

$$\boldsymbol{\Sigma}^{H/F}[\boldsymbol{\rho}(t)] \to \boldsymbol{\Sigma}^{H/F}[\boldsymbol{\rho}(t) - \boldsymbol{\rho}^{(0)}]. \tag{2.36}$$

This would be equivalent to start from the Hamiltonian with the interacting part subtracted by the equilibrium mean field contribution from the interaction,

$$V^{\alpha\beta}_{\gamma\delta} c^\dagger_\alpha c^\dagger_\beta c_\gamma c_\delta \to V^{\alpha\beta}_{\gamma\delta} c^\dagger_\alpha c^\dagger_\beta c_\gamma c_\delta - (\Sigma^H_{\beta\gamma}\left[\rho^{(0)}\right] c^\dagger_\beta c_\gamma - \Sigma^F_{\beta\delta}\left[\rho^{(0)}\right] c^\dagger_\beta c_\delta. \tag{2.37}$$

2.3 Linear response theory

The rDM equation of motion as written in Eq.(2.33) would gives us the *full* response of the system to the external perturbation $F(t)$. However, very frequently, one is only interested in the case where the perturbation is weak and the system responds linearly to it. This is the so-called *linear response regime*. In linear response theory, as the name indicates, we only account for first (linear) order perturbations. Therefore, we start by expanding the rDM in a power series, $\boldsymbol{\rho}(t) = \boldsymbol{\rho}^{(0)} + \boldsymbol{\rho}^{(1)}(t) + \boldsymbol{\rho}^{(2)}(t) + ...$, and retain terms only up to the first order,

$$\boldsymbol{\rho}(t) \approx \boldsymbol{\rho}^{(0)} + \boldsymbol{\rho}^{(1)}(t). \tag{2.38}$$

Substituting Eq.(2.38) into Eq.(2.33), we see that in the linear regime most terms actually vanish: the terms $\left[\boldsymbol{B}\cdot\boldsymbol{F}(t), \boldsymbol{\rho}^{(1)}(t)\right]$ and $\left[\boldsymbol{\Sigma}^H[\boldsymbol{\rho}^{(1)}(t)] + \boldsymbol{\Sigma}^F[\boldsymbol{\rho}^{(1)}(t)], \boldsymbol{\rho}^{(1)}(t)\right]$ are neglected because they are of second order and the term $\left[\boldsymbol{h}, \boldsymbol{\rho}^{(0)}\right]$ is right away zero since the equilibrium rDM $\boldsymbol{\rho}^{(0)}$ is a function of occupation of the single-particle Hamiltonian $\boldsymbol{h}$. We are left with

$$\begin{aligned} i\hbar\frac{d}{dt}\rho^{(1)}_{ab}(t) - \left(h_{ac}\rho^{(1)}_{cb}(t) - \rho^{(1)}_{ac}t)h_{cb}\right) &= B^i_{ac}F^i(t)\rho^{(0)}_{cb} - \rho^{(0)}_{ac}B^i_{cb}F^i(t) \\ &+ \Sigma^H_{ac}[\rho^{(1)}(t)]\rho^{(0)}_{cb} - \rho^{(0)}_{ac}\Sigma^H_{cb}[\rho^{(1)}(t)] \\ &+ \Sigma^F_{ac}[\rho^{(1)}(t)]\rho^{(0)}_{cb} - \rho^{(0)}_{ac}\Sigma^F_{cb}[\rho^{(1)}(t)]. \end{aligned} \tag{2.39}$$

Next, we write the time-dependent force and the rDM as their Fourier counterpart

$$F(t) = \int \frac{d\omega}{2\pi} e^{-i\omega t} F(\omega), \tag{2.40}$$

$$\rho^{(1)}_{ab}(t) = \int \frac{d\omega}{2\pi} e^{-i\omega t} \rho^{(1)}_{ab}(\omega), \tag{2.41}$$

yielding the rDM equation of motion in terms of the frequency of the field ω,

$$\begin{aligned} \hbar\omega\rho^{(1)}_{ab}(\omega) - \left(h_{a\gamma}\rho^{(1)}_{\gamma b}(\omega) - \rho^{(1)}_{a\gamma}(\omega)h_{\gamma b}\right) &= B^i_{a\gamma}F^i(\omega)\rho^{(0)}_{\gamma b} - \rho^{(0)}_{a\gamma}B^i_{\gamma b}F^i(\omega) \\ &+ \Sigma^H_{a\gamma}[\rho^{(1)}(\omega)]\rho^{(0)}_{\gamma b} - \rho^{(0)}_{a\gamma}\Sigma^H_{\gamma b}[\rho^{(1)}(\omega)] \\ &+ \Sigma^F_{a\gamma}[\rho^{(1)}(\omega)]\rho^{(0)}_{\gamma b} - \rho^{(0)}_{a\gamma}\Sigma^F_{\gamma b}[\rho^{(1)}(\omega)]. \end{aligned} \tag{2.42}$$

Since, at linear order, the system response more aggressively at frequencies ω which are in resonance with the characteristic frequencies of the system, we try to rewrite the linear response as

$$\left(\hbar\omega\delta^{\gamma\delta}_{ab} - H^{\gamma\delta}_{ab}\right)\rho^{(1)}_{ab}(\omega) = J_{ab}(\omega). \tag{2.43}$$

with $H^{\gamma\delta}_{ab}$ the effective two-particle Hamiltonian and $J_{ab}(\omega)$ the source term. Specifically, we expect to obtain a free-particles term (where the two particle to not actually interact with each other), a Hartree term and a Fock term. Comparing Eq.(2.42) and Eq.(2.43), we can readily identify the non-interaction term as being

$$h_{a\gamma}\rho^{(1)}_{\gamma b}(\omega) - \rho^{(1)}_{a\gamma}(\omega)h_{\gamma b} = \sum_{\gamma\delta}\left(h_{a\gamma}\delta_{\delta b} - \delta_{a\gamma}h_{\delta b}\right)\rho^{(1)}_{\gamma\delta}(\omega), \tag{2.44}$$

and the source term as being

$$J_{ab}(\omega) = \left(B^i_{a\gamma}\rho^{(0)}_{\gamma b} - \rho^{(0)}_{a\gamma}B^i_{\gamma b}\right)F^i(\omega). \tag{2.45}$$

Although not so straight forward, after some minor play with mute indices while making use of the symmetry properties of the potential in Eqs.(2.10) and (2.11), the two-particle Hamiltonian can be identified as

$$H^{\gamma\delta}_{ab} = \left(h_{a\gamma}\delta_{\delta b} - \delta_{a\gamma}h_{\delta b}\right) + \left(V^{\delta a}_{\epsilon\gamma}\rho^{(0)}_{\epsilon b} - \rho^{(0)}_{a\epsilon}V^{\epsilon\delta}_{\gamma b}\right) - \left(W^{a\delta}_{\epsilon\gamma}\rho^{(0)}_{\epsilon b} - \rho^{(0)}_{a\epsilon}W^{\epsilon\delta}_{b\gamma}\right). \tag{2.46}$$

Furthermore, working in the basis that diagonalizes the single-particle Hamiltonian, we have that

$$h_{ac} = \epsilon_a\delta_{ac} \quad \text{and} \quad \rho^{(0)}_{ab} = f_a\delta_{ab}, \tag{2.47}$$

where ϵ_a is the occupational energy of the state a and $f_a = f(\epsilon_a)$ is the occupation of the state given by the Fermi-Dirac distribution. In this basis, the two-particle Hamiltonian in Eq.(2.46) simply reads

$$H^{\gamma\delta}_{ab} = \left(\epsilon_a - \epsilon_b\right)\delta_{a\gamma}\delta_{\delta b} + \left(f_b - f_a\right)\left(V^{\delta a}_{b\gamma} - W^{a\delta}_{b\gamma}\right). \tag{2.48}$$

Furthermore, the source term in Eq.(2.45) also simplifies to

$$J_{ab}(\omega) = \left(f_b - f_a\right)B^i_{ab}F^i(\omega). \tag{2.49}$$

2.3.1 Zero temperature regime

Consider the case of an insulator at absolute zero. Since at $T = 0K$ the Fermi-Dirac distribution behaves as a Heaviside theta function (centered at the Fermi energy), in the base that diagonalizes the single-particle Hamiltonian, the degrees of freedom can only be classified as either occupied $|o\rangle$ or empty $|e\rangle$ such that $f_o = 1$ or $f_e = 0$. In this regime, the Hamiltonian $H^{\gamma\delta}_{ab}$ has $2 \times 2 \times 2 \times 2 = 16$ blocks arising from all the different combination of $a \to o_1$ or e_1, $b \to o_2$ or e_2, $\gamma \to o_3$ or e_3 and $\delta \to o_4$ or e_4. Therefore, we can write Eq.(2.43) explicitly as

$$\left(\hbar\omega\mathbb{1} - \begin{bmatrix} H^{e_3e_4}_{e_1e_2} & H^{e_3o_4}_{e_1e_2} & H^{o_3e_4}_{e_1e_2} & H^{o_3o_4}_{e_1e_2} \\ H^{e_3e_4}_{e_1o_2} & H^{e_3o_4}_{e_1o_2} & H^{o_3e_4}_{e_1o_2} & H^{o_3o_4}_{e_1o_2} \\ H^{e_3e_4}_{o_1e_2} & H^{e_3o_4}_{o_1e_2} & H^{o_3e_4}_{o_1e_2} & H^{o_3o_4}_{o_1e_2} \\ H^{e_3e_4}_{o_1o_2} & H^{e_3o_4}_{o_1o_2} & H^{o_3e_4}_{o_1o_2} & H^{o_3o_4}_{o_1o_2} \end{bmatrix} \right) \begin{bmatrix} \rho^{(1)}_{e_3e_4}(\omega) \\ \rho^{(1)}_{e_3o_4}(\omega) \\ \rho^{(1)}_{o_3e_4}(\omega) \\ \rho^{(1)}_{o_3o_4}(\omega) \end{bmatrix} = \begin{bmatrix} \mathcal{J}_{e_1e_2}(\omega) \\ \mathcal{J}_{e_1o_2}(\omega) \\ \mathcal{J}_{o_1e_2}(\omega) \\ \mathcal{J}_{o_1o_2}(\omega) \end{bmatrix}, \tag{2.50}$$

where, in order to highlight the absolute zero regime, we introduced the notation $\boldsymbol{\mathcal{J}} = \boldsymbol{J}(T = 0)$. It is important to have in in mind that, although we are specifying a degree of freedom, there are other degrees of freedom still hidden away in the indices. That is why we formally referred to the Hamiltonian "entries" as being block matrices (and some an entry). Also, the dimensions of this blocks define the identity matrix $\mathbb{1}$ dimensions which was not yet specified (it is not just a 4×4 matrix). In this context, although the occupation function in this regime does really only have the two values, $f_o = 1$ or $f_e = 0$, the same is not true for the occupational energy ϵ, as it depends not only on the empty or occupied definition of the state but also on the other possible degree of freedom. From Eq.(2.48), we see that if a term has $a \neq \gamma$ or/and $\delta \neq b$ then the free-particles term is zero and if it has $a = b$ then its the interaction term that is zero. In addition, from Eq.(2.49), we see that the source terms with indices only in the occupied or the empty states vanish. We are left with

$$\left(\hbar\omega\mathbb{1} - \begin{bmatrix} H^{e_3e_4}_{e_1e_2} & 0 & 0 & 0 \\ H^{e_3e_4}_{e_1o_2} & H^{e_3o_4}_{e_1o_2} & H^{o_3e_4}_{e_1o_2} & H^{o_3o_4}_{e_1o_2} \\ H^{e_3e_4}_{o_1e_2} & H^{e_3o_4}_{o_1e_2} & H^{o_3e_4}_{o_1e_2} & H^{o_3o_4}_{o_1e_2} \\ 0 & 0 & 0 & H^{o_3o_4}_{o_1o_2} \end{bmatrix} \right) \begin{bmatrix} \rho^{(1)}_{e_3e_4}(\omega) \\ \rho^{(1)}_{e_3o_4}(\omega) \\ \rho^{(1)}_{o_3e_4}(\omega) \\ \rho^{(1)}_{o_3o_4}(\omega) \end{bmatrix} = \begin{bmatrix} 0 \\ \mathcal{J}_{e_1o_2}(\omega) \\ \mathcal{J}_{o_1e_2}(\omega) \\ 0 \end{bmatrix}. \tag{2.51}$$

Now, the first and last rows of the system of equations in Eq.(2.50) must have the trivial solution $\rho^{(1)}_{e_3e_4}(\omega) = \rho^{(1)}_{o_3o_4}(\omega) = 0$, and therefore, the linear response system reduces to

$$\left(\hbar\omega\mathbb{1} - \begin{bmatrix} H^{e_3o_4}_{e_1o_2} & H^{o_4e_3}_{e_1o_2} \\ H^{e_3o_4}_{o_2e_1} & H^{o_4e_3}_{o_2e_1} \end{bmatrix} \right) \begin{bmatrix} \rho^{(1)}_{e_3o_4}(\omega) \\ \rho^{(1)}_{o_4e_3}(\omega) \end{bmatrix} = \begin{bmatrix} \mathcal{J}_{e_1o_2}(\omega) \\ \mathcal{J}_{o_2e_1}(\omega) \end{bmatrix}, \tag{2.52}$$

where, since the electrons are indistinguishable and interchangeable, we renamed the indices $o_1e_2 \leftrightarrows o_2e_1$ and $o_3e_4 \leftrightarrows o_4e_3$. Recalling the symmetry properties of the potentials in Eqs.(2.10) and (2.11), one can find that the remaining Hamiltonian terms are actually related in the diagonal and in the off-diagonal. As derived in Appendix A.3, we find that $H^{o_4e_4}_{o_1e_2} = -\left(H^{e_3o_4}_{e_1o_2}\right)^*$ and $H^{e_4o_3}_{o_2e_1} = -\left(H^{o_3e_4}_{e_1o_2}\right)^\dagger$. The linear response yields

$$\left(\hbar\omega \begin{bmatrix} \mathbb{1} & 0 \\ 0 & -\mathbb{1} \end{bmatrix} - \begin{bmatrix} \boldsymbol{R} & \boldsymbol{C} \\ \boldsymbol{C}^\dagger & \boldsymbol{R}^* \end{bmatrix}\right) \begin{bmatrix} \boldsymbol{\rho}^{(1)}_{eo}(\omega) \\ \boldsymbol{\rho}^{(1)}_{oe}(\omega) \end{bmatrix} = \begin{bmatrix} \mathbb{1} & 0 \\ 0 & -\mathbb{1} \end{bmatrix} \begin{bmatrix} \boldsymbol{\mathcal{J}}_{eo}(\omega) \\ \boldsymbol{\mathcal{J}}_{oe}(\omega) \end{bmatrix}, \tag{2.53}$$

where we multiplied both side by the matrix with the identities blocks $\mathbb{1}$ and $-\mathbb{1}$ along its diagonal such that the two-particle Hamiltonian is written with all blocks having a positive sign (instead of having the minus signs in the bottom row). From Eq.(2.48), the two-particle Hamiltonian blocks are given respectively by

$$\boldsymbol{R} \equiv H^{e_3o_4}_{e_1o_2} = (\epsilon_{e_1} - \epsilon_{e_2})\,\delta_{e_1e_3}\delta_{o_4o_2} + \left(V^{o_4e_1}_{o_2e_3} - W^{e_1o_4}_{o_2e_3}\right), \tag{2.54}$$

$$\boldsymbol{C} \equiv H^{o_3e_4}_{e_1o_2} = \qquad 0 \qquad + \left(V^{e_4e_1}_{o_2o_3} - W^{e_1e_4}_{o_2o_3}\right). \tag{2.55}$$

At this point the effective two-particle electron-hole Hamiltonian, denoted from now on as $\boldsymbol{H}_{\text{e-h}}$, is usually referred as the *Bethe-Salpeter Hamiltonian* [(25)]. Let us take a look at the first row of the linear response in Eq.(2.53),

$$(\hbar\omega\mathbb{1} - \boldsymbol{R})\,\boldsymbol{\rho}^{(1)}_{eo}(\omega) - \boldsymbol{C}\boldsymbol{\rho}^{(1)}_{oe}(\omega) = \boldsymbol{\mathcal{J}}_{eo}(\omega)\mathbb{1}. \tag{2.56}$$

Consider that, initially, we have an electron in the valence band that, by the external source $\boldsymbol{\mathcal{J}}_{eo}(\omega)$, transitions to the conduction band, leaving behind a hole to whom it couples, effectively creating an exciton. However, although not so prominently, the reversed process, i.e the annihilation of the exciton by reemerging of the electron with its hole, can also occur due to $\boldsymbol{\mathcal{J}}_{oe}(\omega)$ (think of it as stimulated emission). This reversed process is described by the second row of the linear response in Eq.(2.53),

$$(\hbar\omega\mathbb{1} + \boldsymbol{R}^*)\,\boldsymbol{\rho}^{(1)}_{oe}(\omega) + \boldsymbol{C}^\dagger\boldsymbol{\rho}^{(1)}_{eo}(\omega) = \boldsymbol{\mathcal{J}}_{oe}(\omega)\mathbb{1}. \tag{2.57}$$

Moreover, notice that this processes are actually intertwined via the *coupling* block $\boldsymbol{C}$ (hence the name). As one could expect, the strength of the coupling of both processes is not so predominant when comparing it with the main contribution of the *resonant* term $\boldsymbol{R}$. As a common approximation, one could neglect the coupling block $\boldsymbol{C}$. This is the so called *Tamm-Dancoff approximation.* In due time, we will examine the reliability of such approximation.

Generalized susceptibility

We can compactly write the linear response problem in Eq.(2.53) as

$$(\hbar\omega \boldsymbol{S} - \boldsymbol{H}_{\text{e-h}})\, \boldsymbol{\rho}^{(1)}(\omega) = \boldsymbol{S}\boldsymbol{\mathcal{J}}(\omega), \tag{2.58}$$

with $\boldsymbol{S}$ being the matrix having the identities blocks $\mathbb{1}$ and $-\mathbb{1}$ diagonally across. Inverting the relation, the linear response yields

$$\boldsymbol{\rho}^{(1)}(\omega) = (\hbar\omega \boldsymbol{S} - \boldsymbol{H}_{\text{e-h}})^{-1}\, \boldsymbol{S}\boldsymbol{\mathcal{J}}(\omega). \tag{2.59}$$

One the other hand, the deviation of the expected value of some observable A, as written in Eq.(2.14), with respect to its equilibrium state$\langle A\rangle_0$), is given by

$$\langle A\rangle(\omega) = \sum_{ab} A_{ab}\rho^{(1)}_{ba}(\omega) = A_{oe}\rho^{(1)}_{oe}(\omega) + A_{eo}\rho^{(1)}_{eo}(\omega). \tag{2.60}$$

Since A_{ab} is a physical observable it is necessarily a real quantity, $A_{ba} = A^*_{ba}$ and thus, using Eq.(2.59), we can rewrite the expectation value instead as

$$\langle A\rangle(\omega) = \begin{bmatrix} A_{eo} & A_{oe} \end{bmatrix}^{\dagger} (\hbar\omega \boldsymbol{S} - \boldsymbol{H}_{\text{e-h}})^{-1}\, \boldsymbol{S} \begin{bmatrix} \mathcal{B}_{eo} \\ \mathcal{B}_{oe} \end{bmatrix} F(\omega), \tag{2.61}$$

where we unfolded the zero-temperature source term $\mathcal{J}(\omega)$ using Eq.(2.49) and denoted $\mathcal{B} = B(T = 0K)$. This way, comparing Eq.(2.61) with the generic expectation value $\langle A\rangle(\omega) = \chi_{AB}(\omega)F(\omega)$, it is easy to identify the generalized susceptibility as being

$$\chi_{A\mathcal{B}}(\omega) = \begin{bmatrix} A_{eo} & A_{oe} \end{bmatrix}^{\dagger} (\hbar\omega \boldsymbol{S} - \boldsymbol{H}_{\text{e-h}})^{-1}\, \boldsymbol{S} \begin{bmatrix} \mathcal{B}_{eo} \\ \mathcal{B}_{oe} \end{bmatrix}. \tag{2.62}$$

Linear response eigenvalue solution

Obtaining the linear response within this time-dependent Hartree-Fock scheme requires solving the linear problem in Eq.(2.58). One way this can be done is to solve first for the generic eigen-problem

$$(\hbar\omega \boldsymbol{S} - \boldsymbol{H}_{\text{e-h}}) \cdot \boldsymbol{\Psi}_\lambda = E_\lambda \boldsymbol{\Psi}. \tag{2.63}$$

Notice, however, although both $\boldsymbol{H}_{\text{e-h}}$ and $\boldsymbol{S}$ are Hermitian, the total matrix in the above eigen-problem is not. Therefore, one needs to solve instead for the eigen-problem

$$\boldsymbol{H}_{\text{e-h}} \cdot \boldsymbol{\Psi}_X = E_X \boldsymbol{S} \cdot \boldsymbol{\Psi}_X. \tag{2.64}$$

Only in this case does $\boldsymbol{\Psi}_X$ and E_X actually correspond to the collective excitations energies and respective wave-functions. The eigenvalues solution E_X will appear as a par of negative and positive energies with the same absolute value. In practice, solving this generalized eigen-problem must be done numerically. Said numerical implementation will be discussed in Sec.IV. Once we calculate the wave-functions $\boldsymbol{\Psi}_X$, we can expand the first-order rDM into its basis,

$$\boldsymbol{\rho}^{(1)}(\omega) = \sum_X a_X(\omega)\boldsymbol{\Psi}_X, \tag{2.65}$$

with a_X the coefficients to be determined of said expansion. Substituting Eq.(2.65) directly into Eq.(2.58) and contracting the result with $\boldsymbol{\Psi}^\dagger_{X'}$ yields

$$\sum_X a_X(\omega)\left(\hbar\omega - E_X\right)\boldsymbol{\Psi}^\dagger_{X'}\cdot\boldsymbol{S}\cdot\boldsymbol{\Psi}_X = \boldsymbol{\Psi}^\dagger_{X'}\cdot\boldsymbol{S}\cdot\boldsymbol{\mathcal{J}}(\omega). \tag{2.66}$$

Now, the generalized eigenvectors $\boldsymbol{\Psi}_X$ must satisfy the generalized orthogonality relation $\boldsymbol{\Psi}^\dagger_X\cdot\boldsymbol{S}\cdot\boldsymbol{\Psi}_{X'} = \text{sign}(E_X)\delta_{X,X'}$ where the sign function ensures that $\boldsymbol{H}_{\text{e-h}}$ is positive-defined (i.e, for the negative energy of the pair, $\text{sign}(E_X)E_X = |E_X|$). Using this orthogonality condition, we solve for the a_X coefficients we obtain

$$a_X(\omega) = \frac{\text{sign}(E_X)}{(\hbar\omega - E_X)}\boldsymbol{\Psi}^\dagger_X\cdot\boldsymbol{S}\cdot\boldsymbol{B}F(\omega). \tag{2.67}$$

Immediately, the first order rDM in Eq.(2.65) yields

$$\boldsymbol{\rho}^{(1)}(\omega) = \sum_X \boldsymbol{\Psi}_X\frac{\text{sign}(E_X)}{(\hbar\omega - E_X)}\boldsymbol{\Psi}_X\cdot\boldsymbol{S}\cdot\boldsymbol{B}F(\omega), \tag{2.68}$$

and therefore, the generalized susceptibility from Eq.(2.62) can be obtained through

$$\chi_{A\mathcal{B}}(\omega) = \begin{bmatrix} A_{eo} & A_{oe}\end{bmatrix}^\dagger\left(\sum_X\begin{bmatrix}\boldsymbol{\Psi}^X_{eo}\\ \boldsymbol{\Psi}^X_{oe}\end{bmatrix}\frac{\text{sign}(E_X)}{(\hbar\omega - E_X)}\begin{bmatrix}\boldsymbol{\Psi}^X_{eo} & \boldsymbol{\Psi}^X_{oe}\end{bmatrix}^\dagger\cdot\boldsymbol{S}\right)\begin{bmatrix}\mathcal{B}_{eo}\\ \mathcal{B}_{oe}\end{bmatrix}. \tag{2.69}$$

Chapter 3

Excitonic generalized eigen-problem in a crystal

In this section we derive the explicit form of the two-particle electron-hole Hamiltonian $\boldsymbol{H}_{\text{eh}}$ for crystals systems, therefore working in a Bloch states basis. We show how to obtain the explicit form of the potential $V^{\alpha\beta}_{\gamma\delta}$ for an atomistic electron-electron interaction written in a Bloch basis assuming ultra-localized Wannier functions. Using those results we then arrive at the structure of the eigen-problem for an insulator at zero temperature in the Bloch momentum degree of freedom. Furthermore, we also concern ourselves with the spin-structure of the eigen-problem and show that we can the problem can decoupled into a spin-singlet and a spin-triplet class of solutions. By the end of the section we discuss on the screening in the Hartree and Fock term.

3.1 Electron-electron atomistic interaction in the Bloch basis

Consider an electron-electron interaction within a crystal lattice written in second quantization as

$$H_{\text{e-e}} = \sum_{\substack{\boldsymbol{R}_1\boldsymbol{R}_2\\ \varsigma_1\varsigma_2}} \mathsf{V}\left((\boldsymbol{R}_1+\boldsymbol{s}_{\varsigma_1})-(\boldsymbol{R}_2+\boldsymbol{s}_{\varsigma_2})\right) c^\dagger_{\boldsymbol{R}_1\varsigma_1} c^\dagger_{\boldsymbol{R}_2\varsigma_2} c_{\boldsymbol{R}_2\varsigma_2} c_{\boldsymbol{R}_1\varsigma_1}, \tag{3.1}$$

where the operators $c^\dagger_{\boldsymbol{R}\varsigma}$ ($c_{\boldsymbol{R}\varsigma}$) create (annihilate) an electron in a given Bravais lattice site $\boldsymbol{R}$ in a given sub-lattice ς and V is some generic electrostatic potential. Foremost, we note that while we could have simply written $\boldsymbol{R} := \boldsymbol{R}+\boldsymbol{s}_\varsigma$, we make explicit the sub-lattice index as an anticipation to the work with hBN. Notice that, instead of carrying out the four different $\boldsymbol{R}$ indices, we assume that the electrons interact "atomistically" at large distances such that $\boldsymbol{R}_1$ is so very far out from $\boldsymbol{R}_2$ that, for all intents and purposes, the displacement of each electron on the real space lattice after the interaction is negligible, this is, that $\boldsymbol{R}_4,\varsigma_4 \approx \boldsymbol{R}_1,\varsigma_1$ and $\boldsymbol{R}_3,\varsigma_3 \approx \boldsymbol{R}_2,\varsigma_2$.

In order to express the e-e atomistic interaction in the Bloch basis we write the fermionic operators in

terms of the Bloch momentum in a given basis $\{\phi^{\varsigma}_{\boldsymbol{k}\lambda}\}$,

$$c_{\boldsymbol{R},\varsigma} = \frac{1}{\sqrt{N}} \sum_{\boldsymbol{k},\lambda} e^{i\boldsymbol{k}\cdot(\boldsymbol{R}+\boldsymbol{s}_{\varsigma})} \phi^{\varsigma}_{\boldsymbol{k}\lambda} c_{\boldsymbol{k}\lambda}, \tag{3.2}$$

where N is the number of primitive cells, $\boldsymbol{k}$ is the Bloch momentum degree of freedom and λ is the band-index, and the electrostatic potential V as it Fourier counterpart

$$\mathsf{V}(\boldsymbol{R}_1 + \boldsymbol{s}_{\varsigma_1}, \boldsymbol{R}_2 + \boldsymbol{s}_{\varsigma_2}) = \int \frac{d^D\boldsymbol{p}}{(2\pi)^D} e^{i\boldsymbol{p}\cdot(\boldsymbol{R}_1+\boldsymbol{s}_{\varsigma_1}-\boldsymbol{R}_2-\boldsymbol{s}_{\varsigma_2})} \mathsf{V}(\boldsymbol{p}), \tag{3.3}$$

with $D = 1, 2, ...$ being the system dimensions. Moreover, we write the Fourier reciprocal vector $\boldsymbol{p}$ as $\boldsymbol{p} = \boldsymbol{q} + \boldsymbol{G}$ with $\boldsymbol{q}$ being a vector that lays inside the first Brillouin zone (1BZ) and $\boldsymbol{G} = n_1\boldsymbol{b}_1 + n_2\boldsymbol{b}_2$ with n_1, $n_2 \in \mathbb{Z}$ a reciprocal lattice vector such that $\int d^D\boldsymbol{p} \to \sum_{\boldsymbol{G}} \int_{1\text{BZ}} d^D\boldsymbol{q}$. In this topic, we also introduce an Umklapp scattering curved bracket $\{\}$ notation indicating the translation of some momentum vector by the appropriate (and unique) reciprocal lattice vector such that it forces it back inside the 1BZ, for example, $\{\boldsymbol{p}\} = \boldsymbol{q}$. Substituting Eqs.(3.2) and (3.3) into Eq.(3.1) we obtain

$$\begin{aligned} H_{\text{e-e}} = \frac{1}{N^2} \sum_{\substack{\boldsymbol{R}_1\boldsymbol{R}_2 \\ \varsigma_1\varsigma_2}} \sum_{\substack{\boldsymbol{k}_1\boldsymbol{k}_2\boldsymbol{k}_3\boldsymbol{k}_4 \\ \lambda_1\lambda_2\lambda_3\lambda_4}} \sum_{\boldsymbol{G}} \int_{1\text{BZ}} \frac{d^D\boldsymbol{q}}{(2\pi)^D} \mathsf{V}(\boldsymbol{q}+\boldsymbol{G}) \\ \times e^{-i(\boldsymbol{k}_1-\boldsymbol{k}_4-\boldsymbol{q}-\boldsymbol{G})\cdot(\boldsymbol{R}_1+\boldsymbol{s}_{\varsigma_1})} e^{-i(\boldsymbol{k}_2-\boldsymbol{k}_3+\boldsymbol{q}+\boldsymbol{G})\cdot(\boldsymbol{R}_2+\boldsymbol{s}_{\varsigma_2})} \\ \times \left(\phi^{\varsigma_1}_{\boldsymbol{k}_1\lambda_1}\right)^* \left(\phi^{\varsigma_2}_{\boldsymbol{k}_2\lambda_2}\right)^* \phi^{\varsigma_2}_{\boldsymbol{k}_3\lambda_3} \phi^{\varsigma_1}_{\boldsymbol{k}_4\lambda_4} \\ \times c^{\dagger}_{\boldsymbol{k}_1\lambda_1} c^{\dagger}_{\boldsymbol{k}_2\lambda_2} c_{\boldsymbol{k}_3\lambda_3} c_{\boldsymbol{k}_4\lambda_4}, \end{aligned} \tag{3.4}$$

where the summation over $\boldsymbol{R}_1$ yields

$$\sum_{\boldsymbol{R}_1\varsigma_1} e^{-i(\boldsymbol{k}_1-\boldsymbol{k}_4-\boldsymbol{q}-\boldsymbol{G})\cdot(\boldsymbol{R}_1+\boldsymbol{s}_{\varsigma_1})} = \sum_{\varsigma_1} e^{-i(\boldsymbol{k}_1-\boldsymbol{k}_4-\boldsymbol{q}-\boldsymbol{G})\cdot\boldsymbol{s}_{\varsigma_1}} N\delta_{\boldsymbol{q},\{\boldsymbol{k}_1-\boldsymbol{k}_4\}}, \tag{3.5}$$

and the summation over $\boldsymbol{R}_2$ yields

$$\sum_{\boldsymbol{R}_2\varsigma_2} e^{-i(\boldsymbol{k}_2-\boldsymbol{k}_3+\boldsymbol{q}+\boldsymbol{G})\cdot(\boldsymbol{R}_2+\boldsymbol{s}_{\varsigma_2})} = \sum_{\varsigma_2} e^{-i(\boldsymbol{k}_2-\boldsymbol{k}_3+\boldsymbol{q}+\boldsymbol{G})\cdot\boldsymbol{s}_{\varsigma_2}} N\delta_{\boldsymbol{q},\{\boldsymbol{k}_3-\boldsymbol{k}_2\}}. \tag{3.6}$$

Substituting the summations results into Eq.(3.4) we further obtain

$$\begin{aligned} H_{\text{e-e}} = \sum_{\substack{\boldsymbol{k}_1\boldsymbol{k}_2\boldsymbol{k}_3\boldsymbol{k}_4 \\ \lambda_1\lambda_2\lambda_3\lambda_4}} \sum_{\boldsymbol{G}} \int_{1\text{BZ}} \frac{d^D\boldsymbol{q}}{(2\pi)^D} \mathsf{V}(\boldsymbol{q}+\boldsymbol{G}) \\ \times \sum_{\varsigma_1} e^{-i(\boldsymbol{k}_1-\boldsymbol{k}_4-\boldsymbol{q}-\boldsymbol{G})\cdot\boldsymbol{s}_{\varsigma_1}} \left(\phi^{\varsigma_1}_{\boldsymbol{k}_1\lambda_1}\right)^* \phi^{\varsigma_1}_{\boldsymbol{k}_4\lambda_4} \delta_{\boldsymbol{q},\{\boldsymbol{k}_1-\boldsymbol{k}_4\}} \\ \times \sum_{\varsigma_2} e^{-i(\boldsymbol{k}_2-\boldsymbol{k}_3+\boldsymbol{q}+\boldsymbol{G})\cdot\boldsymbol{s}_{\varsigma_2}} \left(\phi^{\varsigma_2}_{\boldsymbol{k}_2\lambda_2}\right)^* \phi^{\varsigma_2}_{\boldsymbol{k}_3\lambda_3} \delta_{\boldsymbol{q},\{\boldsymbol{k}_3-\boldsymbol{k}_2\}} \\ \times c^{\dagger}_{\boldsymbol{k}_1\lambda_1} c^{\dagger}_{\boldsymbol{k}_2\lambda_2} c_{\boldsymbol{k}_3\lambda_3} c_{\boldsymbol{k}_4\lambda_4}, \end{aligned} \tag{3.7}$$

allowing us to identify the density matrix elements, sometimes named *form factors*, as

$$\varrho_{\substack{\boldsymbol{k}\lambda \\ \boldsymbol{k}'\lambda'}}(\pm(\boldsymbol{q}+\boldsymbol{G})) = \sum_{\varsigma} e^{i(\boldsymbol{k}'-\boldsymbol{k}\pm(\boldsymbol{q}+\boldsymbol{G}))\cdot \boldsymbol{s}_{\varsigma}} \left(\phi^{\varsigma}_{\boldsymbol{k}\lambda}\right)^{*} \phi^{\varsigma}_{\boldsymbol{k}'\lambda'}. \tag{3.8}$$

Comparing the e-e interaction Hamiltonian $H_{\text{e-e}}$ in Eq.(3.7) with the generic H_{int} in Eq.(2.7), we can identity the general expression for the interaction potential matrix elements for an atomistic interaction written in term of Bloch states basis as

$$V^{\boldsymbol{k}_1\lambda_1,\boldsymbol{k}_2\lambda_2}_{\boldsymbol{k}_3\lambda_3,\boldsymbol{k}_4\lambda_4} = \frac{1}{\mathcal{V}}\sum_{\boldsymbol{G}}\int_{1\text{BZ}} \frac{d^D\boldsymbol{q}}{(2\pi)^D}\mathrm{V}(\boldsymbol{q}+\boldsymbol{G})\left(\varrho_{\substack{\boldsymbol{k}_1\lambda_1 \\ \boldsymbol{k}_4\lambda_4}}(\boldsymbol{q}+\boldsymbol{G})\,\varrho_{\substack{\boldsymbol{k}_2\lambda_2 \\ \boldsymbol{k}_3\lambda_3}}(-(\boldsymbol{q}+\boldsymbol{G}))\,\delta_{\boldsymbol{q},\{\boldsymbol{k}_1-\boldsymbol{k}_4\}}\delta_{\boldsymbol{q},\{\boldsymbol{k}_3-\boldsymbol{k}_2\}}\right), \tag{3.9}$$

where $\mathcal{V} = \mathcal{V}_{1\text{BZ}}/(2\pi)^D \times N$ is the real space crystal volume in D dimensions.

See that, through a diagrammatic analysis, the general features of his expression could have been guessed with some educated guesses. Looking at the Feynman diagram for this interaction shown in Fig.(3), we see the $\mathrm{V}(\boldsymbol{q}+\boldsymbol{G})$ potential depicted by the squiggly interaction line and the Kronecker deltas $\delta_{\boldsymbol{q},\{\boldsymbol{k}_1-\boldsymbol{k}_4\}}$ and $\delta_{\boldsymbol{q},\{\boldsymbol{k}_3-\boldsymbol{k}_2\}}$ forced by the conservation of momentum at each vertices, connecting electron $\boldsymbol{k}_1$, $\boldsymbol{k}_4$, $\boldsymbol{p}$ and $\boldsymbol{k}_2$, $\boldsymbol{k}_3$, $-\boldsymbol{p}$. The strength of the interaction at this vertices should then be modulated by the density of the participant particles, built from the electronic wave-functions $\phi^{\varsigma}_{\boldsymbol{k}\lambda}$.

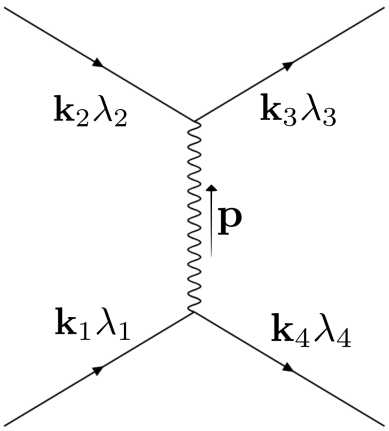

Figure 3: Feynman diagram of the electron-electron interaction in Eq.(3.9).

3.1.1 General electron-electron interaction

For a more complete description of the e-e interaction one must always use the general expression in terms of the electronic Bloch states $\{\psi_{\boldsymbol{k}\lambda}(\boldsymbol{r})\}$ of the density matrix elements,

$$\varrho_{\substack{\boldsymbol{k}\lambda \\ \boldsymbol{k}'\lambda'}}(\boldsymbol{q}+\boldsymbol{G}) = \int d^D\boldsymbol{r}\, e^{i(\boldsymbol{q}+\boldsymbol{G})\cdot\boldsymbol{r}}\psi^{*}_{\boldsymbol{k}\lambda}(\boldsymbol{r})\psi_{\boldsymbol{k}'\lambda'}(\boldsymbol{r}), \tag{3.10}$$

with $\boldsymbol{r}$ the generic position of the electron, i.e $\boldsymbol{r} = \boldsymbol{R} + \boldsymbol{s}_\varsigma + \boldsymbol{r}_{\text{WS}}$ with $\boldsymbol{r}_{\text{WS}}$ the position within the Wigner-Seitz unit cell. As a matter of fact, the atomistic interaction approximation used in our model can be obtained directly from the general expression if one expresses the Bloch states in a Wannier basis $\{w_\varsigma\}$,

$$\psi_{\boldsymbol{k}\lambda}(\boldsymbol{r}) = \frac{1}{\sqrt{N}} \sum_{\boldsymbol{R},\varsigma} e^{i\boldsymbol{k}\cdot(\boldsymbol{R}+\boldsymbol{s}_\varsigma)} \phi^\varsigma_{\boldsymbol{k}\lambda} w_\varsigma(\boldsymbol{r} - \boldsymbol{R} - \boldsymbol{s}_\varsigma), \tag{3.11}$$

and assumes *ultra-localized orbitals* by forcefully introducing the Kronecker delta terms $\delta_{\boldsymbol{R}\boldsymbol{R}'}$ and $\delta_{\varsigma\varsigma'}$. Substituting Eq.(3.11) directly into Eq.(3.10), within this ultra-localized regime, we obtain

$$\varrho_{\substack{\boldsymbol{k}\lambda \\ \boldsymbol{k}'\lambda'}}(\boldsymbol{q}+\boldsymbol{G}) \approx \sum_\varsigma e^{-i(\boldsymbol{k}'-\boldsymbol{k}+(\boldsymbol{q}+\boldsymbol{G}))\cdot\boldsymbol{s}_\varsigma} \left(\phi^\varsigma_{\boldsymbol{k}\lambda}\right)^* \phi^\varsigma_{\boldsymbol{k}'\lambda'} \varrho_{\substack{\boldsymbol{0}\boldsymbol{0} \\ \varsigma\varsigma'}}(\boldsymbol{q}+\boldsymbol{G}) \tag{3.12}$$

$$\text{with} \qquad \varrho_{\substack{\boldsymbol{R}\boldsymbol{R}' \\ \varsigma\varsigma'}}(\boldsymbol{q}+\boldsymbol{G}) = \int d^D\boldsymbol{r} e^{i(\boldsymbol{q}+\boldsymbol{G})\cdot\boldsymbol{r}} w^*_\varsigma(\boldsymbol{r} - \boldsymbol{R} - \boldsymbol{s}_\varsigma) w_\varsigma(\boldsymbol{r} - \boldsymbol{R}' - \boldsymbol{s}_{\varsigma'}). \tag{3.13}$$

Setting $\varrho_{\substack{\boldsymbol{0}\boldsymbol{0} \\ \varsigma\varsigma'}}(\boldsymbol{q}+\boldsymbol{G}) = 1$ yields the same result in Eq.(3.8) of our atomistic model.

3.2 Structure of eigen-problem in the Bloch momentum degree of freedom

Consider an electron of momentum $\boldsymbol{k}$ in a fully occupied valence band v with energy $\epsilon_{\boldsymbol{k},v}$ that, by the perturbation of an externally applied electric field, transitions to the empty conduction band c with momentum $\boldsymbol{k}+\boldsymbol{Q}$, with $\boldsymbol{Q}$ being the center of mass momentum of the exciton, having now energy $\epsilon_{\{\boldsymbol{k}+\boldsymbol{Q}\}c}$. Note that, in this two-band model, the occupied state corresponds to the valence band index, $o \to v$, and the empty state corresponds to valence band index, $e \to c$. As it turns out, this two-band model is sufficient to describe excitons in hBN, due to the simplicity of its electronic band structure. However, this is not always the case, since in most TMD at least a three band model is necessary [(26)]. The source term that described such perturbation is

$$\mathcal{J}_{\{\boldsymbol{k}+\boldsymbol{Q}\}c_1,\boldsymbol{k}v_2}(\omega, \boldsymbol{Q}+\boldsymbol{G}). \tag{3.14}$$

Accounting for the Bloch momentum degree of freedom, the linear response in Eq.(2.53) would read

$$\sum_{\boldsymbol{k}_3\boldsymbol{k}_4} \left(\hbar\omega \boldsymbol{S} - \begin{bmatrix} H^{\boldsymbol{k}_3c_3,\boldsymbol{k}_4v_4}_{\{\boldsymbol{k}+\boldsymbol{Q}\}c_1,\boldsymbol{k}v_2} & H^{\boldsymbol{k}_3v_3,\boldsymbol{k}_4c_4}_{\{\boldsymbol{k}+\boldsymbol{Q}\}c_1,\boldsymbol{k}v_2} \\ \left(H^{\boldsymbol{k}_3v_3,\boldsymbol{k}_4c_4}_{\{\boldsymbol{k}+\boldsymbol{Q}\}c_1,\boldsymbol{k}v_2}\right)^\dagger & \left(H^{\boldsymbol{k}_3c_3,\boldsymbol{k}_4v_4}_{\{\boldsymbol{k}+\boldsymbol{Q}\}c_1,\boldsymbol{k}v_2}\right)^* \end{bmatrix} \right) \begin{bmatrix} \rho^{(1)}_{\boldsymbol{k}_3c_3,\boldsymbol{k}_4v_4}(\omega) \\ \rho^{(1)}_{\boldsymbol{k}_3v_3,\boldsymbol{k}_4c_4}(\omega) \end{bmatrix} = \boldsymbol{S} \begin{bmatrix} \mathcal{J}_{\{\boldsymbol{k}+\boldsymbol{Q}\}c_1,\boldsymbol{k}v_2}(\omega) \\ \mathcal{J}_{\boldsymbol{k}v_1,\{\boldsymbol{k}+\boldsymbol{Q}\}c_2}(\omega) \end{bmatrix}, \tag{3.15}$$

where the summation over the momentum $\boldsymbol{k}_3$ and $\boldsymbol{k}_4$ accounts for all the possible different interactions (although, technically, it should have been an integral in the thermodynamic limit). This interaction must,

of course, conserve momentum as imposed by the Kronecker deltas in Eq.(3.9) or by the diagrammatics in Fig.(4). For instance, looking at the Hartree term in Fig.(4)(c) we see that the virtual transferred momentum $\boldsymbol{q}$ must read $\boldsymbol{q}=\boldsymbol{Q}+\boldsymbol{G}$ while for the Fock term in Fig.(4)(b) must read instead $\boldsymbol{q}=\{\boldsymbol{k}-\boldsymbol{k}'\}+\boldsymbol{G}$, where we rewrote $\boldsymbol{k}_4\to\boldsymbol{k}'$. Therefore, the linear response yields

$$\sum_{\boldsymbol{k}'}\left(\hbar\omega\boldsymbol{S}-\begin{bmatrix}\boldsymbol{R}(\boldsymbol{Q}) & \boldsymbol{C}(\boldsymbol{Q})\\ \boldsymbol{C}(\boldsymbol{Q})^{\dagger} & \boldsymbol{R}^{*}(\boldsymbol{Q})\end{bmatrix}\right)\begin{bmatrix}\boldsymbol{\rho}^{(1)}_{\{\boldsymbol{k}'+\boldsymbol{Q}\}c_3\boldsymbol{k}'v_4}(\omega)\\ \boldsymbol{\rho}^{(1)}_{\{\boldsymbol{k}'+\boldsymbol{Q}\}v_3\boldsymbol{k}'c_4}(\omega)\end{bmatrix}=\boldsymbol{S}\begin{bmatrix}\mathcal{J}_{\{\boldsymbol{k}+\boldsymbol{Q}\}c_1,\boldsymbol{k}v_2}(\omega,\boldsymbol{q}+\boldsymbol{G})\\ \mathcal{J}_{\boldsymbol{k}v_1,\{\boldsymbol{k}+\boldsymbol{Q}\}c_2}(\omega,\boldsymbol{q}+\boldsymbol{G}))\end{bmatrix}, \tag{3.16}$$

where the resonant block is given by

$$\boldsymbol{R}(\boldsymbol{Q})=H^{\{\boldsymbol{k}'+\boldsymbol{Q}\}c_3,\boldsymbol{k}'v_4}_{\{\boldsymbol{k}+\boldsymbol{Q}\}c_1,\boldsymbol{k}v_2}=\left(\epsilon_{\{\boldsymbol{k}+\boldsymbol{Q}\}c_1}-\epsilon_{\boldsymbol{k}v_2}\right)\delta_{\{\boldsymbol{k}+\boldsymbol{Q}\}c_1,\{\boldsymbol{k}'+\boldsymbol{Q}\}c_3}\delta_{\boldsymbol{k}v_2,\boldsymbol{k}'v_4}+\left(V^{\boldsymbol{k}'v_4,\{\boldsymbol{k}+\boldsymbol{Q}\}c_1}_{\boldsymbol{k}v_2,\{\boldsymbol{k}'+\boldsymbol{Q}\}c_3}-W^{\{\boldsymbol{k}+\boldsymbol{Q}\}c_1,\boldsymbol{k}'v_4}_{\boldsymbol{k}v_2,\{\boldsymbol{k}'+\boldsymbol{Q}\}c_3}\right), \tag{3.17}$$

and the coupling block by

$$\boldsymbol{C}(\boldsymbol{Q})=H^{\{\boldsymbol{k}'+\boldsymbol{Q}\}v_3,\boldsymbol{k}'c_4}_{\{\boldsymbol{k}+\boldsymbol{Q}\}c_1,\boldsymbol{k}v_2}=V^{\boldsymbol{k}'c_4,\{\boldsymbol{k}+\boldsymbol{Q}\}c_1}_{\boldsymbol{k}v_2,\{\boldsymbol{k}'+\boldsymbol{Q}\}v_3}-W^{\{\boldsymbol{k}+\boldsymbol{Q}\}c_1,\boldsymbol{k}'c_4}_{\boldsymbol{k}v_2,\{\boldsymbol{k}'+\boldsymbol{Q}\}v_3}. \tag{3.18}$$

We note that formally we should have made explicit composite indices $\boldsymbol{k}c_1v_1;\boldsymbol{k}'c_3v_4$ in the resonant and coupling blocks but abstained to do so for the sake of space and tidiness. Finally, using the general expressions in Eqs.(3.9) and (3.8), we can explicitly show the interaction terms in either the resonant and coupling block. The resonant Hartree term yields

$$V^{\boldsymbol{k}'v_4,\{\boldsymbol{k}+\boldsymbol{Q}\}c_1}_{\boldsymbol{k}v_2,\{\boldsymbol{k}'+\boldsymbol{Q}\}c_3}=\frac{1}{\mathcal{V}}\sum_{\boldsymbol{G}}\mathsf{V}(\boldsymbol{Q}+\boldsymbol{G})\left[\varrho_{\substack{\{\boldsymbol{k}+\boldsymbol{Q}\}c_1\\ \boldsymbol{k}v_2}}(\boldsymbol{Q}+\boldsymbol{G})\right]\left[\varrho_{\substack{\boldsymbol{k}'v_4\\ \{\boldsymbol{k}'+\boldsymbol{Q}\}c_3}}(-(\boldsymbol{Q}+\boldsymbol{G}))\right] \tag{3.19}$$

$$\text{with,}\qquad \varrho_{\substack{\{\boldsymbol{k}+\boldsymbol{Q}\}c_1\\ \boldsymbol{k}v_2}}(\boldsymbol{Q}+\boldsymbol{G})=\sum_{\varsigma}e^{i(\boldsymbol{k}-\{\boldsymbol{k}+\boldsymbol{Q}\}+(\boldsymbol{Q}+\boldsymbol{G}))\cdot\boldsymbol{s}_{\varsigma}}\left(\phi^{\varsigma}_{\{\boldsymbol{k}+\boldsymbol{Q}\}c_1}\right)^{*}\phi^{\varsigma}_{\boldsymbol{k}v_2} \tag{3.20}$$

$$\text{and,}\qquad \varrho_{\substack{\boldsymbol{k}'v_4\\ \{\boldsymbol{k}'+\boldsymbol{Q}\}c_3}}(-(\boldsymbol{Q}+\boldsymbol{G}))=\sum_{\varsigma}e^{i(\{\boldsymbol{k}'+\boldsymbol{Q}\}-\boldsymbol{k}'-(\boldsymbol{Q}+\boldsymbol{G}))\cdot\boldsymbol{s}_{\varsigma}}\left(\phi^{\varsigma}_{\boldsymbol{k}'v_4}\right)^{*}\phi^{\varsigma}_{\{\boldsymbol{k}'+\boldsymbol{Q}\}c_3}, \tag{3.21}$$

while the resonant Fock term yields

$$W^{\{\boldsymbol{k}+\boldsymbol{Q}\}c_1,\boldsymbol{k}'v_4}_{\boldsymbol{k}v_2,\{\boldsymbol{k}'+\boldsymbol{Q}\}c_3}=\frac{1}{\mathcal{V}}\sum_{\boldsymbol{G}}\mathsf{W}\left(\{\boldsymbol{k}-\boldsymbol{k}'\}+\boldsymbol{G}\right)\left[\varrho_{\substack{\{\boldsymbol{k}+\boldsymbol{Q}\}c_1\\ \{\boldsymbol{k}'+\boldsymbol{Q}\}c_3}}\left(\{\boldsymbol{k}-\boldsymbol{k}'\}+\boldsymbol{G}\right)\right]\left[\varrho_{\substack{\boldsymbol{k}'v_4\\ \boldsymbol{k}v_2}}\left(-(\{\boldsymbol{k}-\boldsymbol{k}'\}+\boldsymbol{G})\right)\right] \tag{3.22}$$

$$\text{with,}\qquad \varrho_{\substack{\{\boldsymbol{k}+\boldsymbol{Q}\}c_1\\ \{\boldsymbol{k}'+\boldsymbol{Q}\}c_3}}\left(\{\boldsymbol{k}-\boldsymbol{k}'\}+\boldsymbol{G}\right)=\sum_{\varsigma}e^{i(\{\boldsymbol{k}'+\boldsymbol{Q}\}-\{\boldsymbol{k}+\boldsymbol{Q}\}+(\{\boldsymbol{k}-\boldsymbol{k}'\}+\boldsymbol{G}))\cdot\boldsymbol{s}_{\varsigma}}\left(\phi^{\varsigma}_{\{\boldsymbol{k}+\boldsymbol{Q}\}c_1}\right)^{*}\phi^{\varsigma}_{\{\boldsymbol{k}'+\boldsymbol{Q}\}c_3} \tag{3.23}$$

$$\text{and,}\qquad \varrho_{\substack{\boldsymbol{k}'v_4\\ \boldsymbol{k}v_2}}\left(-(\{\boldsymbol{k}-\boldsymbol{k}'\}+\boldsymbol{G})\right)=\sum_{\varsigma}e^{i(\boldsymbol{k}-\boldsymbol{k}'-(\{\boldsymbol{k}-\boldsymbol{k}'\}+\boldsymbol{G}))\cdot\boldsymbol{s}_{\varsigma}}\left(\phi^{\varsigma}_{\boldsymbol{k}'v_4}\right)^{*}\phi^{\varsigma}_{\boldsymbol{k}v_2}. \tag{3.24}$$

Comparing the resonant and coupling indices in Eqs.(3.17) and (3.18) respectively, we see that the momentum indices stay exactly the same while the band indices swap as $v_4 \to c_4$ and $c_3 \to v_3$. Therefore, the expressions for the coupling block are the same as for the resonant block in Eqs.(3.19) through (3.24) but instead with the band indices altered as $v_4 \to c_4$ and $c_3 \to v_3$.

3.3 Structure of eigen-problem in the spin degree of freedom

Until now we have omitted the spin degrees of freedom, effective dealing with spineless fermions. We will now study the effect of spin in the structure of the effective two-particle Hamiltonian. We consider, however, the spin-orbit interaction to be negligible such that the single-particle states can be simply classified as either spin-up $|\uparrow\rangle$ or spin-down $|\downarrow\rangle$ states, this way, we just have to introduce the spin degree of freedom $\sigma = \uparrow, \downarrow$ and sum over all the possible spin combinations of σ_3 and σ_4 in Eq.(3.16). The Hilbert space of the electron-hole pairs consists now of eight subspaces: $|c_3\uparrow_3, v_4\uparrow_4\rangle$, $|c_3\uparrow_3, v_4\downarrow_4\rangle$, $|c_3\downarrow_3, v_4\uparrow_4\rangle$, $|c_3\downarrow_3 v_4\downarrow_4\rangle$ and the other four instead with $c_3 \to v_3$ and $v_4 \to c_4$. Therefore, the linear response equation (shown within the TDA for the sake of space) yields

$$\left(\hbar\omega\mathbb{1} - \begin{bmatrix} R^{\uparrow_3\uparrow_4}_{\uparrow_1\uparrow_2} & R^{\uparrow_3\downarrow_4}_{\uparrow_1\uparrow_2} & R^{\downarrow_3\uparrow_4}_{\uparrow_1\uparrow_2} & R^{\downarrow_3\downarrow_4}_{\uparrow_1\uparrow_2} \\ R^{\uparrow_3\uparrow_4}_{\uparrow_1\downarrow_2} & R^{\uparrow_3\downarrow_4}_{\uparrow_1\downarrow_2} & R^{\downarrow_3\uparrow_4}_{\uparrow_1\downarrow_2} & R^{\downarrow_3\downarrow_4}_{\uparrow_1\downarrow_2} \\ R^{\uparrow_3\uparrow_4}_{\downarrow_1\uparrow_2} & R^{\uparrow_3\downarrow_4}_{\downarrow_1\uparrow_2} & R^{\downarrow_3\uparrow_4}_{\downarrow_1\uparrow_2} & R^{\downarrow_3\downarrow_4}_{\downarrow_1\uparrow_2} \\ R^{\uparrow_3\uparrow_4}_{\downarrow_1\downarrow_2} & R^{\uparrow_3\downarrow_4}_{\downarrow_1\downarrow_2} & R^{\downarrow_3\uparrow_4}_{\downarrow_1\downarrow_2} & R^{\downarrow_3\downarrow_4}_{\downarrow_1\downarrow_2} \end{bmatrix}\right) \begin{bmatrix} \rho^{(1)}_{c_3\uparrow_3, v_4\uparrow_4} \\ \rho^{(1)}_{c_3\uparrow_3, v_4\downarrow_4} \\ \rho^{(1)}_{c_3\downarrow_3, v_4\uparrow_4} \\ \rho^{(1)}_{c_3\downarrow_3, v_4\downarrow_4} \end{bmatrix} = \begin{bmatrix} \mathcal{J}_{c_1\uparrow_1, v_2\uparrow_2} \\ \mathcal{J}_{c_1\uparrow_1, v_2\downarrow_2} \\ \mathcal{J}_{c_1\downarrow_1, v_2\uparrow_2} \\ \mathcal{J}_{c_1\downarrow_1, v_2\downarrow_2} \end{bmatrix}. \tag{3.25}$$

Notice that most of the matrix elements are actually zero due to spin conservation, since the virtual transferred particle does not carry spin i.e the interaction does not induce spin-flips. To see why, we turn once more to a diagrammatic approach and study the diagrams in Fig.(4). For example, in the free-particles term and in the Fock term represented in Fig.(4)(a) and (b) respectively, we must force the spin σ_3 to be the same as σ_1 and the spin σ_2 to be the same as σ_4. One the other hand, in the Hartree term in Fig.(4)(c), we must force the spin σ_1 to be the same as σ_2 and the spin σ_4 to be the same as σ_3. Therefore, we are left with

$$\boldsymbol{R} = \begin{bmatrix} \epsilon + V - W & 0 & 0 & V \\ 0 & \epsilon - W & 0 & 0 \\ 0 & 0 & \epsilon - W & 0 \\ V & 0 & 0 & \epsilon + V - W \end{bmatrix} \begin{matrix} \uparrow\uparrow \\ \uparrow\downarrow \\ \downarrow\uparrow \\ \downarrow\downarrow \end{matrix}, \tag{3.26}$$

where, for compactness, we wrote $\epsilon := \left(\epsilon_{\{\boldsymbol{k}+\boldsymbol{Q}\}c_1} - \epsilon_{\boldsymbol{k}v_2}\right)$, $W := W^{\{\boldsymbol{k}+\boldsymbol{Q}\}c_1,\boldsymbol{k}'v_4}_{\boldsymbol{k}v_2,\{\boldsymbol{k}'+\boldsymbol{Q}\}c_3}$ and $V := V^{\boldsymbol{k}'v_4,\{\boldsymbol{k}+\boldsymbol{Q}\}c_1}_{\boldsymbol{k}v_2,\{\boldsymbol{k}'+\boldsymbol{Q}\}c_3}$. If we now change the basis to

$$U = \begin{bmatrix} \frac{1}{\sqrt{2}} & \frac{1}{\sqrt{2}} & 0 & 0 \\ 0 & 0 & 1 & 0 \\ 0 & 0 & 0 & 1 \\ \frac{1}{\sqrt{2}} & -\frac{1}{\sqrt{2}} & 0 & 0 \end{bmatrix}, \tag{3.27}$$

we effectively decouple the problem into a spin-singlet class of solutions with symmetric subspace $(1/\sqrt{2})\left(|c\uparrow, v\uparrow\rangle + |c\downarrow, v\downarrow\rangle\right)$ for which the Hamiltonian becomes

$$R_{\mathrm{s}} = \epsilon - W + 2V, \tag{3.28}$$

and a spin-triplet class of solutions, consisting of the subspaces $|c\uparrow, v\downarrow\rangle$ and $|c\downarrow, v\uparrow\rangle$, and the anti-symmetric $(1/\sqrt{2})\left(|c\uparrow, v\uparrow\rangle - |c\downarrow, v\downarrow\rangle\right)$, for which the Hamiltonian becomes

$$R_{\mathrm{t}} = \epsilon - W. \tag{3.29}$$

The linear response can thus be solved for singlet and triplet configuration separately, we no further regards to the spin degrees of freedom. This still holds true outside the TDA, considering the coupling block $\boldsymbol{C}$. Notice that, if the spin-orbit interaction was not negligible, the singlet and triplet configurations would have mixed and the two-particle Hamiltonian must be discussed including its full spin structure. This increases the number of basis states by a factor of 4 and the evaluation of the linear response becomes more difficult. For a discussion on the effect of spin-orbit interaction on the optical spectra (not particularly in hBN but inMoS_2) see [(27)].

See that, in full analogy to the electric charge case, an electron of spin σ removed from a fully occupied valence band can be interpreted as the valence band having an overall deficiency of spin σ which can then be regarded as a hole with spin $-\sigma$. In this sense the singlet state can be understood as a zero spin electron-hole bound state.

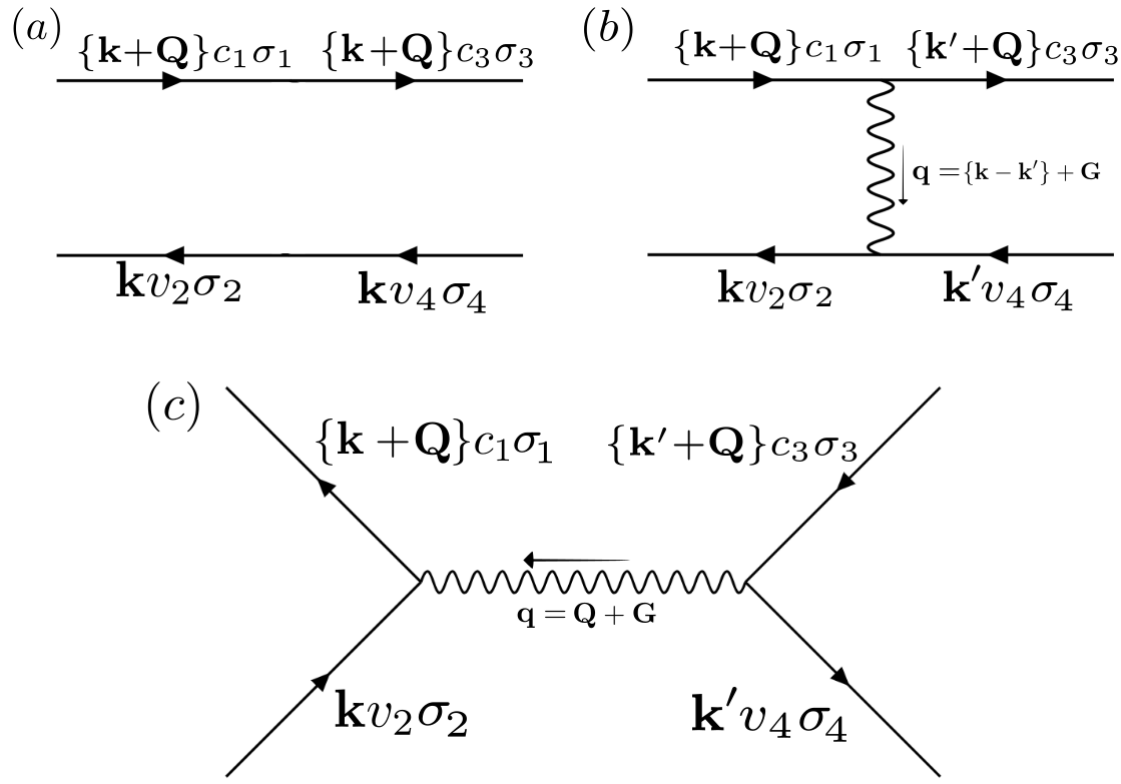

Figure 4: Feynman diagram of the electron-electron interaction including spins for the **(a)** free-particles/non-interacting term [corresponding to the first term in Eq.(3.17)], **(b)** for the resonant Fock interaction [in Eq.(3.19)] and **(c)** for the resonant Hartree interaction [in Eq.(3.22)].

3.4 Screening in the Hartree and Fock terms

While we prematurely introduced the screened potential W into the Fock self-energy term in Eq.(2.32), we still haven't discuss the reason why the Fock term is screened while the Hartree term is not. Since we already discussed the many-body perturbation problem and obtained a description for the effective two-particle collective excitations, we are now more then capable to clearly see why this is the case. Foremost to this discussion, we note that the Hartree term is also commonly referred as being the *exchange* term and the Fock term as the *direct* term although, when talking about two electrons interaction outside the context of a excitonic problem, the Fock term is actually the one being called the exchange term and the Hartree as the direct (this is just an unfortunate mismatch).

For this discussion, it is useful to take a diagrammatic approach and write the Bethe-Salpeter equation (BSE) as its analogous Dyson equation $\mathcal{G} = G_0 + G_0\Sigma\mathcal{G}$ where $\mathcal{G}$ is the two-particle propagator, G_0 is the non-interacting single-particle propagator and Σ is the *proper/irreducible* self-energy of the interaction, i.e that no component of Σ can be written in terms of two self-energy connected by G_0. As usual, an

iterative solution can be constructed by making the initial ansatz $\mathcal{G} = G_0$, obtaining $\mathcal{G} = G_0 + G_0\Sigma G_0$ and then repeatedly substituting the new equality back into $\mathcal{G}$ until we arrive at $\mathcal{G} = G_0 + G_0\Sigma G_0 + G_0\Sigma G_0\Sigma G_0 + \ldots$. Diagrammatically, this expansion amounts to an infinite series of diagrams containing all possible combinations of the interaction vertex.

Consider, initially, the interaction to be the bare Coulomb V. Setting $\Sigma = \Sigma^H$, the Dyson equation for the Hartree interaction is as shown in Fig.(5)(a). Notice that all diagrams from 2rd order onward contain a series of "bubbles" diagrams formed from the combinations VG_0V. Analogously, setting $\Sigma = \Sigma^F$ for the Fock interaction, we obtain a corresponding series of "ladders" as shown in Fig.(5)(b).

Consider now that we substitute our bare Coulomb potential for the *random phase approximation* (RPA) screened potential W_{RPA}. In the RPA, electrons are assumed to respond to an effective potential W_{RPA} which already accounts for an averaging of screening effects. We can write the renormalized interaction as $W_{RPA} = V + V\mathcal{L}V + V\mathcal{L}V\mathcal{L}V + \ldots$ where $\mathcal{L}$ is the so called Lindhard function corresponding to the proper bubble diagram as shown in Fig.(5)(c). Now see what happens if we substitute the potential W_{RPA} in the place of V in both the Hartree and Fock terms. For the Fock terms it's easy to see that each "rung" term has now infinite terms, corresponding to each of the bubbles of the interaction line. However, if we try to do the same for the Hartree term, we just obtain diagrams that are already accounted elsewhere in the original expansion. This multiple counting of equivalent terms is strictly forbidden since the interaction potential must be proper, so it is concluded that the interaction V in the Hartree term must not be screened, at least in the RPA sense. Said in other words, the bubble series in Fig.(5)(b) already "naturally" screens itself.

We note that some studies argue that, when solving the BSE in a restricted subspace of the full Hilbert space (for example, the subspace associated with low-energy bands close to the Fermi energy), the Hartree interaction should be appropriately screened by states outside of said subspace (for example, higher energy bands and/or other physical subsystems such as substrates). This is the so called *S-approximation* [(28)]. As we will explain further ahead, for the case of isolated hBN, due to the simplicity of its band structure, we actually do not need to account for the screening of higher order bands. However, when dealing with the hBN-metal hetero-structure, we do screen both the Hartree and Fock term due to the proximity of the metal. For a more in dept discussion on the screening in the exchange term and the S-approximation see the article [(28), (29)]. As a compendium see also the many-body theory books [(30), (31)].

We take this discussion as an opportunity to point out that we are working within the static limit, $W(\omega = 0)$, meaning that we do not account for the dynamics (i.e the frequency dependency) of the screened potential $W(\omega)$. As a side note, in a non-equilibrium Dyson equation sense, this would be

equivalent to close the system of equations for the lesser- and greater-GF, also know as Kadanoff-Baym equation, by setting the collision integrals to zero [(32)]. As discussed in the article [(33)], taking into account the dynamical effects is possible however, instead of obtaining a simple eigenvalue problem, one obtains a non-linear one, this is, we would need to solve the BSE self-consistently because the Fock self-energy itself would depend on the resulting excitonic energy. Fortunately, as also pointed out in their work, taking the static limit is a reasonable approximation for most semiconductor crystals since the plasmon energies that control the dynamic of the screening are much bigger than the excitonic binding energies, effectively closing the iterative process.

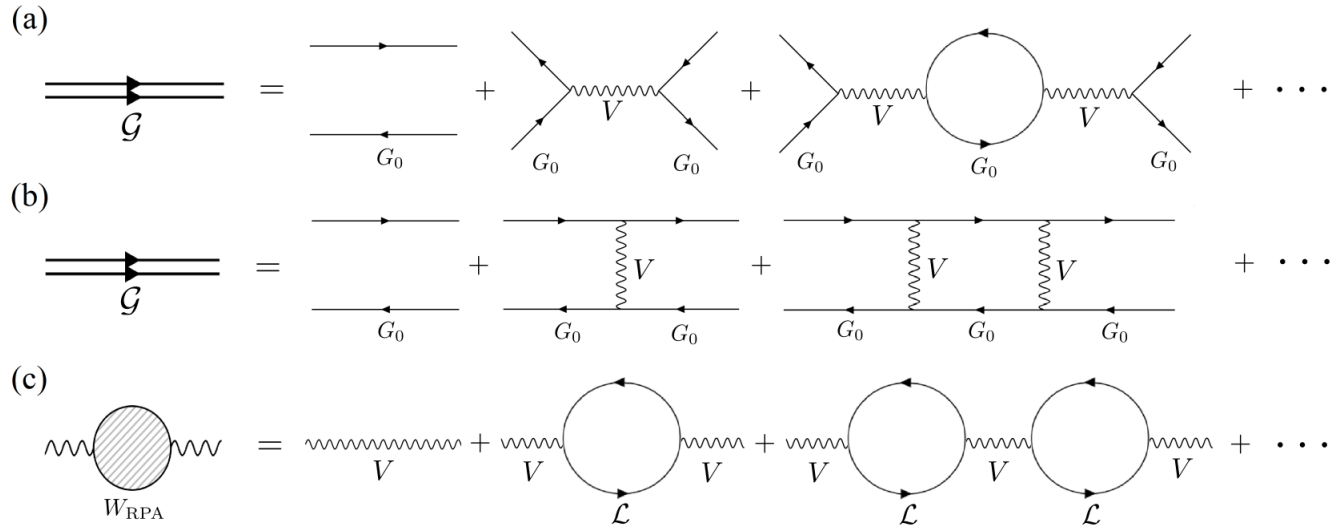

Figure 5: Diagrammatic approach to the iterative Dyson equation by expansion of the electron-hole propagator $\mathcal{G}$ in powers of the **(a)** Hartree self-energy **(b)** Fock self-energy. **(c)** RPA expansion of the effective potential W_{RPA}.

On the topic of screening, we take this opportunity to lay out the explicit form of the static potentials describing the e-e interaction. We comment on the results in three dimensions but also in two dimensions as a precursor to the study of hBN. Firstly, the bare interaction of the Hartree/exchange term corresponds to the Coulomb potential,

$$V(\boldsymbol{r}) = \frac{e^2}{4\pi\varepsilon_0}\frac{1}{|\boldsymbol{r}|}, \tag{3.30}$$

expressed in reciprocal space. Performing the 3D and 2D Fourier transforms, one obtains, respectively,

$$V_{3D}(\boldsymbol{k}) = \frac{e^2}{\varepsilon_0}\frac{1}{|\boldsymbol{k}|^2} \quad \text{and} \quad V_{2D}(\boldsymbol{k}) = \frac{e^2}{2\varepsilon_0}\frac{1}{|\boldsymbol{k}|}. \tag{3.31}$$

While for the case of a 3D dielectric the screened interaction of the Fock/direct can be obtained just by directly making the alteration $\varepsilon_0 \to \varepsilon$ in the 3D bare potentials, the same is not true for the 2D case. As

derived in Appendix B.1, the suitable choice of potential to account for the repulsive screened interaction between electrons in a polarizable 2D semiconductor is the Rytova-Keldysh potential,

$$\mathrm{W}(\boldsymbol{k}) = \frac{e^2}{2\varepsilon_0}\frac{1}{|\boldsymbol{k}|}\frac{1}{1+r_0|\boldsymbol{k}|}, \tag{3.32}$$

where $r_0 = \chi_{2D}/2$ is the so called *effective screening radius* which is material dependent. The term $1/(1+r_0k)$ account for the RPA dielectric screening as discussed above.

Chapter 4

Numerical Implementation

In this section we discuss on the numerical implementation details of the generalized eigen-problem in Eq.(2.64). For this discussion, we refer to bright excitons in hBN as a concrete example and visual aid, however, we will refrain ourselves to comment beyond numerical details since this section is prior to that of excitons hBN. In due time such comments will be made and refer to this section so one gets a complete grasp of some details. We start by showing how the discretization of the eigenvalue problem is made with a $\boldsymbol{k}$-point sampling of the electronic first Brillouin zone, tackling the complications that emerge such as the small apparent momenta divergence of the interaction and the need to implement a cutoff for large momentum. Next, in order to obtain the excitonic energies and wave-functions, we review possible numerical eigen-solvers outside and within the Tamm-Dancoff approximation. Finally, we test the convergence of the excitonic energies with the number of $\boldsymbol{k}$-point samplings and norm of cutoff as a compromise between numerical precision and computational cost (on a 8core machine).

4.1 Discretization of the eigenvalue problem

4.1.1 k-point sampling

Looking back at Eq.(3.16), although in the thermodynamic limit the sum over the electron's momentum $\boldsymbol{k}'$ should be actually an integral, in order for us to be able to withdraw any information about the excitonic band structure and wave-function, we need to retain $\boldsymbol{k}'$ as a sum over a discretized grid of $N_{\boldsymbol{k}}$ equidistant points within the 1BZ separated by some interval $\Delta_{\boldsymbol{k}}$,

$$\int_{1\text{BZ}} \frac{d\boldsymbol{k}}{(2\pi)^2} \to \Delta_{\boldsymbol{k}} \sum_{\boldsymbol{k}\in 1\text{BZ}} . \tag{4.1}$$

This can be done in a mid-point rule as

$$\boldsymbol{k}_{n_1,n_2}(\boldsymbol{b}_1,\boldsymbol{b}_2) = \frac{2n_1-\sqrt{N_{\boldsymbol{k}}}-1}{2\sqrt{N_{\boldsymbol{k}}}}\times\boldsymbol{b}_1 + \frac{2n_2-\sqrt{N_{\boldsymbol{k}}}-1}{2\sqrt{N_{\boldsymbol{k}}}}\times\boldsymbol{b}_2 \quad \text{, with } n_1,\, n_2 \in 1,2,...,\sqrt{N_{\boldsymbol{k}}}, \tag{4.2}$$

where $\boldsymbol{b}_1$ and $\boldsymbol{b}_2$ are reciprocal space vectors and the interval length reads $\Delta_{\boldsymbol{k}} = |\boldsymbol{b}_1|/\sqrt{N_{\boldsymbol{k}}}$ along both the $\hat{\boldsymbol{b}}_1$ and $\hat{\boldsymbol{b}}_2$ direction. In Fig.(6) we shown a concrete example of a discretized 1BZ grid for the case of hBN. For example, substituting $n_1 = \sqrt{N_{\boldsymbol{k}}}$ and $n_2 = 1/2\left(\sqrt{N_{\boldsymbol{k}}}+1\right)$ into Eq.(4.2), we obtain the point near the edge of the 1BZ along the $\hat{\boldsymbol{b}}_1$ direction just shy of the symmetry point M (which is exactly on the edge of the 1BZ) by half a division length. Notice that, to guarantee that n_2 is a whole number we must set $N_{\boldsymbol{k}}$ as an odd perfect square. Also, with $N_{\boldsymbol{k}}$ being odd, it is guaranteed that the Γ symmetry point is exactly hit. In addition, particularly for the hBN case, to ensure that the immensely relevant valley symmetry points $\pm\boldsymbol{K}$ are exactly part of the grid, i.e $\pm\boldsymbol{K} \overset{!}{=} \boldsymbol{k}_{n_1,n_2}(\boldsymbol{b}_1^{\text{hBN}},\boldsymbol{b}_2^{\text{hBN}})$, one needs to specifically use $N_{\boldsymbol{K}} \in \{3+6\mathbb{N}\}^2$ where $\mathbb{N}$ are natural numbers.

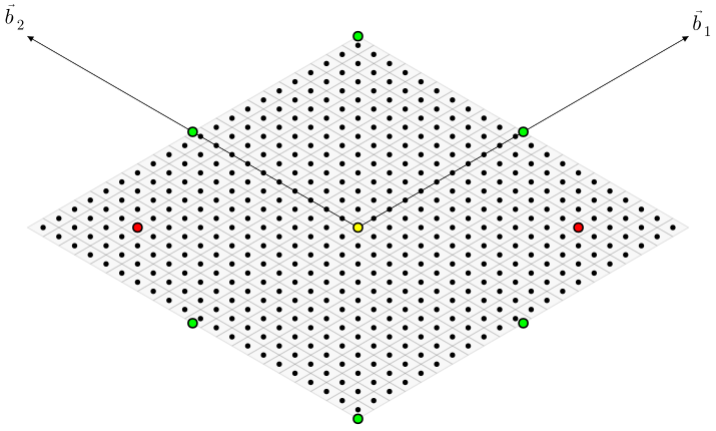

Figure 6: Discrete hBN first Brillouin zone grid with $N_{\boldsymbol{k}} = 441$ points (corresponding to $\sqrt{N_{\boldsymbol{k}}} = 21$ points along each $\boldsymbol{b}_1/\boldsymbol{b}_2$ direction) defined in a mid-point rule in the electronic $\boldsymbol{k}$-space.

After performing this $\boldsymbol{k}$-point sampling, the linear response equation in Eq.(3.16) (shown only within the TDA for the sake of space) reads

$$\left(\hbar\omega\mathbb{1}_{N_{\boldsymbol{k}}\times N_{\boldsymbol{k}}} - \begin{bmatrix} R^{\{\boldsymbol{k}_1'+\boldsymbol{Q}\}c_3,\boldsymbol{k}_1'v_4}_{\{\boldsymbol{k}_1+\boldsymbol{Q}\}c_1,\boldsymbol{k}_1v_2} & R^{\{\boldsymbol{k}_2'+\boldsymbol{Q}\}c_3,\boldsymbol{k}_2'v_4}_{\{\boldsymbol{k}_1+\boldsymbol{Q}\}c_1,\boldsymbol{k}_1v_2} & \xrightarrow{\boldsymbol{k}'} \\ R^{\{\boldsymbol{k}_1'+\boldsymbol{Q}\}c_3,\boldsymbol{k}_1'v_4}_{\{\boldsymbol{k}_2+\boldsymbol{Q}\}c_1,\boldsymbol{k}_2v_2} & R^{\{\boldsymbol{k}_2'+\boldsymbol{Q}\}c_3,\boldsymbol{k}_2'v_4}_{\{\boldsymbol{k}_2+\boldsymbol{Q}\}c_1,\boldsymbol{k}_2v_2} & \xrightarrow{\boldsymbol{k}'} \\ \downarrow\boldsymbol{k} & \downarrow\boldsymbol{k} & \ddots \end{bmatrix}\right) \begin{bmatrix} \boldsymbol{\rho}^{(1)}_{\{\boldsymbol{k}_1'+\boldsymbol{Q}\}c_3\boldsymbol{k}_1'v_4} \\ \boldsymbol{\rho}^{(1)}_{\{\boldsymbol{k}_2'+\boldsymbol{Q}\}c_3\boldsymbol{k}_2'v_4} \\ \downarrow\boldsymbol{k}' \end{bmatrix} = \begin{bmatrix} \mathcal{J}_{\{\boldsymbol{k}_1+\boldsymbol{Q}\}c_1,\boldsymbol{k}_1v_2} \\ \mathcal{J}_{\{\boldsymbol{k}_2+\boldsymbol{Q}\}c_1,\boldsymbol{k}_2v_2} \\ \downarrow\boldsymbol{k} \end{bmatrix}, \tag{4.3}$$

where $\boldsymbol{k}$ and $\boldsymbol{k}'$ run on all the points of the discretized 1BZ. From here we can construct our two-particle Hamiltonian matrix with each entry of the resonant block $\boldsymbol{R}$ and coupling block $\boldsymbol{C}$ calculated using the expressions in Eqs.(3.19) through (3.24) for a fixed exciton center of mass momentum $\boldsymbol{Q}$. The electronic

Bloch states $\phi^{\varsigma}_{\boldsymbol{k}\lambda}$ are also obtained numerical, usually through some type of DFT calculations. As we will see further in the text, in this work the electronic Bloch states $\phi^{\varsigma}_{\boldsymbol{k}\lambda}$ were calculated within a tight-binding model, corresponding to the eigenvectors of the tight-binding Hamiltonian.

4.1.2 Regularization of interaction for small momentum

Bare Coulomb potential

Consider the case of a zero momentum exciton $\boldsymbol{Q} = \boldsymbol{0}$ and the first term of the sum over the reciprocal vectors $\boldsymbol{G} = \boldsymbol{0}$. In this case, directly from Eq.(3.19), the resonant Hartree term reads

$$V^{\boldsymbol{k}'v_4,\boldsymbol{k}c_1}_{\boldsymbol{k}v_2,\boldsymbol{k}'c_3}(\boldsymbol{G}=\boldsymbol{0}) = \frac{1}{\mathcal{V}}\mathrm{V}(\boldsymbol{0})\left[\varrho^{\boldsymbol{k}c_1}_{\boldsymbol{k}v_2}(\boldsymbol{0})\right]\left[\varrho^{\boldsymbol{k}'v_4}_{\boldsymbol{k}'c_3}(\boldsymbol{0})\right] \tag{4.4}$$

$$\text{with} \qquad \varrho^{\boldsymbol{k}c_1}_{\boldsymbol{k}v_2}(\boldsymbol{0}) = \sum_{\varsigma}\left(\phi^{\varsigma}_{\boldsymbol{k}c_1}\right)^{*}\phi^{\varsigma}_{\boldsymbol{k}v_2} \tag{4.5}$$

$$\text{and} \qquad \varrho^{\boldsymbol{k}'v_4}_{\boldsymbol{k}'c_3}(\boldsymbol{0}) = \sum_{\varsigma}\left(\phi^{\varsigma}_{\boldsymbol{k}'v_4}\right)^{*}\phi^{\varsigma}_{\boldsymbol{k}'c_3}. \tag{4.6}$$

Although the bare Coulomb potential in Eq.(3.31) has an apparent divergence at $\boldsymbol{k} = \boldsymbol{0}$ that should be dealt with, since the tight-binding Block states $\phi^{\varsigma}_{\boldsymbol{k}c}$ and $\phi^{\varsigma}_{\boldsymbol{k}v}$ are orthogonal to each other (since they correspond to the eigenvectors of the TB Hamiltonian for a fixed $\boldsymbol{k}$), both form factors are actually zero and subsequently the Hartree term as a whole is also zero. This holds true also for the coupling block and for any choice of potential V.

Rytova-Keldysh potential

As derived in Appendix B.1, the Rytova-Keldysh potential, which describes the repulsive screened interaction between electrons in a polarizable 2D semiconductor, reads

$$\mathrm{W}(\boldsymbol{k}) = \frac{e^2}{2\epsilon_0}\frac{1}{|\boldsymbol{k}|}\frac{1}{1+r_0|\boldsymbol{k}|}, \tag{4.7}$$

with r_0, the effective screening radius, a constant that is material dependent. See that, for the particular case of $\boldsymbol{k} = \boldsymbol{0}$, we get a divergence of this potential. This is problematic since, due to the $\boldsymbol{k}$-point sampling, we have this divergence appearing as a Fock interaction term with $\boldsymbol{k} = \boldsymbol{k}'$ and $\boldsymbol{G} = \boldsymbol{0}$ in our

effective two-particle Hamiltonian,

$$W^{\{\boldsymbol{k}'+\boldsymbol{Q}\}c_1,\boldsymbol{k}'v_4}_{\boldsymbol{k}v_2,\{\boldsymbol{k}'+\boldsymbol{Q}\}c_3}(\boldsymbol{G}=\boldsymbol{0}) = \frac{1}{\mathcal{V}}\mathsf{W}(\boldsymbol{0})\left[\varrho^{\{\boldsymbol{k}'+\boldsymbol{Q}\}c_1}_{\{\boldsymbol{k}'+\boldsymbol{Q}\}c_3}(\boldsymbol{0})\right]\left[\varrho^{\boldsymbol{k}'v_4}_{\boldsymbol{k}'v_2}(\boldsymbol{0})\right] \tag{4.8}$$

$$\text{with} \qquad \varrho^{\{\boldsymbol{k}'+\boldsymbol{Q}\}c_1}_{\{\boldsymbol{k}'+\boldsymbol{Q}\}c_3}(\boldsymbol{0}) = \sum_{\varsigma}\left(\phi^{\varsigma}_{\{\boldsymbol{k}'+\boldsymbol{Q}\}c_1}\right)^{*}\phi^{\varsigma}_{\{\boldsymbol{k}'+\boldsymbol{Q}\}c_3} \tag{4.9}$$

$$\text{and} \qquad \varrho^{\boldsymbol{k}'v_4}_{\boldsymbol{k}'v_2}(\boldsymbol{0}) = \sum_{\varsigma}\left(\phi^{\varsigma}_{\boldsymbol{k}'v_4}\right)^{*}\phi^{\varsigma}_{\boldsymbol{k}'v_2}. \tag{4.10}$$

Notice that this divergence is not safeguarded by the orthonormality properties of the Block states $\phi^{\varsigma}_{\boldsymbol{k}\lambda}$ as it was the case for the Hartree term because the form factors now have the same band indices, cc or vv. Fortunately, we can bypass this apparent small momenta divergence going back to the integral representation of the thermodynamic limit. Therefore, we will be integrating in $\boldsymbol{k}'$ the Fock interaction term with $\boldsymbol{G}=\boldsymbol{0}$ in a tiny patch of the 1BZ centered around zero, which we will be denoting by 1bz_0. We assume that the Block states $\phi^{\varsigma}_{\boldsymbol{k}\lambda}$ in Eqs.(4.9) and (4.10) vary smoothly with $\boldsymbol{k}'$ such that they can be considered outside of the integral, effectively dealing with the divergence of W in isolation. Although the integral over the 1bz_0 is still ill-defined at zero, we can clear up the divergence by separating the integral into two distinct parts: a polar integral centered in zero with a radius $R_\circ$ which maximize the area of integration to the biggest possible circle enclosed within 1bz_0 and a second integral containing the remaining area $\mathcal{A}_{\text{out}}$. This regions are depicted in Fig.(7) in yellow and blue respectively (in a very low $\boldsymbol{k}$-points sampling such that 1bz_0 is big enough to see clearly). Within this course of action, the divergent term $1/k$ at $k=0$ only appears in the polar integral which ends up being canceled out with the polar Jacobian determinant k. The integral over the "weird shaped" remaining area can then be done numerically without the trouble of the divergence. We obtain

$$\int_{1\text{bz}_0}\frac{d^2\boldsymbol{k}'}{(2\pi)^2}\mathsf{W}(\boldsymbol{k}') = \frac{1}{(2\pi)^2}\frac{e^2}{2\epsilon_0}\left[2\pi\frac{\log(r_0R_\circ+1)}{r_0}+\int_{\mathcal{A}_{\text{out}}}\frac{1}{k'}\frac{1}{1+r_0k'}d^2\boldsymbol{k}'\right]. \tag{4.11}$$

We note that in a later section we will be dealing with a metal screened Rytova-Keldysh potential which effectively loses this divergence but we still had to implement this integral treatment. This is necessary because in the limiting case where the metal is very far away from the material of study, the metal screened Rytova-Keldysh potential will tend to its bare form and thus the divergence will progressively become apparent and must be dealt with. As a side note, since the metal screened Rytova-Keldysh polar integral is not so analytically trivial to solve we do it numerically (which is still fine since the divergence is not there anymore).

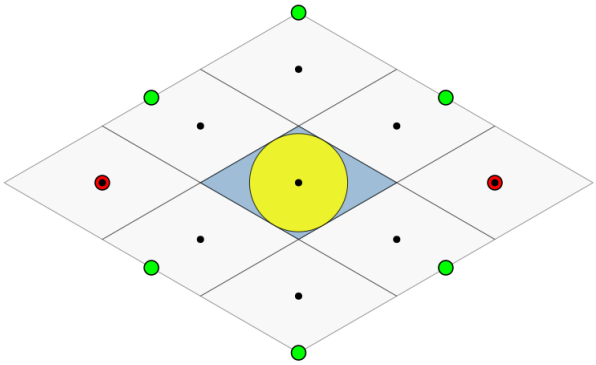

Figure 7: Discrete hBN first Brillouin zone grid with $N_{\boldsymbol{k}} = 9$ points (corresponding to $\sqrt{N_{\boldsymbol{k}}} = 3$ points along each $\boldsymbol{b}_1/\boldsymbol{b}_2$ direction) defined in a mid-point rule in the electronic $\boldsymbol{k}$-space. The yellow area correspond to the biggest possible circle enclosed within the central tiny patch of the 1BZ . The remaining area $\mathcal{A}_{\text{out}}$ is colored in blue.

4.1.3 Cutoff of the interaction for large momentum

As a mean to define a numerical precision to our calculations, we now introduce a cutoff norm $|\boldsymbol{k}_{\text{cutoff}}|$ to the interaction range of both the bare and screened potentials for large momentum such that

$$\mathrm{V}\left(\boldsymbol{k} > |\boldsymbol{k}_{\text{cutoff}}|\right) = \mathrm{W}\left(\boldsymbol{k} > |\boldsymbol{k}_{\text{cutoff}}|\right) = 0. \tag{4.12}$$

This cutoff is proactively justified by the absence of the term $\underset{ss'}{\varrho_{\mathbf{00}}}(\boldsymbol{k})$ introduced in Sec.III.A, which is known to decay fairly quickly. Since we have set this term to unity in our ultra-localized orbitals we are effectively missing out on this rapid decay and most introduce it manually. Therefore, with this cutoff most of the effective two-particle Hamiltonian terms [described in Eqs.(3.19) through (3.24)] will be exactly zero and not just very small valued. The Hamiltonian $H_{\text{e-h}}$ will have a dominant diagonal due to the free-particles non-interacting term while the off-diagonal terms fade in magnitude. This fact is a huge numerical advantage since we should be able to use *sparse matrices*. Sparse matrices provide a more efficient storage of data that has a large percentage of zeros, typically $> 70\%$. While full (or dense) matrices store every single element in memory regardless of value, sparse matrices store only the nonzero elements and their position within the matrix. However, as it turned out, the use of sparse matrix was not fully justified since the percentage of zeros in the matrix was not big enough for numerical improvement and we defaulted to using dense matrices (we could, of course, diminish the cutoff norm even more such that the matrix had a usable percentage of zeros, however we would be cutting off relevant contributions).

Moreover, due to this cutoff range, we can upper-bound the infinite sum over all possible the reciprocal lattice vectors $\boldsymbol{G}$ in Eqs.(3.19) through (3.24) accounting only for the neighboring Brillouin zones that are

actually within the cutoff range of all points within the 1BZ. In Fig.(8) we show how this upper-bounding responds for a given cutoff.

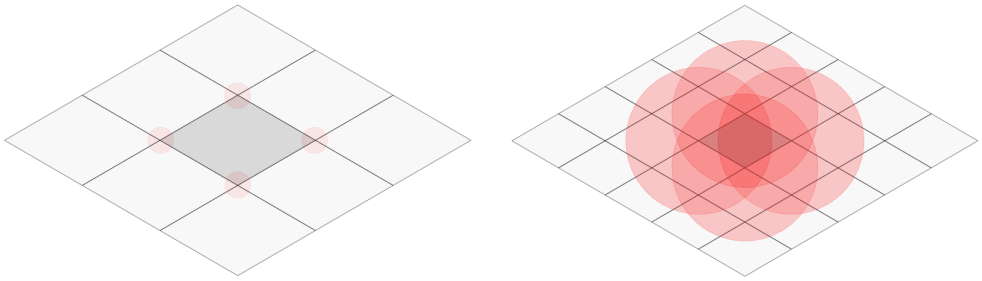

Figure 8: Upper-bounding of the summation $\sum_{\boldsymbol{G}}$ due to the cutoff norm for values **(a)** $|\boldsymbol{k}_{\text{cutoff}}| = |\boldsymbol{M} - \boldsymbol{K}|/2 \approx 0.43\text{Å}^{-1}$ and **(b)** $|\boldsymbol{k}_{\text{cutoff}}| = 4\text{Å}^{-1}$, represented in the electronic $\boldsymbol{k}$-space. The red circles, centered at the 1BZ (in dark gray) vertices, represents the allowed area within which a grid point has $|\boldsymbol{k}| < |\boldsymbol{k}_{\text{cutoff}}|$. In light gray are all the neighboring BZs, defined by a $\boldsymbol{G}(n_1, n_2)$ shift from the 1BZ, that intersect with said red circles. The $|\boldsymbol{M} - \boldsymbol{K}|/2$ distance, corresponding to the radius of a 1BZ circumscribed circle centered in $\pm\boldsymbol{K}$ and characterizes the low-energy regime.

4.2 Eigen-solvers

Once the effective two-particle Hamiltonian is built, the next step is to calculate its eigenvalues. Numerically, this is a simple task and can be done in a number of different ways. In our case, this was done in *Julia* in two different manners. Initially, we focused on the Tamm-Dancoff approximation and solved the simple eigen-problem $\boldsymbol{R} \cdot \boldsymbol{\Psi}_X = E_X \boldsymbol{\Psi}_X$ resorting to the built-in eigen$(A, 1:n)$ function, which provided us with the eigenvalues up to the nth state as long as A is Hermitian (which $\boldsymbol{R}$ is). However, outside of the TDA, one has to solve a generalized eigenvalue problem, $\boldsymbol{H}_{\text{e-h}} \cdot \boldsymbol{\Psi}_X = E_X \boldsymbol{S} \cdot \boldsymbol{\Psi}_X$, and cannot straightforwardly use the eigen$(A, 1:n)$ function. For this, one needs to use some approximated eigenvalue algorithm like the *power method* [(34)]. Moreover, considering that the excitonic eigenvalues appear as $-\lambda_{N_{\boldsymbol{k}}}, -\lambda_{N_{\boldsymbol{k}}-1}, ..., -\lambda_1, +\lambda_1, ..., +\lambda_{N_{\boldsymbol{k}}-1}, +\lambda_{N_{\boldsymbol{k}}}$ (as commented previously in Sec.II.C.3), one would need to use instead a *shifted inverse* power method [(34)] since uniquely using the inverse method would only get us the largest eigenvalue but with a negative sign and uniquely using the shifted method would get us the positive-negative pars around zero. In particular, we resorted to the *Arnoldi iteration algorithm* [(35)], which is basically an improved power method, particularly useful when dealing with large sparse matrices [(36)].

4.3 Convergence with sampling and cutoff

First and foremost, before showing any relevant results, we must test the optimal number of $\boldsymbol{k}$-sampling points $N_{\boldsymbol{k}}$ and the optical cutoff $\boldsymbol{k}_{\text{cutoff}}$, chosen as a compromise between numerical precision and computational cost. We study the absolute and relative errors along the convergence of the first 8 energy levels with one of the parameters fixed in its optimal value while the other is incrementally increasing. This was, of course, an iterative process between the results of $N_{\boldsymbol{k}}$ and $\boldsymbol{k}_{\text{cutoff}}$ after some decent guess. The $\boldsymbol{k}_{\text{cutoff}}$ initial guess can be reasoned, for example, by looking at the magnitude of a given row of $R_{\boldsymbol{k},\boldsymbol{k}'\in 1\text{BZ}}$ calculated with large $N_{\boldsymbol{k}}$ and $\boldsymbol{k}_{\text{cutoff}}$ [calculated using the expression in Eq.(4.3)] as shown in Fig.(9). In this heatmap plot, we can see that the strength of interaction between $\boldsymbol{k} = \boldsymbol{K}$ and its neighboring points $\boldsymbol{k}'$ doesn't extend much further than $\approx 1\,\text{Å}^{-1}$, with the remaining values being of order $\approx 10^{-6}$eV. While the convergence tests were performed for optically active modes (singlet-state with $\boldsymbol{Q} = \boldsymbol{0}$) within the TDA, we assume that the results applies outside of the TDA as well as for all other $\boldsymbol{Q}$'s and for the triplet-states. Analyzing the convergence of the energy levels accompanied by its absolute and relative error for consecutive increments of the respective parameter compiled in Fig.(10), we consider the values $N_{\boldsymbol{k}} = (3 + 6 \times 15)^2 \approx 9000$ points and $\boldsymbol{k}_{\text{cutoff}} = 1.5\text{Å}^{-1}$ to be an optimal compromise between numerical precision and computational cost (on a 8core machine) and, as such, will be used throughout all the numerical calculations. Building the 9000×9000 two-particle matrix from Eqs.(3.19) through (3.24) and calculating its first eight energies with the built-in *Julia* eigen-solver took about $\sim$30min. From the absolute error shown in Fig.(10) we consider to have precision roughly to the second decimal place and will be showing the results accordingly.

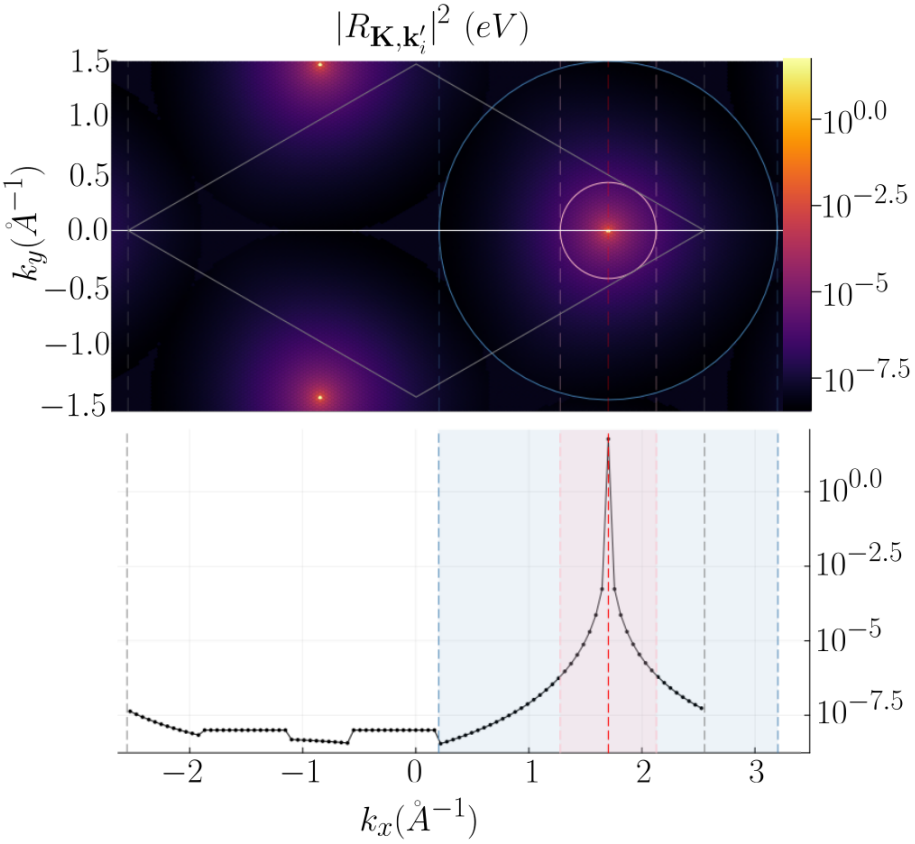

Figure 9: **(top)** Strength of interaction of $\boldsymbol{K}$ with its neighboring $\boldsymbol{k}'_i \in$ 1BZ, corresponding to the 1BZ heatmap plot of the entries of the resonant block row $R_{\boldsymbol{K},\boldsymbol{k}'_i}$. **(bottom)** Entries of the resonant block row $R_{\boldsymbol{K},\boldsymbol{k}'_i}$ for only $\boldsymbol{k}'_i \in$ 1BZ $\cap\, k_y = 0$, corresponding to the path denoted in white in the heatmap. The 1BZ is depicted in gray outlines. Points outside the 1BZ area were shifted from within the 1BZ by a given reciprocal lattice vector $\boldsymbol{G}$ for viewing purposes. The pink highlights characterizes the low-energy regime and has radius $|\boldsymbol{k}_{\text{cutoff}}| = |\boldsymbol{M} - \boldsymbol{K}|/2 \approx 0.43\mathring{\text{A}}^{-1}$. The blue highlights characterizes chosen optimal cutoff, $|\boldsymbol{k}_{\text{cutoff}}| = 1.5$.

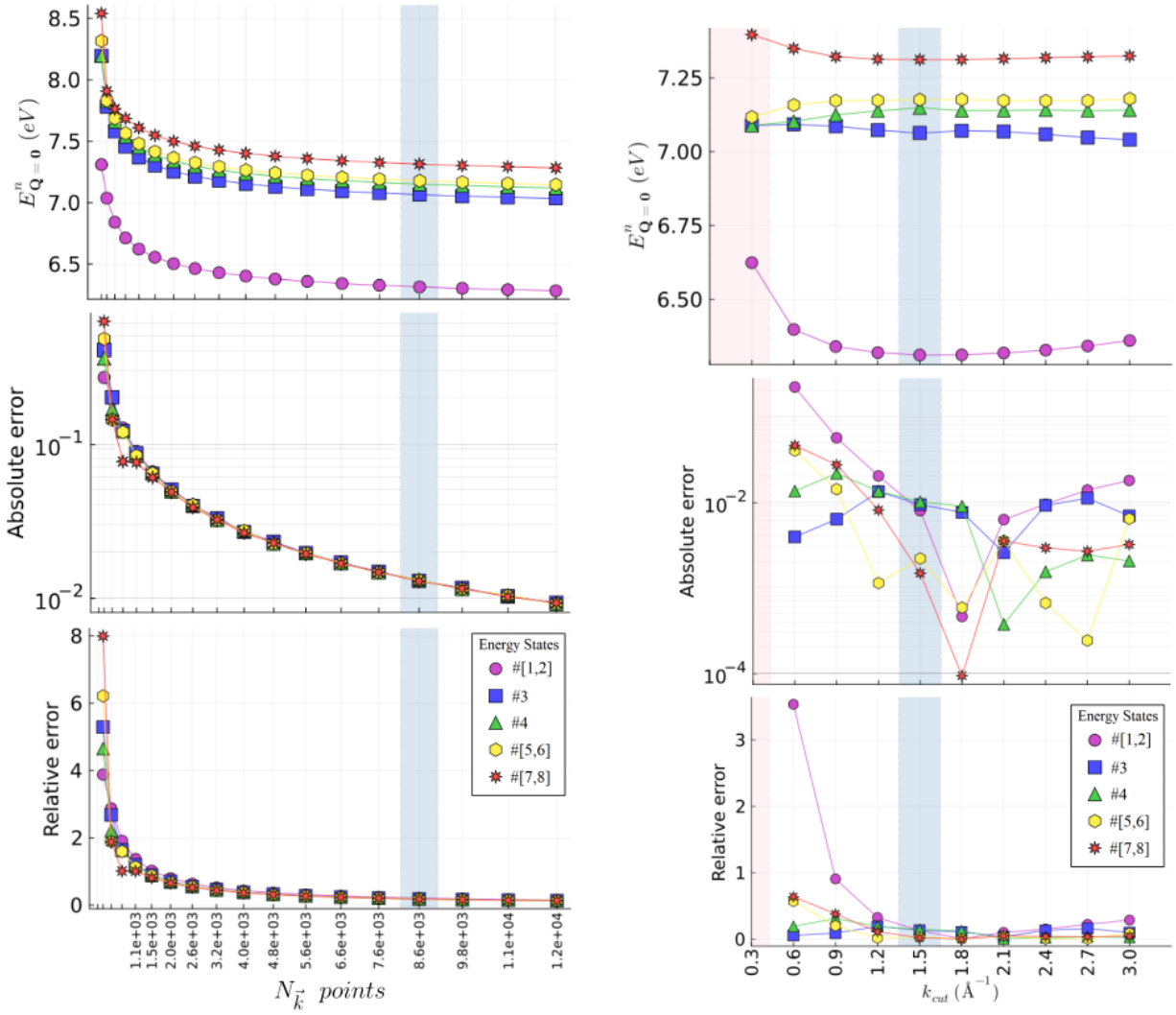

Figure 10: Convergence of the first eight energy levels for a bright exciton in hBN as a function of **(1st column)** the number of $\boldsymbol{k}$-sampling points $N_{\boldsymbol{k}}$ using $|\boldsymbol{k}_{\text{cutoff}}| = 1.5\text{Å}^{-1}$ and *(***2nd column***)* as a function of the cutoff norm $|\boldsymbol{k}_{\text{cutoff}}|$ using $N_{\boldsymbol{k}} \approx 9000$ points. Each energy convergence plot is accompanied by the absolute error in a log10 scale and the relative error between energies calculated with consecutive increments of the respective parameter. There are only 5 states visible because we treated degenerated states as being the same state (which we checked to behaved the same apart from some very minor variations.). The blue shaded area corresponds to the values taken as the optimal compromise between numerical precision and computational cost. The pink shaded area characterizes the low-energy regime and has radius $|\boldsymbol{k}_{\text{cutoff}}| = |\boldsymbol{M} - \boldsymbol{K}|/2 \approx 0.43\text{Å}^{-1}$.

Chapter 5

Excitons on hBN structures

5.1 Tight-binding model for the single-particle Bloch states

Hexagonal boron nitride (hBN) is a 2D material composed of a simple layer of alternating boron and nitrogen atoms disposed in a planar honeycomb lattice, as shown in Fig.(11)(a). hBN shares a lot of similarities with graphene, also a 2D honeycomb structured material but instead composed of only carbon atoms. The most relevant distinction is that graphene behaves as a semi-metal with a zero-gap at its Dirac points while hBN, due the different electrostatic environment in the boron and in the nitrogen atom, has an opening gap of about $\epsilon_g = 5.9$eV (there are actually a lot of different results for ϵ_g in the literature however the mentioned value is one of the more commonly reported [(37)]. Also, hBN has a slightly larger lattice constant than graphene (about 1.8%), being around $a_0 = 2.5$Å [(38)]. The planar honeycomb lattice can be described as a triangular Bravais lattice generated by the real vectors basis

$$\boldsymbol{a}_1 = \frac{a_0}{2}\left(1, \sqrt{3}\right), \tag{5.1}$$

$$\boldsymbol{a}_2 = \frac{a_0}{2}\left(-1, \sqrt{3}\right). \tag{5.2}$$

In each Wigner-Seitz cell, we have one atom of boron and one atom of nitride, which we designate as sub-lattices A and B respectively, having positions,

$$\boldsymbol{s}_A = (0, 0), \tag{5.3}$$

$$\boldsymbol{s}_B = \frac{a_0}{\sqrt{3}}(0, 1). \tag{5.4}$$

For each site A, the position of the nearest-neighbors (NN) in the sites B are given by

$$\boldsymbol{\delta}_1 = \frac{a_0}{\sqrt{3}}(0, 1), \tag{5.5}$$

$$\boldsymbol{\delta}_2 = \frac{a_0}{2\sqrt{3}}\left(-\sqrt{3}, -1\right), \tag{5.6}$$

$$\boldsymbol{\delta}_3 = \frac{a_0}{2\sqrt{3}}\left(\sqrt{3}, -1\right). \tag{5.7}$$

All these vectors are shown in Fig.(11)(a) within the real space lattice. Furthermore, from the real lattice basis vectors follow the reciprocal lattice basis vectors

$$\boldsymbol{b}_1 = \frac{2\pi}{\sqrt{3}a_0}\left(\sqrt{3}, 1\right), \tag{5.8}$$

$$\boldsymbol{b}_2 = \frac{2\pi}{\sqrt{3}a_0}\left(-\sqrt{3}, 1\right). \tag{5.9}$$

which are shown in Fig.(11)(b) together with the first zone of Brillouin, which they form.

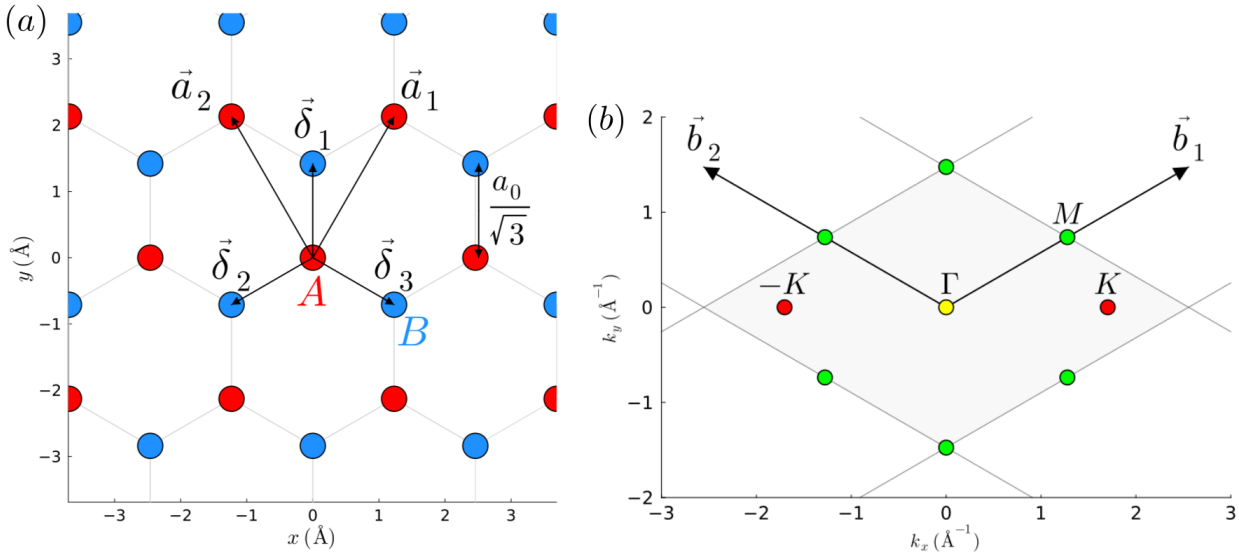

Figure 11: **(a)** hBN real space honeycomb lattice constructed from two superposed triangular sub-lattices of boron atoms (depicted in red), denoted as sub-lattice A, and of nitrogen atoms (depicted in blue), denoted as sub-lattice B. The vectors $\boldsymbol{a}_1$ and $\boldsymbol{a}_2$ are the lattice basis vectors and $\boldsymbol{\delta}_1$, $\boldsymbol{\delta}_2$ and $\boldsymbol{\delta}_3$ are the nearest-neighbor vectors. **(b)** hBN reciprocal space lattice with $\boldsymbol{b}_1$ and $\boldsymbol{b}_2$ its basis vectors. The first Brillouin zone is emphasized in light gray while the remaining are only outlined. The red dots correspond to the Dirac points $\pm K$ and the green dots correspond to the 1BZ edges M points.

In order to compute the excitonic energies using Eqs.(3.19) through (3.24), we first need to know the single-particle Bloch wave-functions $\phi^{S}_{\boldsymbol{k}\lambda}$. In this work we calculate them in a nearest-neighbors tight-binding model. For this, we write the system's single-particle NN tight-binding Hamiltonian in real space as

$$H_{\text{TB}}(\boldsymbol{R}) = \sum_i \epsilon_A a^\dagger_{\boldsymbol{R}_i} a_{\boldsymbol{R}_i} + \sum_i \epsilon_B b^\dagger_{\boldsymbol{R}_i} b_{\boldsymbol{R}_i} - t \sum_{\langle i,j \rangle} \left(a^\dagger_{\boldsymbol{R}_i} b_{\boldsymbol{R}_i + \boldsymbol{\delta}_j} + b^\dagger_{\boldsymbol{R}_j} a_{\boldsymbol{R}_i - \boldsymbol{\delta}_j} \right), \tag{5.10}$$

where the operators $a^\dagger_{\boldsymbol{R}_i}(a_{\boldsymbol{R}_i})$ create (annihilate) an electron in the sub-lattice A in a given Bravais lattice site $\boldsymbol{R}_i$ while the operators $b^\dagger_{\boldsymbol{R}_i}(b_{\boldsymbol{R}_i})$ create (annihilate) an electron instead in the sub-lattice B (in a

given Bravais lattice site $\boldsymbol{R}_i$). Therefore, the first two terms correspond to the isolated single-particles Hamiltonian of the site A and B, respectively, and the last term to the hybridization between neighboring sites i and j, describing the possible hoppings from site A to site B and vice-versa. We only assess hopping terms up to the first neighbors terms, which is denote by $\langle i,j\rangle$, and consider a static hopping term in either direction, i.e $t_{\boldsymbol{R}_i,\boldsymbol{R}_j} \to -t$. Notice that, contrarily to graphene, since the atoms on sites A and B are different the single-particle energies ϵ_A and ϵ_B are inherently different. We can represent the NN TB Hamiltonian in Eq.(5.10) in reciprocal space by expressing the creation/annihilation operators as their Fourier counterparts,

$$a_{\boldsymbol{R}_i} = \frac{1}{\sqrt{V}} \sum_{\boldsymbol{k}} e^{+i\boldsymbol{k}\cdot(\boldsymbol{R}_i+\boldsymbol{s}_A)} a_{\boldsymbol{k}}, \tag{5.11}$$

$$b_{\boldsymbol{R}_i} = \frac{1}{\sqrt{V}} \sum_{\boldsymbol{k}} e^{+i\boldsymbol{k}\cdot(\boldsymbol{R}_i+\boldsymbol{s}_B)} b_{\boldsymbol{k}}, \tag{5.12}$$

and rearranging the expression just that the identity $\delta(\boldsymbol{k}-\boldsymbol{k'}) = 1/N \sum_i e^{-i\boldsymbol{R}_i\cdot(\boldsymbol{k}-\boldsymbol{k'})}$ is apparent. We obtain

$$H_{\text{TB}}(\boldsymbol{R}) = \sum_{\boldsymbol{k}} \epsilon_A a^\dagger_{\boldsymbol{k}} a_{\boldsymbol{k}} + \sum_{\boldsymbol{k}} \epsilon_B b^\dagger_{\boldsymbol{k}} b_{\boldsymbol{k}} - t \sum_{\boldsymbol{k}} \left(\gamma_{\boldsymbol{k}} a^\dagger_{\boldsymbol{k}} b_{\boldsymbol{k}} + \gamma^\dagger_{\boldsymbol{k}} b^\dagger_{\boldsymbol{k}} a_{\boldsymbol{k}} \right), \tag{5.13}$$

with the newly-defined γ complex number,

$$\gamma_{\boldsymbol{k}} = \sum_{\langle j \rangle} e^{+i\boldsymbol{k}\cdot\boldsymbol{\delta}_j}. \tag{5.14}$$

If we now define a row vector $c^\dagger_{\boldsymbol{k}} = \begin{bmatrix} a^\dagger_{\boldsymbol{k}} & b^\dagger_{\boldsymbol{k}} \end{bmatrix}$ we can rewrite the system's Hamiltonian as $H^{\text{TB}}_{\boldsymbol{R}} = \sum_{\boldsymbol{k}} c^\dagger_{\boldsymbol{k}} H^{\text{TB}}_{\boldsymbol{k}} c_{\boldsymbol{k}}$ with the hBN NN TB Hamiltonian matrix being

$$H_{\text{TB}}(\boldsymbol{k}) = \begin{bmatrix} \epsilon_A & -t\gamma_{\boldsymbol{k}} \\ -t\gamma^\dagger_{\boldsymbol{k}} & \epsilon_B \end{bmatrix}. \tag{5.15}$$

Within this simplified tight-binding model, the expression for the electronic two-band structure can easily be obtained analytically by diagonalizing the matrix in Eq.(5.15), yielding

$$E^{\pm}_{\text{TB}}(\boldsymbol{k}) = \pm \sqrt{\epsilon^2 + t^2 \left[3 + 2\cos(a_0 k_x) + 4\cos\left(\frac{a_0\sqrt{3}}{2} k_y\right) \cos\left(\frac{a_0}{2} k_x\right) \right]}. \tag{5.16}$$

Here we defined the zero point energy at $(\epsilon_A + \epsilon_B)/2$ and defined $\epsilon \equiv (\epsilon_A - \epsilon_B)/2$ at the middle of the gap such that $\epsilon_A = \epsilon$ and $\epsilon_B = -\epsilon$. The valence band corresponds to the $E^-_{\text{TB}}(\boldsymbol{k})$ dispersion while the $E^+_{\text{TB}}(\boldsymbol{k})$ corresponds to the conduction band, as shown in Fig.(12) which is accompanied by the density of states $\text{DoS}(E) = \sum_{\boldsymbol{k}} \delta(E - E(\boldsymbol{k}))$. Notice that, if $\epsilon_A = \epsilon_B$, as is the case for

graphene, we obtain $\epsilon = 0$ and the band dispersion closes in a linear fashion at the so called Dirac points, $\boldsymbol{K}^{\pm} = (\pm 4\pi/(3a_0), 0)$. In hBN, the electronic band dispersion is also at its minimum near these points but has instead a parabolic shape. In either case, this points represent a fundamental symmetry of the system, called valley parity. To see why the dispersion is parabolic at these valley points, we Taylor series expand the exponential of $\gamma_{\boldsymbol{k}}$ in Eq.(5.14) near $\boldsymbol{k} \to \boldsymbol{K} + \boldsymbol{p}$ with $\boldsymbol{p} \to 0$. We obtain $e^{+i\boldsymbol{p}\cdot\boldsymbol{\delta}_j} \approx 1 + i\boldsymbol{p}\cdot\boldsymbol{\delta}_j$. Now, since $\sum_{\langle j \rangle} e^{+i\boldsymbol{K}\cdot\boldsymbol{\delta}_j} = 0$ we are left with

$$\gamma_{\boldsymbol{K}+\boldsymbol{p}} \simeq i\boldsymbol{p}\cdot\sum_{\langle j \rangle} e^{+i\boldsymbol{K}\cdot\boldsymbol{\delta}_j}\boldsymbol{\delta}_j = -\frac{\sqrt{3}a_0}{2}\left(p_x - ip_y\right). \tag{5.17}$$

Invoking the Pauli matrices definitions, from Eq.(5.15) we can write the TB Hamiltonian $H_{\text{TB}}^{\boldsymbol{k}}$ in this low-energy regime as

$$H_{\text{TB}}(\boldsymbol{K}+\boldsymbol{p}) = \epsilon\sigma_z + t\frac{\sqrt{3}a_0}{2}\left(\boldsymbol{p}\cdot\boldsymbol{\sigma}\right), \tag{5.18}$$

which clearly resembles the 2D Dirac Hamiltonian, $H_{\text{Dirac}} = \sigma_z mc^2 + c\left(\boldsymbol{p}\cdot\boldsymbol{\sigma}\right)$ with ϵ taking the role of the rest mass energy mc^2 and instead with a velocity $v_F = t\sqrt{3}a_0/2$, termed the *Fermi velocity*, as a replacement to the velocity of light c. Notice that, for the case of graphene, since $\epsilon = 0$, the electrons would behave as if they are massless. In this limit, the hBN low-energy dispersion can be written as the typical relativistic dispersion relation

$$E_{\text{TB}}(\boldsymbol{K}+\boldsymbol{p}) = \pm\sqrt{p^2v_F^2 + m_{\text{eff}}^2v_F^4}. \tag{5.19}$$

where m_{eff} is the effective mass of the electron at a given point near the valleys.

Although not captured in this simple tight-binding model, if one does some type of DFT to obtain a more complete electronic band structure, one could see that the hBN bands do actually cross between themselves (see, for example, Fig.(1) from [(39)]). This appears to be troublesome to our two-band time-dependent Hartree-Fock mean-field theory since certain transitions could occur between bands that are not accounted for in our model. However, these other intersecting bands corresponds to electronic states that are orthogonal to the ones we use in our two-band model and thus, will not interfere (i.e, even if we accounted for this other bands in our model, the form factors in Eqs.(3.19)-(3.24) would always give zero for transitions between those bands). However, this only applies for the hBN case since, if one was dealing instead with TMDs, one would need to account for at least three bands [(26)]. Furthermore, following the context of TMDs, one should also need to account for the spin-orbit coupling (SOC) where the effective Hamiltonian for such a system could be obtained by adding to Eq.(5.18) the term $H_{\text{SOC}} = t_s t s_z(\sigma_z - \mathbb{1})/2$ where t_s quantifies the spin-orbit coupling and $s_z = \pm 1$ labels the spin projection of the bands [(26), (40)].

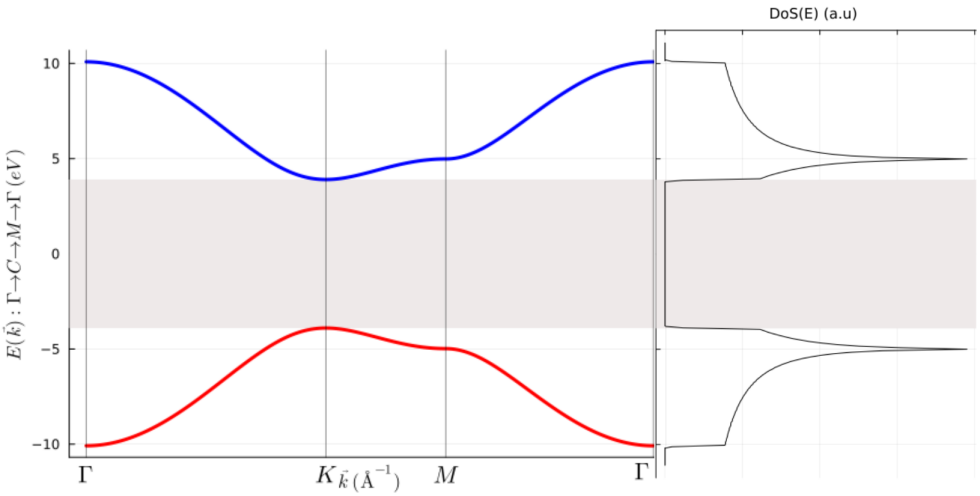

Figure 12: hBN electronic band structure from a nearest-neighbor tight-binding model accompanied by the density of the states. The dispersion goes along the symmetry path $\boldsymbol{k} : \Gamma \to K \to M \to \Gamma$ and was calculated using $\epsilon_g = 7.8$eV for the energy gap, $t = 3.1$eV for the hopping parameter and $a_0 = 1.42\sqrt{3}$Å for the honeycomb lattice length.

5.2 Isolated hBN excitonic properties

5.2.1 Bright exciton: singlet state for $Q = 0$

Firstly, we focus on the results, in and out of the TDA, for the (optical active) bright excitons, corresponding to the singlet state for a zero center of mass momentum exciton. Bright excitons, as opposed to dark excitons, dominate the optical properties of semiconductors since they can form/recombine from a single photon absorption/emission, making them the main focus of most of the literature on excitons.

The hBN NN TB electronic parameters to perform the calculation were: $e^2/\varepsilon_0 = 10^4/55.3$eVÅ, $\epsilon_g = 7.8$eV for the energy band-gap, $t = 3.1$eV for the hopping parameter, $a_0 = 1.42\sqrt{3}$Å for the honeycomb lattice length and $r_0 = 10$Å for the effective screening radius of the Rytova-Keldysh potential. We have selected these values because they correspond to those featured in the reference [(41)], with which we intend to make a comparative analysis of the results. Furthermore, following the convergence tests done in Sec.IV, we will be using a $\boldsymbol{k}$-sampling of $N_{\boldsymbol{k}} = 8649$ points with a cutoff norm of $|\boldsymbol{k}_{\text{cutoff}}| = 1.5$Å.

We show the results for the bright exciton energies in Fig.(13) and the results for the corresponding wave-function intensities in both reciprocal and real space in Fig.(15). The real space representation was

obtained via

$$\Psi^X_{cv}(\boldsymbol{R}+\boldsymbol{s}_\alpha, \boldsymbol{R}'+\boldsymbol{s}_\beta) = \frac{1}{N_{\boldsymbol{k}}}\sum_{\boldsymbol{k}} e^{i\boldsymbol{k}\cdot\left((\boldsymbol{R}+\boldsymbol{s}_\alpha)-\left(\boldsymbol{R}'-\boldsymbol{s}_\beta\right)\right)}\left(\phi^\beta_{\boldsymbol{k}v}\right)^* \phi^\alpha_{\boldsymbol{k}c}\Psi^X_{cv}(\boldsymbol{k}), \tag{5.20}$$

where $\boldsymbol{R}+\boldsymbol{s}_\alpha$ is the position of the electron in the real space lattice and $\boldsymbol{R}'+\boldsymbol{s}_\beta$ the position of the hole. In particular, the results shown in Fig.(15) have the hole fixed at the center boron atom in the origin of the referential, i.e $\boldsymbol{R}'=\boldsymbol{0}$ and $\boldsymbol{s}_\beta=\boldsymbol{s}_A$. Such expression can be obtained by considering the rDM in real space, $\rho_{\boldsymbol{R}\alpha,\boldsymbol{R}'\beta} = \left\langle c^\dagger_{\boldsymbol{R}',\beta}c_{\boldsymbol{R},\alpha}\right\rangle$ and inverse-Fourier transforming the creation/annihilation as in Eq.(3.2).

Analyzing the energy state results in Fig.(13), we observe a 1st and a 2nd lowest energy state having both the same energy 6.31eV. This states are then separated from the next higher energy state by 0.75eV. Subsequently, we obtained a 4th state considerably above the 3rd by 0.09eV and then a succession of two pairs of states, 5th and 6th, and 7th and 8th, having also the same energy (in pairs). We see that the lowest energy state is isolated from the higher energy states by a gap of 0.75eV, compared to the 0.25eV range between the 3st and 8nd states. Furthermore, the emergence of states having the same energies is to be expected due to valley parity symmetry where, and speaking from a low-energy scheme in the vicinity of $K^\pm$, each decoupled valley would contributes with its own eigenvalue. This, of course, assumes that inter-valley coupling in nearly absent which is not necessarily true as seen in the degeneracy lift between the 3rd and 4th state. Formally, we must sum the total wave-function intensities of the states that share the same energy, in order to preserve the natural symmetry of the (perfect) crystal lattice [(42)]. We do this in both the reciprocal and real intensities plots in Fig.(15) and denote the now single double-degenerated states by their pure constituents states in a square bracket notation. If we were to break the symmetry of the crystal, for example by slightly displacing one of the atoms, we would expect a splitting of these constituent states.

In order to understand if our calculations are trustworthy, we compare our results with those obtained in previous studies, specifically the references [(39), (41), (43), (44)]. We note that these comparisons are not meant to be one-to-one because the electronic parameters and methodology do not exactly match between the different articles and ours. Also, we note that in [(41)] refers not to the excitonic energies E_X but instead to their binding energy E_b with respect to the electronic energy gap, i.e $E_b = E_X - \epsilon_g$. Moreover, the order of appearance of the states may depend on whether the electronic calculations where based on a TB or an ab inition model. In particular, comparing with the results from [(39), (43)], we see that in our TB calculations the non-degenerated 3rd and 4th states, which are degenerate in their ab inition calculations, are switched with the degenerated 5th and 6th states, which are non-degenerate in their ab inition calculations. Beside this points, we consider the values and behavior of our results within reason

with the mentioned studies: a lowest energy state around ~ 6eV isolated from the higher energy states by a gap of ~ 1eV with three pairs of degenerated states and two non-degenerated states separated by ~ 0.1eV.

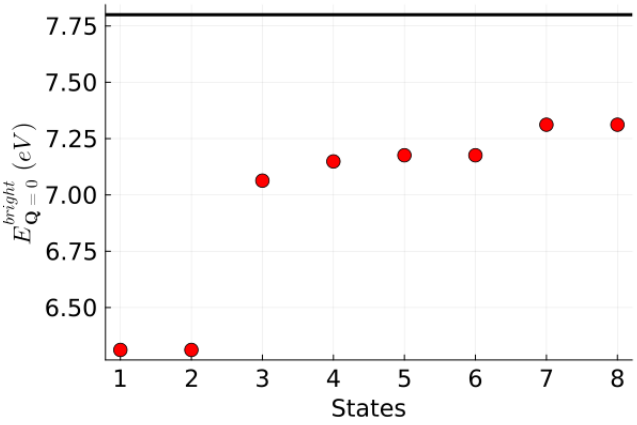

Figure 13: hBN bright exciton energies (corresponding to the optically active singlet state with center of mass momentum $\boldsymbol{Q} = 0$) for the first eight excitonic states. The energy values read as: 6.31eV for the 1st and 2nd state, 7.06eV for the 3rd, 7.15eV for the 4th, 7.18eV for the 5th and 6th and 7.31eV for the 7th and 8th. The parameters utilized for these results are made explicit in the beginning of Sec.V.B.I. Also, the calculation were performed within the TDA.

We now refer to the results for the wave-functions shown in Fig.(15). Since in the Wannier limit the exciton can be treated as a hydrogenoide model [(1)], we can classify and identify to some extent the excitonic states in an scheme borrowed from the 2D atomic orbitals terminology: (n, ℓ, m) with n the principal quantum number, $\ell = 0, ..., n-1$ the azimuthal quantum number and $m = -\ell, ...\ell$ the magnetic quantum number, denoting the states in the format $1s \equiv (1,0,0)$, $2s \equiv (2,0,0)$, $2p_0 \equiv (2,1,0)$, $2p_1 \equiv (2,1,1)$, etc... The probability densities of these hydrogenic atomic orbitals are shown in Fig.(14) as a visual reference guide.

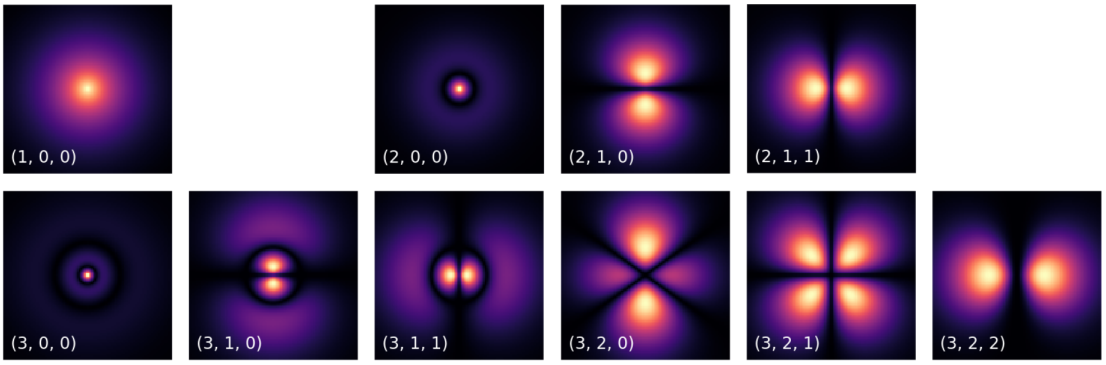

Figure 14: 2D probability density projection onto the plane $z\mathcal{O}y$ of the hydrogenic atomic orbitals in a (n, ℓ, m) representation. Image altered from [(45)]

Evaluating side by side the probability densities of the atomic orbitals in Fig.(14) with our results for the hBN bright excitonic in Fig.(15), one could assess through a visual comparison that the excitonic lower energy state resembles the $1s$ atomic orbital and that the higher excited state resembles the $2s$ atomic orbital. Although the comparison for the in-between states is not visually evident, possibly due to trigonal warping and/or hybridizing of the s and p behavior, we can at least assess that, since they are strikingly similar, they must belong to the same orbital family. Given they are only three different states on that orbital family, #3, #4 and #[5,6], it must correspond to the $2p$ orbital family. Thus, we assess the #[5,6] as being the $2p_0$ state and the non-degenerated #3 and #4 states as being the $2p_{-1}$ and $2p_{+1}$ states respectively. Whilst not necessarily common, the $2s$ level is indeed found to be above the $2p$ levels.

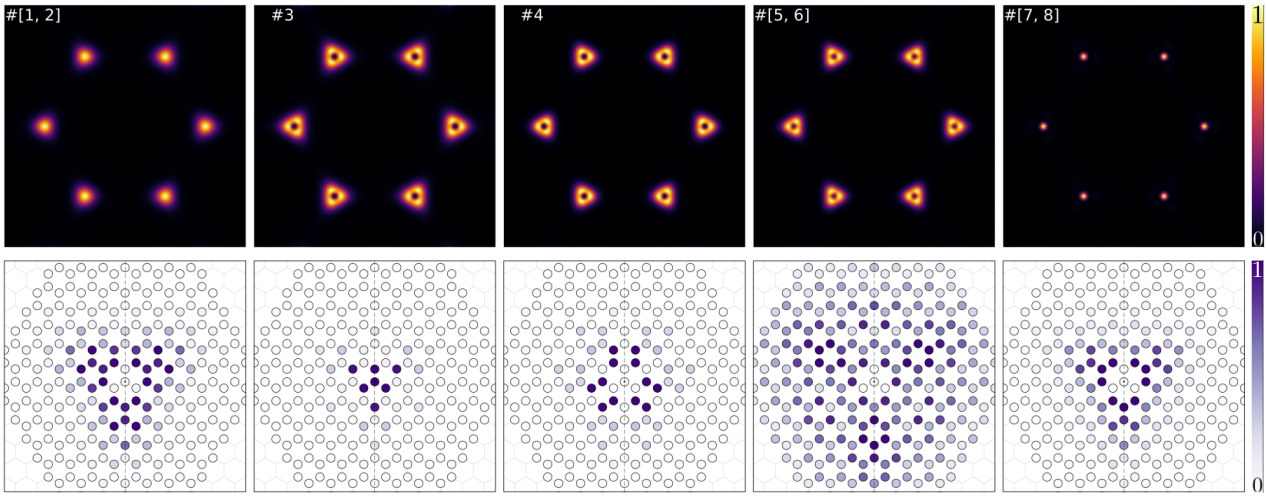

Figure 15: hBN bright exciton (normalized) wave-function intensities $|\psi_X|^2$ for the first eight excitonic states. The representation in done in **(1st row)** reciprocal space and in **(2nd row)** real space. The single double-degenerated states are constructed by summing the intensities of the states that share the same energy, in order to preserve the natural symmetry of the crystal lattice. In the real space representation, the hole (denoted by a small black dot) is fixed at the center boron atom in the origin of the referential.

While this hydrogenoide classifications of the excitonic states is useful, it its the genuine triangular point group symmetry C_{3v} that should formally describe the excitonic states. The C_{3v} symmetry group is described by three different classes: the identity E, two 3-fold rotation symmetries C_3 and three mirror symmetries σ_v, reflecting along the axis of highest rotational symmetry. It decomposes into three irreducible representations (irreps): the single-degenerated symmetric irrep A_1, the single-degenerated *anti*-symmetric irrep A_2, characterized by an odd character for the σ_v reflections, and the double-degenerated irrep E [(46)]. Immediately, we can identify the double degenerate $2s$, $2p$ and $2p_0$ as being irreducible presented by E. It then only remains to make the correspondence between the $2p_{+1}$ and $2p_{-1}$ states and the irreps A_1 or A_2. For this, we do an intensity-phase representation of the excitonic wave-function where each $\boldsymbol{k}$-point of the discretized 1BZ has an associated color value given by to the wave-function phase and an opacity proportional to the normalized intensity, as shown in Fig.(16). From here, and ignoring the numerical noise, it is clear that the 3rd state, corresponding to the $2p_{-1}$ state, is symmetric with respect to a highest rotational symmetry axis, in particular the k_y-axis, and therefore is irreducible represented by the A_1 irrep. One the other hand, the 4th state, corresponding to the $2p_{+1}$ state, is anti-symmetric with respect to the k_y-axis and is instead irreducible represented by the A_2 irrep. However, contrary to our findings, in [(39)], which also studied the excitonic states in terms of the C_{3v} symmetric, found the anti-symmetric state to be instead the first of the non-degenerate states.

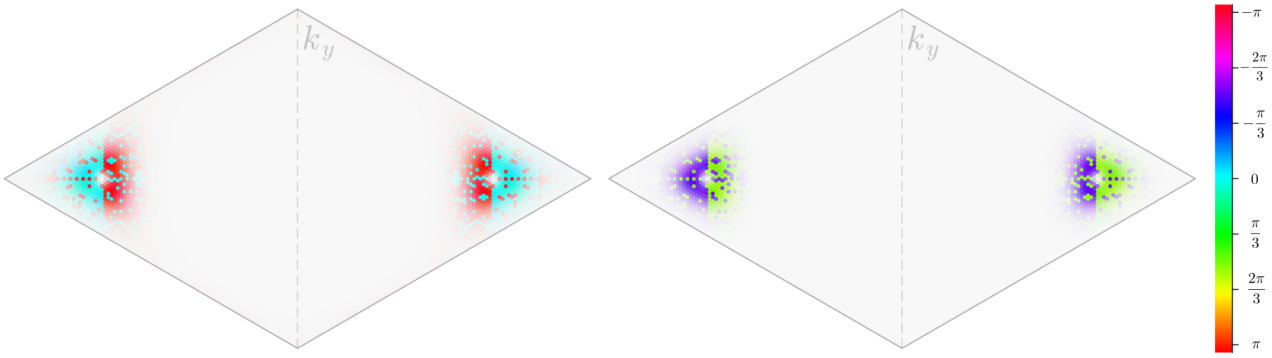

Figure 16: Intensity-phase representation in reciprocal space of the hBN bright exciton wave-function for the 3rd and 4th states. Each $\boldsymbol{k}_i$ point of the discretized 1BZ grid has an associated color value given by the wave-function phase and an opacity directly proportional to the normalized intensity.

5.2.2 Excitonic band structure

We now concern ourselves with the whole excitonic band structure for both the singlet and triplet spin-states. Although one could argue that the excitonic band structure, specially for the triplet states, is not necessarily interesting because dark excitons do not have a photoluminescence response and thus do not contribute for the optical properties of the semiconductor, the particularity of them not being able to easily recombine into a single photon, either because the electronic transition is non-vertical or spin-forbidden, also means that they have much longer radiative lifetimes than bright excitons which makes them attractive for different reasons, as talked about in the introduction.

In order to build the excitonic band structure we need to perform the calculations for the first eight energy states for various exciton center of mass momentum $\boldsymbol{Q}$. Particularly, we consider the path $\boldsymbol{Q}$: $\Gamma \rightarrow K \rightarrow M \rightarrow \Gamma$ with $N_{\boldsymbol{Q}} = 32$ points. For this, the total length $L_{\boldsymbol{Q}}$ of the path was first divided into $N_{\boldsymbol{Q}} - 2$ equidistant intervals $\Delta\boldsymbol{Q} \approx 0.134\text{Å}^{-1}$ which are then distributed along each of the three path directions. Since the lengths of each are not multiples of each other the K and M point are not exactly hit so we just manually incorporate them into the path (hence the previous -2 in $N_{\boldsymbol{Q}} - 2$).

For this choice of $\boldsymbol{Q}$ points, the complete excitonic band structure is as shown in Fig.(17). We note that, in this figure, the lines in-between the same state energies for consecutive $\boldsymbol{Q}$-points were added as a visual guide and that the actual scatter points had to be omitted because it would made the display a lot more convoluted and impossible to read. Firstly, we comment on the overall structure and degeneracies of the singlet states, then on the spin-splitting comparing the singlet and triplet state and finally on the validity of the Tamm-Dancoff approximation. We focus our analysis mainly on the high symmetry points of the excitonic band structure, $\boldsymbol{Q} = K$ and $\boldsymbol{Q} = M$.

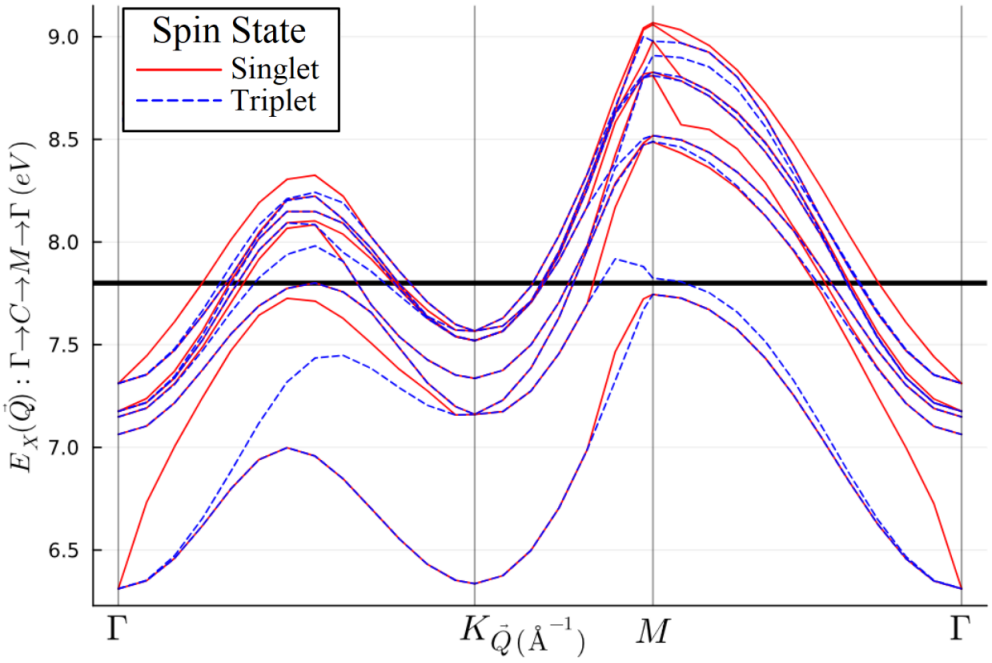

Figure 17: hBN excitonic band structure for both the spin-singlet and spin-triplet states, for the first eight excitonic states. The dispersion goes along the symmetry path $\boldsymbol{Q} : \Gamma \to K \to M \to \Gamma$ for $N_{\boldsymbol{Q}} = 32$ different excitonic center of mass momentum $\boldsymbol{Q}$. It was used a sampling of $N_{\boldsymbol{k}} = 8649$ electronic $\boldsymbol{k}$-points and a cutoff norm of $|\boldsymbol{k}_{\text{cutoff}}| = 1.5$Å. The lines are added as a visual guide and the actual scatter points had to be omitted to avoid a convoluted display. The thick black line corresponds to the hBN electronic band-gap energy. The parameters utilized for these results are made explicit in the beginning of Sec.V.B.I. Also, the calculation were performed within the TDA.

Inspecting Fig.(17), we see that the valley-degeneracy of the bright excitons states are immediately lifted, which is to be expected since for a non-zero center of mass momentum exciton the C_{3v} symmetry is broken. Furthermore, notice that for $\boldsymbol{Q} = K$ the states group themselves once more into double-degenerated states although not in the initial $\boldsymbol{Q} = 0$ configuration. Analysis the first plot of Fig.(18), where we show the energy values (vs the energy state) specifically for the $\boldsymbol{Q} = K$ case, we clearly see that the 2nd state separates from the 1st state ending up degenerating instead with the 3rd state. This in turns leaves the 4th state isolated since the pairs 5th and 6th, and 7th and 8th stay degenerated as in the $\boldsymbol{Q} = 0$ case. More importantly, see that this large-momentum excitons actually have its energy very similar to those near zero momentum. In particular, the $\boldsymbol{Q} = K$ lowest state stays a shy ~ 0.02eV above the $\boldsymbol{Q} = 0$ lowest-state. Perhaps, depending on the value of the exchange term V, controlled by the electronic parameters, the lowest energy excitons could occur at $\boldsymbol{Q} = K$, corresponding to a indirect gap excitonic system.

Concerning the spin-structure, we found that, for the zero center of mass momentum exciton, the singlet and triplet state do not appear to have any differences, nor a spin splitting, nor a spin inversion of levels. This, however, contradiction the ab inition results from [(43)] where, by turning on the (repulsive) exchange interaction (which corresponds to go from the triplet to the singlet state), the energy of their 4th state moved substantially. The fact that we do not capture such phenomenon could be justified due to the single-particle Bloch functions being approximated in a tight-binding model. This is somewhat corroborated since in that very same study, besides the ab inition calculation, they also tested a tight-binding model that also does not capture such inversion of levels. In our particular case, one possible explanation can be attributed to the use of the ultra-localized electronic orbitals approximation (as described in Section III.A) while the excitons are not genuinely in the Wannier limit, as it can be seen in the real space representation in the second row of Fig.(15). In other words, if we are assuming the electrons to interact only at long distances, the corresponding excitonic wave-function must be extensive enough to validate such approximation, otherwise the electronic interaction cannot be straightforwardly described by the Hamiltonian in Eq.(3.1) because $\boldsymbol{R}_4, \varsigma_4 \approx \boldsymbol{R}_1, \varsigma_1$ and $\boldsymbol{R}_3, \varsigma_3 \approx \boldsymbol{R}_2, \varsigma_2$ is simply not true. One the other hand, while there were no differences between the singlet and triplet states for $\boldsymbol{Q} = 0$, looking once more at Fig.(17), we see that the spin-splitting is noticeable for other center of mass momenta, especially for the 2nd state. In fact, the 2nd state seems to have a much more spin structure dependent behavior overall. In particular, we see that partway along the path $\boldsymbol{Q} : \Gamma \to K$ the spin-splitting is highly relevant but ends up "closing" near the valley, coming back to zero at its center. Additional, along the path $\boldsymbol{Q} : K \to M$, the singlet and triplet states stay very close to each other (energetically speaking) and only near the 1BZ edge at $\boldsymbol{Q} = M$ do they begin to considerably split. In the remaining path $\boldsymbol{Q} : M \to \Gamma$ the splitting stays considerable large for most of the way, closing somewhat abruptly only at $\boldsymbol{Q} = \Gamma$.

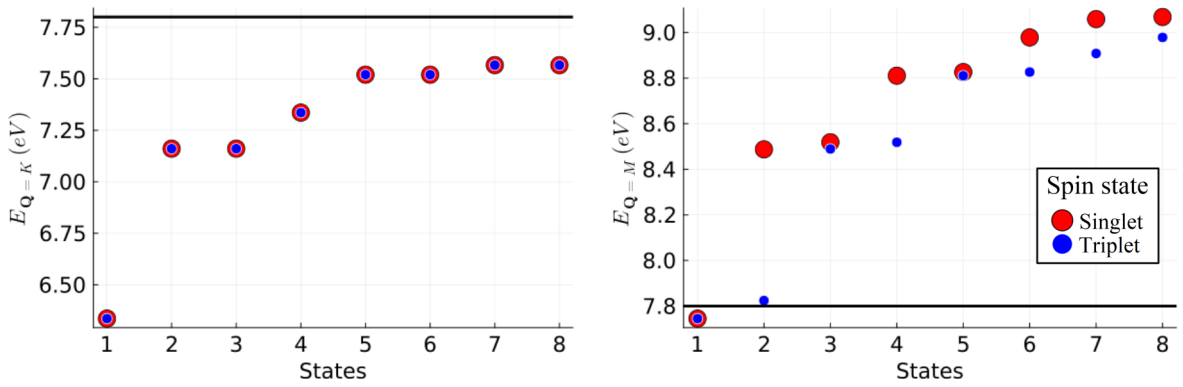

Figure 18: Comparing the first eight excitonic energy with excitonic center of mass momentum $\boldsymbol{Q} = K$ and $\boldsymbol{Q} = M$ for both the spin-singlet and spin-triplet states. The thick black line corresponds to the hBN electronic band-gap energy. The parameters utilized for these results are made explicit in the beginning of Sec.V.B.I. Also, the calculation were performed within the TDA.

In the context of the hydrogenoide comparison, let us extend our discussion beyond the optical active states, and analyze also the excitonic wave-functions for $\boldsymbol{Q} = K$. Since its energy values resemble those of the bright excitons, maybe is excitonic states canbe similar to the atomic orbitals. In Fig.(15) we show the wave-functions intensities for its first eight states and indeed it is possible to see some similarities when comparing these results with the probability densities of the atomic orbitals in Fig.(14). For example, the 2nd and 3rd state of the $\boldsymbol{Q} = K$ exciton bare a great resemblance to the $2p_{-1}$ and $2p_{+1}$ orbitals states, not only because of their shape but also because of their tilt alignment with the reciprocal lattice vectors $\boldsymbol{b}_1$ and $\boldsymbol{b}_2$ (analogously to the alignment to the x or y axis in the atomic orbitals). From the excitonic band structure in Fig.(17) we can see that these $2p_{-1}/2p_{+1}$ $\boldsymbol{Q} = K$ states are similar in energy with the not so obvious $2p_{-1}/2p_{+1}$ $\boldsymbol{Q} = 0$ states, which gives further legitimacy to our initial classification. See that this energy similarity also happens for the $2s$ states when comparing the #[7,8] $\boldsymbol{Q} = 0$ state with the 4th $\boldsymbol{Q} = K$ state. To conclude this hydrogenoide classifications of the excitonic states we mention that the $\boldsymbol{Q} = K$ 5th and 6th state resemble respectively the $3d_{-1}$ and $3d_{+1}$ atomic orbitals and that the $\boldsymbol{Q} = K$ 7th and 8th state resemble respectively the $3d_{-2}$ and $3d_{+2}$.

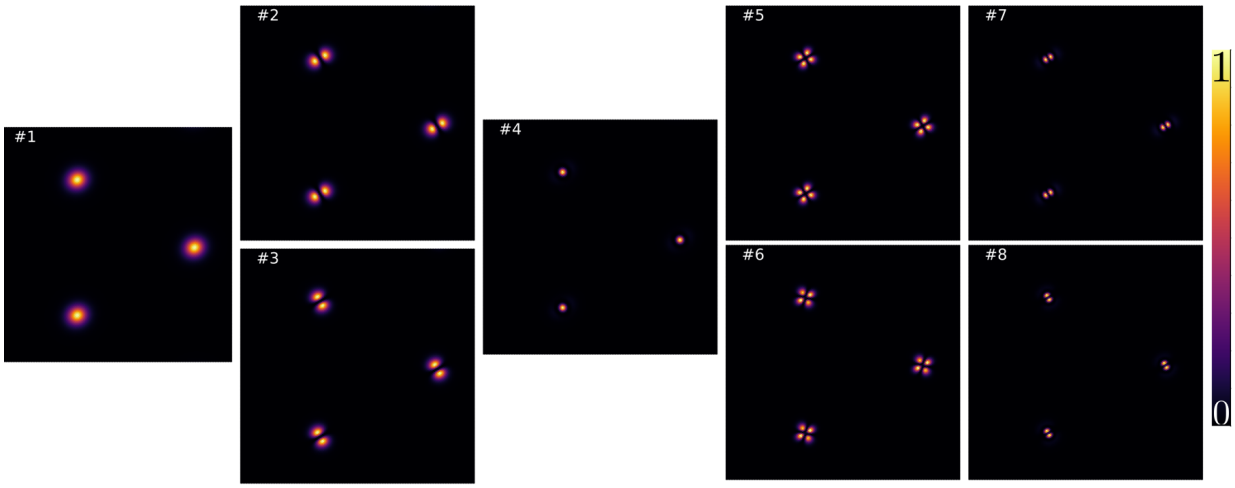

Figure 19: hBN singlet excitonic (normalized) wave-function intensities $|\psi_X^n|^2$ of the first eight excitonic states for excitonic center of mass momentum $\boldsymbol{Q} = K$, in reciprocal space.

To test the reliability of the Tamm-Dancoff approximation, we calculated the excitonic energies for the main three symmetry points $\boldsymbol{Q} = \Gamma, K, M$ for both the singlet and triplet states in and out the TDA. We found that the energies calculated with the complete Hamiltonian bare no difference whatsoever from the TDA calculations. However, for the $\boldsymbol{Q} = M$ singlet state we obtained some unexpected behavior on the higher energy states. The sequence of energies for the 6th to 8th states within the TDA reads 8.98, 9.02, 9.06eV while for the complete Hamiltonian it reads 8.98, 9.06, 9.07eV. One possible explanation is that the complete Hamiltonian calculations are actually less exact and didn't capture the 9.02eV state due to the usage of approximated eigenvalues algorithms, as discussed in the numerical details section. In this sense, the 9.07eV energy would actually correspond to the 9th state within the TDA and the 9.02eV state ended up just being skipped. Unfortunately, the calculation were only made up to the 8th state and we cannot confirm exactly if this is the case. From these results, we conclude that, indeed, the TDA is not only admissible but of much help since it greatly reduces the computational power needed to solve the eigen-problem without possibly introducing additional errors due to approximated eigenvalues algorithms.

5.3 hBN-metal hetero-structure excitonic properties

As a follow-up to the isolated hBN monolayer case, consider a system where the hBN monolayer in no longer surrounded by vacuum but is instead inside a dielectric which is in close contact with a metal such that there is a distance d between the 2D material and the metal, as depicted in Fig.(20). We study the effects of the metal screening on the excitonic energies as a function of the distance d. We note to the article [(47)] which examine the effects of material thickness and surrounding dielectric medium on the

Coulomb interactions.

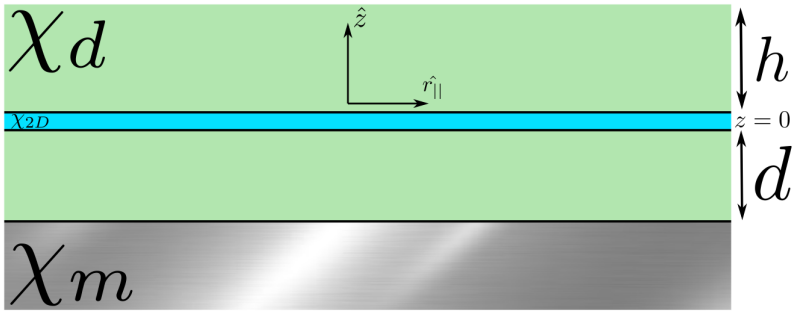

Figure 20: Hetero-structure of a 2D material inside a dielectric which is in close contact with a metal.

As derived in Appendix B.2, the effective electron-hole interaction in close proximity of a bulk metal is instead described by the metal screened Rytova-Keldysh potential

$$\mathrm{W}_m(\boldsymbol{k}_{||}) = \frac{e}{2\varepsilon_0}\frac{1}{k_{||}}\frac{1}{r_0 k_{||} + \frac{1}{2}\frac{e^{k_{||}d}}{\sinh(k_{||}d)}}, \tag{5.21}$$

where, once again, $r_0 = \chi_{2D}/2$ is the effective screening radius with χ_{2D} the 2D susceptibility and d is the distance between the hBN monolayer and the metal. Note that this expression is only valid if we consider the metal to be perfect, $\chi_m \to -\infty$, and the dielectric to be actually a vacuum $\chi_d = 0$. Furthermore, as discussed in Section III.D, the Hartree term potential should not be screened by to the electrons in a polarizable 2D semiconductor since this screening it is already accounted for in a RPA sense. However, the screening due to the presence of the metal is an independent source of screening and as such, it should be imposed also in the Hartree term. Therefore, turning off the over-counted 2D polarization screening in the Hartree term we have the metal-screened Coulomb potential

$$\mathrm{V}_m(\boldsymbol{k}_{||}) = \frac{e}{2\varepsilon_0}\frac{1}{k_{||}}\frac{1}{\frac{1}{2}\frac{e^{k_{||}d}}{\sinh(k_{||}d)}}. \tag{5.22}$$

Both this potentials are shown in Fig.(21) as a function of d. As we move the metal away from the hBN monolayer the metal screening is progressively less apparent until the limiting case where there is effectively zero screening. In this limiting case we return to the description of the potentials as in Eqs.(3.31) and (3.32).

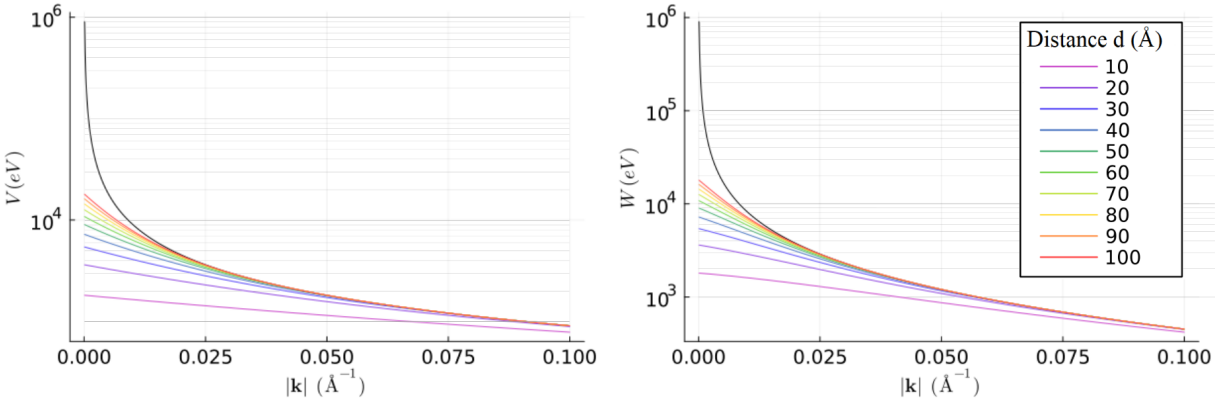

Figure 21: Metal screened potentials in a log10 scale as a function of the distance d between the hBN monolayer and the metal The bare potential, corresponding to $d \to \infty$, is colored black. The utilized effective screening radius reads $r_0 = 10$Å.

In Fig.(22), we repeat the calculations for the first eight energy levels of the bright exciton, (corresponding to the singlet state with $\boldsymbol{Q} = 0$) but instead with the metal screened potentials as a function of the distance d between the hBN monolayer and the bulk metal in Eqs.(5.21) and (5.22). As one would expect, the greater the metal screening, the lower the excitonic binding energies, $E_b = \epsilon_g - E_X$. In a crude explanation, this happens because the electric field lines that go outside the hBN and pierce the metal hamper the electron-hole interaction making them less attracted to each other. In the limiting case where the metal is so far away that its screening has no effect on the hBN monolayer, the excitonic energies tend to the isolated monolayer values.

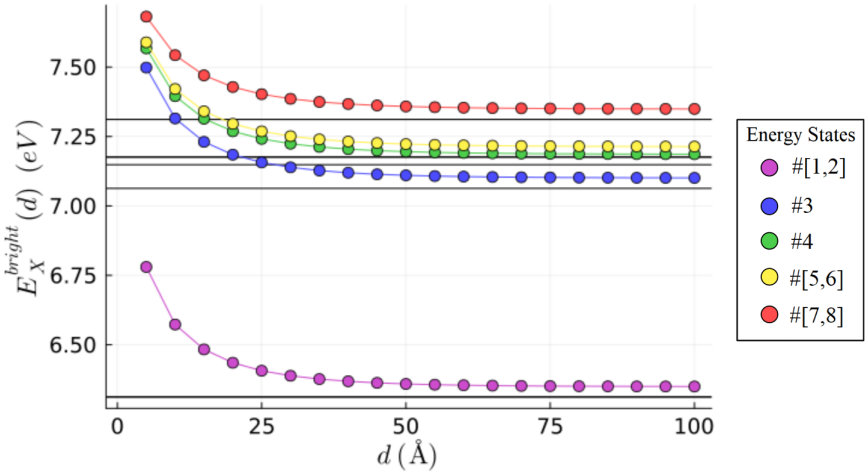

Figure 22: hBN-metal hetero-structure bright exciton energies as a function of the distance d between the hBN monolayer and the bulk metal, for the first eight excitonic states. The distance d increment is 5Å. The parameters utilized for these results are made explicit in the beginning of Sec.V.B.I. Also, the calculation were performed within the TDA.

Chapter 6

Conclusions and future work

In this work, we showed how collective excitations can emerge from a many-body system of interacting particles in a time-dependent reduced density matrix (rDM) Hartree-Fock mean-field theory.

We studied the linear response of a system of electrons from a many-body perturbation theory by inspecting the time evolution of the system's rDM. To this end, and as a mean to simplify the rDM's equation of motion, two main approximations were made: a mean-field decoupling and the specification to an insulator at zero temperature. It was shown that evaluation of the lowest order correction to the rDM due to a time-dependent perturbation can be reduced to the solution of the generalized eigen-problem for the effective two-particle Hamiltonian for an interacting electron-hole pair. We then particularized this formalism to the case of hBN structures, describing the electronic single-particle Bloch states in a nearest-neighbor tight-binding model, considering atomistic electron-electron interactions.

Solving the generalized eigen-problem numerically proves to be a simple yet effective method to calculate excitonic energies and wave-functions, in the sense that its implementations is straightforward and takes a relatively small computation time to obtain results up to two decimal places which are within reason when comparing to more challenging techniques. Moreover, this method is quite versatile in the sense that it has plenty of room for improvements, for example, we could account for spin-orbit effects or for more than just two bands; or we could study other Van der Waals hetero-structures with different electrostatic potentials.

Concerning the results of the first eight bright (spin-singlet with nill excitonic center of mass momentum) exciton states for a isolated hBN monolayer, we obtained an energy of 6.32eV for the lowest energy state and observed the emergence of pairs of states having the same energies, which is to be expected due to valley symmetry. Furthermore, we tested the validity of the Tamm-Dancoff Approximation and found no difference whatsoever on the excitonic energies calculated neglecting or not the coupling block, thus proving its efficiency. Concerning the whole excitonic band structure, we confirm that the bright double-degenerated states immediately break apart for non-zero excitonic center of mass; and that the Hartree

term contribution does impact significantly the spin-splinting of the singlet and triplet states. Moreover, we considered the case of a hBN-metal hetero-structure in order to study the effects of (bulk) metal screening on the excitonic energy levels and confirmed that, as the metal gets closer to the hBN monolayer and the screening gets more intense, the lower the excitonic binding energies get.

As a continuation of this work, the next step would be to take the obtained excitonic energies and eigenvalues and calculate the optical conductivity following the discussion of Sec.II.C.b. Moreover, we could calculate the expected life-time of the excitons, for example, through decay into the electromagnetic modes of a planar laser cavity. As future lines of research, it would be interesting to apply the formalism of this work to other 2D structures, such as TMDs within three-band model or even more. Indeed, even within the context of hBN, there still remains numerous ideas to explore. How does the excitonic energies vary with the effective screening radius? Or with a dielectric environment other than the vacuum? What are the effects on the excitonic band structure due to spin-orbit coupling? What about other structures such as bilayers, or twisted bilayers, or periodic alternating metal-dieletric-hBN structures?

Bibliography

[1] “Knox, r. s. (1983). introduction to exciton physics. in collective excitations in solids (pp. 183-245). boston, ma: Springer us.,”

[2] “Dvorak, m., wei, s. h., wu, z. (2013). origin of the variation of exciton binding energy in semiconductors. physical review letters, 110(1), 016402.,”

[3] “Egri, i. (1979). a simple model for the unified treatment of wannier and frenkel excitons. journal of physics c: Solid state physics, 12(10), 1843.,”

[4] “N. rytova, moscow univ. phys. bull. 3, 30 (1967),”

[5] “L.v. keldysh, sov. j. exp. theor. phys. lett. 29, 658 (1979),”

[6] “Cudazzo, p., sponza, l., giorgetti, c., reining, l., sottile, f., gatti, m. (2016). exciton band structure in two-dimensional materials. physical review letters, 116(6), 066803.,”

[7] “Mueller, t., malic, e. (2018). exciton physics and device application of two-dimensional transition metal dichalcogenide semiconductors. npj 2d materials and applications, 2(1), 29.,”

[8] “Massicotte, m., vialla, f., schmidt, p., lundeberg, m. b., latini, s., haastrup, s., ... koppens, f. h. (2018). dissociation of two-dimensional excitons in monolayer wse2. nature communications, 9(1), 1633.,”

[9] “Wang, g., chernikov, a., glazov, m. m., heinz, t. f., marie, x., amand, t., amp; urbaszek, b. (2018). colloquium: Excitons in atomically thin transition metal dichalcogenides. reviews of modern physics, 90(2).,”

[10] “Quintela, m. f., peres, n. m. (2020). a colloquium on the variational method applied to excitons in 2d materials. the european physical journal b, 93, 1-16.,”

[11] “Kalugin, n. g., rostovtsev, y. v. (2009). ” dark” and” bright” excitons in carbon nanotubes: New media for quantum optics. journal of nanoelectronics and optoelectronics, 4(3), 302-306.,”

[12] “Berkelbach, t. c., hybertsen, m. s., reichman, d. r. (2015). bright and dark singlet excitons via linear and two-photon spectroscopy in monolayer transition-metal dichalcogenides. physical review b, 92(8), 085413.,”

[13] “Ye, z., cao, t., o’brien, k., zhu, h., yin, x., wang, y., ... zhang, x. (2014). probing excitonic dark states in single-layer tungsten disulphide. nature, 513(7517), 214-218.,”

[14] “Loh, k. p. (2017). brightening the dark excitons. nature nanotechnology, 12(9), 837-838.,”

[15] “Zhou, y., scuri, g., wild, d. s., high, a. a., dibos, a., jauregui, l. a., ... park, h. (2017). probing dark excitons in atomically thin semiconductors via near-field coupling to surface plasmon polaritons. nature nanotechnology, 12(9), 856-860.,”

[16] “Zhang, s., li, b., chen, x., ruta, f. l., shao, y., sternbach, a. j., ... basov, d. n. (2022). nano-spectroscopy of excitons in atomically thin transition metal dichalcogenides. nature communications, 13(1), 542.,”

[17] “Kim, y., kim, j. (2021). near-field optical imaging and spectroscopy of 2d-tmds. nanophotonics, 10(13), 3397-3415,”

[18] “Saiki, t., matsuda, k., nomura, s., mihara, m., aoyagi, y., nair, s., takagahara, t. (2004). nano-optical probing of exciton wave-functions confined in a gaas quantum dot. microscopy, 53(2), 193-201.,”

[19] “Zhang, x. x., cao, t., lu, z., lin, y. c., zhang, f., wang, y., ... heinz, t. f. (2017). magnetic brightening and control of dark excitons in monolayer wse2. nature nanotechnology, 12(9), 883-888.,”

[20] “Gelly, r. j., renaud, d., liao, x., pingault, b., bogdanovic, s., scuri, g., ... lončar, m. (2022). probing dark exciton navigation through a local strain landscape in a wse2 monolayer. nature communications, 13(1), 232.,”

[21] “Jiang, j., pachter, r. (2022). analysis of localized excitons in strained monolayer wse 2 by first principles calculations. nanoscale, 14(31), 11378-11387.,”

[22] “Darlington, t. p., carmesin, c., florian, m., yanev, e., ajayi, o., ardelean, j., ... schuck, p. j. (2020). imaging strain-localized excitons in nanoscale bubbles of monolayer wse2 at room temperature. nature nanotechnology, 15(10), 854-860.,”

[23] “Blase, x., duchemin, i., jacquemin, d., loos, p. f. (2020). the bethe–salpeter equation formalism: From physics to chemistry. the journal of physical chemistry letters, 11(17), 7371-7382.,”

[24] “Strinati, g. (1988). application of the green’s functions method to the study of the optical properties of semiconductors. la rivista del nuovo cimento (1978-1999), 11(12), 1-86.,”

[25] “Salpeter, e. e. (2008). bethe-salpeter equation–the origins,”

[26] “Liu, gui-bin shan, wen-yu yao, yugui yao, wang xiao, di. (2013). three-band tight-binding model for monolayers of group-vib transition metal dichalcogenides. physical review b. 88. 10.1103/physrevb.88.085433.,”

[27] “Molina-sánchez, a., sangalli, d., hummer, k., marini, a., wirtz, l. (2013). effect of spin-orbit interaction on the optical spectra of single-layer, double-layer, and bulk mos 2. physical review b, 88(4), 045412.,”

[28] “Benedict, l. x. (2002). screening in the exchange term of the electron-hole interaction of the bethe-salpeter equation. physical review b, 66(19).,”

[29] “Qiu, d. y., da jornada, f. h., louie, s. g. (2021). solving the bethe-salpeter equation on a subspace: Approximations and consequences for low-dimensional materials. physical review b, 103(4), 045117.,”

[30] “Cottam, m. g., haghshenasfard, z. (2020). many-body theory of condensed matter systems: An introductory course. cambridge university press.,”

[31] “Jishi, r. a. (2013). feynman diagram techniques in condensed matter physics. cambridge university press.,”

[32] “Lipavský, p., Špička, v., velický, b. (1986). generalized kadanoff-baym ansatz for deriving quantum transport equations. physical review b, 34(10), 6933.,”

[33] “Rohlfing, michael louie, steven. (2000). electron-hole excitations and optical spectra from first principles. phys. rev. b. 62. 10.1103/physrevb.62.4927,”

[34] “Andrilli, s., hecker, d. (2022). elementary linear algebra. academic press.,”

[35] “Arnoldi, w. e. (1951). the principle of minimized iterations in the solution of the matrix eigenvalue problem. quarterly of applied mathematics, 9(1), 17-29.,”

[36] “Gazzola, s., nagy, j. g. (2014). generalized arnoldi–tikhonov method for sparse reconstruction. siam journal on scientific computing, 36(2), b225-b247.,”

[37] “Cassabois, g., valvin, p., gil, b. (2016). hexagonal boron nitride is an indirect bandgap semiconductor. nature photonics, 10(4), 262-266.,”

[38] “Ishigami, m., aloni, s., zettl, a. (2003, december). properties of boron nitride nanotubes. in aip conference proceedings (vol. 696, no. 1, pp. 94-99). american institute of physics.,”

[39] “F. ferreira, a. j. chaves, n. m. r. peres, and r. m. ribeiro, ”excitons in hexagonal boron nitride single-layer: a new platform for polaritonics in the ultraviolet,” j. opt. soc. am. b 36, 674-683 (2019),”

[40] “Scharf, b., xu, g., matos-abiague, a., Žutić, i. (2017). magnetic proximity effects in transition-metal dichalcogenides: converting excitons. physical review letters, 119(12), 127403.,”

[41] “Quintela, mauricio henriques, j. peres, nuno. (2022). theoretical methods for excitonic physics in two-dimensional materials: A tutorial.,”

[42] “Wirtz, l., marini, a., grüning, m., attaccalite, c., kresse, g., rubio, a. (2008). comment on “huge excitonic effects in layered hexagonal boron nitride”. physical review letters, 100(18), 189701.,”

[43] “Galvani, thomas paleari, fulvio miranda, henrique molina-sánchez, alejandro wirtz, ludger latil, sylvain amara, hakim ducastelle, françois. (2016). excitons in boron nitride single layer. physical review b. 94. 10.1103/physrevb.94.125303.,”

[44] “Wu, f., qu, f., macdonald, a. h. (2015). exciton band structure of monolayer mos 2. physical review b, 91(7), 075310.,”

[45] “Qijing zheng, matplotlib: Hydrogen wave function,”

[46] “Dresselhaus, m. s., dresselhaus, g., jorio, a. (2007). group theory: application to the physics of condensed matter. springer science business media.,”

[47] “Flórez, f. g., siebbeles, l. d., stoof, h. t. c. (2020). effects of material thickness and surrounding dielectric medium on coulomb interactions and two-dimensional excitons. physical review b, 102(12), 125303.,”

Appendices

Appendix A
Details on the theoretical description of excitons

A.1 Symmetry properties of the interaction matrix elements

We show the details on how to arrive at the symmetry properties presented in Eqs.(2.10) and (2.11) of the interaction matrix elements, as described in Eq.(2.9), of the many-body system of electron Hamiltonian in Eq.(2.7). From the imposed symmetry $V(\boldsymbol{r}-\boldsymbol{r}') = V(\boldsymbol{r}'-\boldsymbol{r})$, we obtain

$$\begin{aligned} V_{\gamma\delta}^{\alpha\beta} &= \int d^3\boldsymbol{r} d^3\boldsymbol{r}' \phi_\alpha^*(\boldsymbol{r})\, \phi_\beta^*(\boldsymbol{r}') V(\boldsymbol{r}-\boldsymbol{r}') \phi_\gamma(\boldsymbol{r}') \phi_\delta(\boldsymbol{r}) \\ &= \int d^3\boldsymbol{r} d^3\boldsymbol{r}' \phi_\alpha^*(\boldsymbol{r}')\, \phi_\beta^*(\boldsymbol{r}) V(\boldsymbol{r}'-\boldsymbol{r}) \phi_\gamma(\boldsymbol{r}) \phi_\delta(\boldsymbol{r}') \\ &= \int d^3\boldsymbol{r} d^3\boldsymbol{r}' \phi_\alpha^*(\boldsymbol{r}')\, \phi_\beta^*(\boldsymbol{r}) V(\boldsymbol{r}-\boldsymbol{r}') \phi_\gamma(\boldsymbol{r}) \phi_\delta(\boldsymbol{r}') \\ &= \int d^3\boldsymbol{r} d^3\boldsymbol{r}' \phi_\beta^*(\boldsymbol{r}) \phi_\alpha^*(\boldsymbol{r}')\, V(\boldsymbol{r}-\boldsymbol{r}') \phi_\delta(\boldsymbol{r}') \phi_\gamma(\boldsymbol{r}) \\ &= V_{\delta\gamma}^{\beta a}. \end{aligned} \tag{A.1}$$

Similarly

$$\begin{aligned} \left(V_{\gamma\delta}^{\alpha b}\right)^* &= \int d^3\boldsymbol{r} d^3\boldsymbol{r}' \phi_\alpha(\boldsymbol{r})\, \phi_\beta(\boldsymbol{r}') V(\boldsymbol{r}-\boldsymbol{r}') \phi_\gamma^*(\boldsymbol{r}') \phi_\delta^*(\boldsymbol{r}) \\ &= \int d^3\boldsymbol{r} d^3\boldsymbol{r}' \phi_\delta^*(\boldsymbol{r}) \phi_\gamma^*(\boldsymbol{r}') V(\boldsymbol{r}-\boldsymbol{r}') \phi_\delta(\boldsymbol{r}') \phi_\alpha(\boldsymbol{r}) \\ &= V_{\beta\alpha}^{\delta\gamma} \\ &= V_{\alpha\beta}^{\gamma\delta} \end{aligned} \tag{A.2}$$

A.2 Commutators and Anti-commutator properties

We show the details on how to arrive at the commutator presented in Eqs.(2.19) and Eqs.(2.20). We evaluate each commutator individually given the fermionic and commutator operator properties,

$$\left\{c_a, c_b^\dagger\right\} = \left\{c_b^\dagger, c_a\right\} = \delta_{ab} \tag{A.3}$$

$$\{c_a, c_b\} = \left\{c_b^\dagger, c_a^\dagger\right\} = 0 \tag{A.4}$$

Foremost, we derive commutator and anti-commutator properties for various numbers of operator in a general fashion and then apply then to the explicit case at hand. The commutator and anti-commutator operate, respectively as,

$$[A, Z] = AZ - ZA \tag{A.5}$$

$$\{A, Z\} = AZ + ZA. \tag{A.6}$$

From here it follows that

$$\{A, Z\} = \{Z, A\} \tag{A.7}$$

$$[A, Z] = -[Z, A] \tag{A.8}$$

Consequently we have that

$$\begin{aligned}
[AB, Z] &= ABZ - ZAB \\
&= ABZ - ZAB + AZB - AZB \\
&= A(BZ + ZB) - (ZA + AZ)B \\
&= A\{B, Z\} - \{Z, A\}B
\end{aligned} \tag{A.9}$$

and

$$\begin{aligned}
[AB, Z] &= ABZ - ZAB \\
&= ABZ - ZAB - AZB + AZB \\
&= A(BZ - ZB) - (ZA - AZ)B \\
&= A[B, Z] - [Z, A]B
\end{aligned} \tag{A.10}$$

Using both of the properties above we further obtain

$$\begin{aligned}
[ABCD, Z] &= [(AB)(CD), Z] \\
&= (AB)[(CD), Z] - [E, (AB)](CD) \\
&= AB(C\{D, Z\} - \{Z, C\}D) + (A\{B, Z\} - \{Z, A\}B)CD
\end{aligned} \tag{A.11}$$

Therefore, making use of the commutator property in Eq.(A.11), we obtain, firstly for $[H, c_b^\dagger]$,

$$
\begin{aligned}
[H, c_b^\dagger] &= \left[\sum_{\alpha\beta} \left(h_{\alpha\beta} + d_{\alpha\beta}^i E^i(t) \right) c_\alpha^\dagger c_\beta + \frac{1}{2} \sum_{\alpha\beta\gamma\delta} V_{\gamma\delta}^{\alpha\beta} c_\alpha^\dagger c_\beta^\dagger c_\gamma c_\delta, c_b^\dagger \right] \\
&= \sum_{\alpha\beta} \left(h_{\alpha\beta} + d_{\alpha\beta}^i E^i(t) \right) \left[c_\alpha^\dagger c_\beta, c_b^\dagger \right] + \frac{1}{2} \sum_{\alpha\beta\gamma\delta} V_{\gamma\delta}^{\alpha\beta} \left[c_\alpha^\dagger c_\beta^\dagger c_\gamma c_\delta, c_b^\dagger \right] \\
&= \sum_{\alpha\beta} \left(h_{\alpha\beta} + d_{\alpha\beta}^i E^i(t) \right) \left(c_\alpha^\dagger \left\{ c_\beta, c_b^\dagger \right\} - \cancel{\left\{ c_b^\dagger, c_\alpha^\dagger \right\}} c_\beta \right) \\
&+ \frac{1}{2} \sum_{\alpha\beta\gamma\delta} V_{\gamma\delta}^{\alpha\beta} \left(c_\alpha^\dagger c_\beta^\dagger \left(c_\gamma \left\{ c_\delta, c_b^\dagger \right\} - \left\{ c_b^\dagger, c_\gamma \right\} c_\delta \right) + \left(c_\alpha^\dagger \cancel{\left\{ c_\beta^\dagger, c_b^\dagger \right\}} - \cancel{\left\{ c_b^\dagger, c_\alpha^\dagger \right\}} c_\beta^\dagger \right) c_\gamma c_\delta \right) \\
&= \sum_{\alpha\beta} \left(h_{\alpha b} + d_{\alpha\beta}^i E^i(t) \right) c_\alpha^\dagger \delta_{\beta b} \\
&+ \frac{1}{2} \sum_{\alpha\beta\gamma\delta} V_{\gamma\delta}^{\alpha\beta} \left(c_\alpha^\dagger c_\beta^\dagger c_\gamma \delta_{\delta b} - c_\alpha^\dagger c_\beta^\dagger \delta_{b\gamma} c_\delta \right)
\end{aligned}
\tag{A.12}
$$

Suppressing the summation over β, δ and γ, respectively, using the Kronecker delta and hiding the summations on repeated indices using Einstein's notation, we arrive at

$$
[H, c_b^\dagger] = \left(h_{\alpha b} + d_{\alpha b}^i E^i(t) \right) c_\alpha^\dagger + \frac{1}{2} V_{\gamma b}^{\alpha\beta} c_\alpha^\dagger c_\beta^\dagger c_\gamma - \frac{1}{2} V_{b\delta}^{\alpha\beta} c_\alpha^\dagger c_\beta^\dagger c_\delta \tag{A.13}
$$

Analogous for $[H, c_a]$, we have

$$
\begin{aligned}
[H, c_a] &= \left[\sum_{\alpha\beta} \left(h_{\alpha\beta} + d_{\alpha\beta}^i E^i(t) \right) c_\alpha^\dagger c_\beta + \frac{1}{2} \sum_{\alpha\beta\gamma\delta} V_{\gamma\delta}^{\alpha\beta} c_\alpha^\dagger c_\beta^\dagger c_\gamma c_\delta, c_a \right] \\
&= \sum_{\alpha\beta} \left(h_{\alpha\beta} + d_{\alpha\beta}^i E^i(t) \right) \left[c_\alpha^\dagger c_\beta, c_a \right] + \frac{1}{2} \sum_{\alpha\beta\gamma\delta} V_{\gamma\delta}^{\alpha\beta} \left[c_\alpha^\dagger c_\beta^\dagger c_\gamma c_\delta, c_a \right] \\
&= \sum_{\alpha\beta} \left(h_{\alpha\beta} + d_{\alpha\beta}^i E^i(t) \right) \left(c_\alpha^\dagger \cancel{\{c_\beta, c_a\}} - \{c_a, c_\alpha^\dagger\} c_\beta \right) \\
&+ \frac{1}{2} \sum_{\alpha\beta\gamma\delta} V_{\gamma\delta}^{\alpha\beta} \left(c_\alpha^\dagger c_\beta^\dagger \left(c_\gamma \cancel{\{c_\delta, c_a\}} - \cancel{\{c_a, c_\gamma\}} c_\delta \right) + \left(c_\alpha^\dagger \left\{ c_\beta^\dagger, c_a \right\} - \left\{ c_a, c_\alpha^\dagger \right\} c_\beta^\dagger \right) c_\gamma c_\delta \right) \\
&= - \sum_{\alpha\beta} \left(h_{\alpha\beta} + d_{\alpha\beta}^i E^i(t) \right) \delta_{a\alpha} c_\beta \\
&+ \frac{1}{2} \sum_{\alpha\beta\gamma\delta} V_{\gamma\delta}^{\alpha\beta} \left(c_\alpha^\dagger \delta_{\beta a} c_\gamma c_\delta - \delta_{a\alpha} c_\beta^\dagger c_\gamma c_\delta \right)
\end{aligned}
\tag{A.14}
$$

And finally,

$$
[H, c_a] = - \left(h_{a\beta} + d_{a\beta}^i E^i(t) \right) c_\beta + \frac{1}{2} V_{\gamma\delta}^{\alpha a} c_\alpha^\dagger c_\gamma c_\delta - \frac{1}{2} V_{\gamma\delta}^{a\beta} c_\beta^\dagger c_\gamma c_\delta \tag{A.15}
$$

A.3 Symmetry properties of the two-particle Hamiltonian blocks

We show the details on how to arrive at the symmetry properties of the resonant and coupling block of the effective two-particle Hamiltonian presented just above Eq.(2.53). For this we must recall the symmetry properties of the interaction matrix elements in Eqs.(2.10) and (2.11). Firstly, focusing on the diagonal term $H^{o_3e_4}_{o_1e_2}$, since the electrons are indistinguishable and interchangeable, we can rename the electrons $o_1e_2 \leftrightarrows o_2e_1$ and $o_3e_4 \leftrightarrows o_4e_3$. We obtain

$$\begin{aligned}
H^{o_3e_4}_{o_1e_2} &= (\epsilon_{o_1} - \epsilon_{e_2})\,\delta_{o_1o_3}\delta_{e_4e_2} - \left(V^{e_4o_1}_{e_2o_3} - W^{o_1e_4}_{e_2o_3}\right) \\
\Leftrightarrow H^{o_4e_3}_{o_2e_1} &= (\epsilon_{o_2} - \epsilon_{e_1})\,\delta_{o_2o_4}\delta_{e_3e_1} - \left(V^{e_3o_2}_{e_1o_4} - W^{o_2e_3}_{e_1o_4}\right) \\
&= (\epsilon_{e_2} - \epsilon_{o_1})\,\delta_{o_2o_4}\delta_{e_3e_1} - \left(\left(V^{e_1o_4}_{e_3o_2}\right)^* - \left(W^{e_1o_4}_{o_2e_3}\right)^*\right) \\
&= -\left[(\epsilon_{e_1} - \epsilon_{o_2})\,\delta_{o_2o_4}\delta_{e_3e_1} + \left(V^{e_1o_4}_{e_3o_2} - W^{e_1o_4}_{o_2e_3}\right)\right]^* \\
&= -\left(H^{e_3o_4}_{e_1o_2}\right)^*
\end{aligned} \tag{A.16}$$

Secondly and similarly for the off-diagonal term, we have

$$\begin{aligned}
H^{e_3o_4}_{o_1e_2} &= -\left(V^{o_4o_1}_{e_2e_3} - W^{o_1o_4}_{e_2e_3}\right) \\
\Leftrightarrow H^{e_4o_3}_{o_2e_1} &= -\left(V^{o_3o_2}_{e_1e_4} - W^{o_2o_3}_{e_1e_4}\right) \\
&= -\left[\left(V^{e_1e_4}_{o_3o_2}\right)^* - \left(W^{e_1e_4}_{o_2o_3}\right)^*\right] \\
&= -\left[V^{e_4e_1}_{o_2o_3} - W^{e_1e_4}_{o_2o_3}\right]^* \\
&= -\left(H^{o_3e_4}_{e_1o_2}\right)^*
\end{aligned} \tag{A.17}$$

Moreover, note that $H^{o_3e_4}_{e_1o_2}$ is symmetric,

$$\begin{aligned}
H^{o_3e_4}_{e_1o_2} &= V^{e_4e_1}_{o_2o_3} - W^{e_1e_4}_{o_2o_3} \\
&= V^{e_1e_4}_{o_3o_2} - W^{e_4e_1}_{o_3o_2} \\
&= H^{o_2e_1}_{e_4o_3} \\
&= \left(H^{o_3e_4}_{e_1o_2}\right)^T
\end{aligned} \tag{A.18}$$

further meaning that

$$H^{e_4o_3}_{o_2e_1} = -\left(H^{o_3e_4}_{e_1o_2}\right)^* = -\left(\left(H^{o_3e_4}_{e_1o_2}\right)^T\right)^* = -\left(H^{o_3e_4}_{e_1o_2}\right)^\dagger \tag{A.19}$$

Thus, the effective two-particle Hamiltonian has the final form

$$\boldsymbol{H}_{\text{e-h}} = \begin{bmatrix} H^{e_3o_4}_{e_1o_2} & H^{o_3e_4}_{e_1o_2} \\ -\left(H^{o_3e_4}_{e_1o_2}\right)^\dagger & -\left(H^{e_3o_4}_{e_1o_2}\right)^* \end{bmatrix} \tag{A.20}$$

Appendix B
Electron-electron interaction in quasi-2D systems

B.1 Rytova-Keldysh Potential

The purpose of this section is to discuss the formation of intralayer excitons in hBN as opposed to interlayer excitons. For intralayer excitons in 2D materials, the suitable choice of electrostatic potential is the Rytova-Keldish potential, as it provides a better description of the screening in a 2D material.

2D semiconductors are characterized by a 2D polarization. This, together with the fact that the electrostatic field lines are for the most of it outside the semiconductor makes the electrostatic potential different from the Coulomb interaction between two charges in a bulk.

The key to the derivation of the Rytova-Keldysh potential is the fact that the charge fluctuation are proportional to the Laplacian of the potential evaluated at the plane of the 2D material, which is assumed to be surrounded by vacuum for simplicity. Such a fact comes from the following considerations: the induced charge density, $\delta n_{2D}(\boldsymbol{r}_{||})$, due to a point charge located at a distance $\boldsymbol{r}$ from the system is given by the 2D polarization, $\boldsymbol{P}_{2D}$, in the usual way

$$\delta n_{2D}(\boldsymbol{r}_{||}) = -\nabla \cdot \boldsymbol{P}_{2D}, \tag{B.1}$$

where the 3D polarization vector is given by $\boldsymbol{r} = (\boldsymbol{r}_{||}, z)$, and δn_{2D} has units of charge per unit area. The polarization itself is proportional to the total electric field

$$\boldsymbol{P}_{2D} = -\varepsilon_0 \chi_{2D} \nabla_{||} \mathsf{V}(\boldsymbol{r}_{||}, z), \tag{B.2}$$

with χ_{2D} having dimensions of length. Therefore

$$\delta n_{2D}(\boldsymbol{r}_{||}) = +\varepsilon_0 \chi_{2D} \nabla_{||}^2 \mathsf{V}(\boldsymbol{r}_{||}, z) \tag{B.3}$$

Let us write Poisson's equation as

$$\nabla^2 \mathsf{V}(\boldsymbol{r}) = -\frac{e}{\varepsilon_0} \left[n_{2D,+} + n(\boldsymbol{r}) \right] \tag{B.4}$$

where $n_{2D,+}$ is the background positive charge density due to the atomic nuclei (in units of particles per area). We now write the electronic density (in units of particles per area) as

$$n(\boldsymbol{r}) = -n_{2D,-} + \delta(\boldsymbol{r}) + \delta(z)\Delta\sigma(\boldsymbol{r}_{||}) \tag{B.5}$$

where $n_{2D,-}$ is the neutralizing density of negative charge, $\delta(\boldsymbol{r})$ represents the density of a localized charge at position $\boldsymbol{r}$, and $\delta(z)\Delta\sigma(\boldsymbol{r}_{||})$ is the induced charge density fluctuation in the 2D material. With this definitions, Poisson's equation reads

$$\begin{aligned}\nabla^2\mathsf{V}(\boldsymbol{r}) &= -\frac{e}{\varepsilon_0}\left[\cancel{n_{2D,+} = n_{2D,-}} + \delta(\boldsymbol{r}) + \delta(z)\Delta\sigma(\boldsymbol{r}_{||})\right] \\ &= -\frac{e}{\varepsilon_0}\delta(\boldsymbol{r}) - -\frac{1}{\varepsilon_0}\delta(z)\left(e\Delta\sigma(\boldsymbol{r}_{||})\right)\end{aligned} \tag{B.6}$$

Since

$$e\Delta\sigma(\boldsymbol{r}_{||}) = \delta n_{2D}(\boldsymbol{r}_{||}) \tag{B.7}$$

we have that

$$\nabla^2\mathsf{V}(\boldsymbol{r}) = -\frac{e}{\varepsilon_0}\delta(\boldsymbol{r}) - \frac{1}{\varepsilon_0}\delta(z)\left(\varepsilon_0\chi_{2D}\nabla_{||}\mathsf{V}(\boldsymbol{r}_{||}, z)\right) \tag{B.8}$$

and thus

$$\nabla^2\mathsf{V}(\boldsymbol{r}) = -\frac{e}{\varepsilon_0}\delta(\boldsymbol{r}) - \delta(z)\chi_{2D}\nabla_{||}^2\mathsf{V}(\boldsymbol{r}_{||}, 0) \tag{B.9}$$

Fourier transforming the previous equation yields

$$(i\boldsymbol{k})^2\mathsf{V}(\boldsymbol{k}) = -\frac{e}{\varepsilon_0} - \chi_{2D}(ik_{||})^2\mathsf{V}(\boldsymbol{k}_{||}, 0) \tag{B.10}$$

Since $\boldsymbol{k} = (\boldsymbol{k}_{||}, k_z)$ we obtain

$$-(k_{||}^2 + k_z^2)\mathsf{V}(\boldsymbol{k}) = -\frac{e}{\varepsilon_0} + k_{||}^2\chi_{2D}\mathsf{V}(\boldsymbol{k}_{||}, 0) \tag{B.11}$$

Solving for $\mathsf{V}(\boldsymbol{k})$, we find

$$\mathsf{V}(\boldsymbol{k}) = \frac{e}{\varepsilon_0}\frac{1}{(k_{||}^2 + k_z^2)} - \frac{k_{||}^2}{(k_{||}^2 + k_z^2)}\chi_{2D}\mathsf{V}(\boldsymbol{k}_{||}, 0) \tag{B.12}$$

Inverse Fourier transforming k_z back into the real space we obtain

$$\int_{-\infty}^{+\infty}\frac{dk_z}{2\pi}e^{ik_z z}\mathsf{V}(\boldsymbol{k}_{||}, k_z) = \int_{-\infty}^{+\infty}\frac{dk_z}{2\pi}e^{ik_z z}\left(\frac{e}{\varepsilon_0}\frac{1}{(k_{||}^2 + k_z^2)} - \frac{k_{||}^2}{(k_{||}^2 + k_z^2)}\chi_{2D}\mathsf{V}(\boldsymbol{k}_{||})\right) \tag{B.13}$$

where the integral $\int dk_z e^{ik_z z}/(k_{||}^2 + k_z^2)$ can be solve in the complex plane with a semi-circular loop around the upper plane and applying the residue theorem on the pole $k_z = +ik_{||}$. We obtain

$$\begin{aligned}\int_{-\infty}^{+\infty} dk_z \frac{e^{ik_z z}}{(k_{||}^2 + k_z^2)} &= 2\pi i \lim_{k_z \to +ik_{||}} \left((k_z - ik_{||}) \frac{e^{ik_z z}}{(k_z + ik_{||})(k_z - ik_{||})} \right) \\ &= 2\pi i \frac{e^{-k_{||} z}}{2ik_{||}} \\ &= \pi \frac{e^{-k_{||} z}}{k_{||}} \end{aligned} \tag{B.14}$$

Defining

$$\mathsf{V}(\boldsymbol{k}_{||}, z) = \int_{-\infty}^{+\infty} \frac{dk_z}{2\pi} e^{ik_z z} \mathsf{V}(\boldsymbol{k}_{||}, k_z) \tag{B.15}$$

and substituting (B.14) into (B.13) we obtain

$$\mathsf{V}(\boldsymbol{k}_{||}, z) = \frac{1}{2\pi} \left(\frac{e}{\varepsilon_0} \left(\pi \frac{e^{-k_{||} z}}{k_{||}} \right) - k_{||}^2 \left(\pi \frac{e^{-k_{||} z}}{k_{||}} \right) \chi_{2D} \mathsf{V}(\boldsymbol{k}_{||}) \right) \tag{B.16}$$

Putting $z = 0$ we further obtain

$$\mathsf{V}(\boldsymbol{k}_{||}) = \frac{e}{2\varepsilon_0 k_{||}} - k_{||} \frac{\chi_{2D}}{2} \mathsf{V}(\boldsymbol{k}_{||}) \tag{B.17}$$

Defining $r_0 \equiv 1/\kappa_{||} = \chi_{2D}/2$ as the effective screening radius and solving for $\mathsf{V}(\boldsymbol{k}_{||})$ yields

$$\mathsf{W}(\boldsymbol{k}_{||}) = \frac{e}{2\varepsilon_0} \frac{1}{k_{||}} \frac{1}{1 + r_0 k_{||}} \tag{B.18}$$

where we use W instead of the the generic V. The solution to this integral is known as the *Rytova-Keldish potential*, and this repulsive potential represents the interaction among the electrons in a polarizable 2D semiconductor.

B.2 Screened Rytova-Keldysh Potential (2D dielectric-metal interface)

As a follow-up of the previous section, consider the case where the 2D semiconductor in no longer surrounded by vacuum but is instead inside a dielectric which is in close contact with a metal such that there is a distance d between the 2D material and the metal, as depicted in Fig.(20).

To obtain the effective electron-hole interaction, which will translate in a screened Rytova-Keldysh potential, we need to solve once more the Poisson equation (B.4) but taking into account the interface boundary conditions satisfied by the electromagnetic fields between the dielectric ε_d and the metal ε_m,

$$\boldsymbol{E}_m \cdot \hat{\boldsymbol{r}}_{||} - \boldsymbol{E}_d \cdot \hat{\boldsymbol{r}}_{||} = 0, \tag{B.19}$$

$$\boldsymbol{B}_m \cdot \hat{\boldsymbol{z}} - \boldsymbol{B}_d \cdot \hat{\boldsymbol{z}} = 0, \tag{B.20}$$

with $\hat{\boldsymbol{z}}$ the unit normal to the interface and $\hat{\boldsymbol{r}}_{||}$ the unit vector tangent to the interface. Consider a point charge $-e$ on top of the 2D material at $\boldsymbol{r} = \boldsymbol{0}$. The electronic density as described in Eq.(B.5) has two additional volumetric bound terms corresponding to the charges within the dielectric and the metal, reading

$$\begin{aligned} n(\boldsymbol{r}) = &-n_{2D,-} + \delta(\boldsymbol{r}) + \delta(z)\Delta\sigma(\boldsymbol{r}_{||}) \\ &+ n_d(\boldsymbol{r}_{||}, z)\left[\Theta(z+d) - \Theta(z-h)\right] \\ &+ n_m(\boldsymbol{r}_{||}, z)\left[\Theta(-(z+d))\right] \end{aligned} \tag{B.21}$$

where Θ is the Heaviside function. As done for the isolated 2D material, supposing linear mediums without non-local effects, the relation between the induced charges and the potential yields

$$n_i(\boldsymbol{r}) = +\varepsilon_0 \chi_i \nabla_{||}^2 \mathsf{V}(\boldsymbol{r}_{||}, z) \tag{B.22}$$

with χ_i the medium $i = d, m$ susceptibility. Following the same steps as before but having in mind this two extra terms, after performing the 2D Fourier transform over the parallel component, $\mathsf{V}(\boldsymbol{k}_{||}, z) \equiv \tilde{\mathsf{V}}$, the Poisson equations reads

$$\begin{aligned} \left((ik_{||})^2 + \partial_z^2\right)\tilde{\mathsf{V}} = &-\frac{e}{\varepsilon_0}\delta(z) - \chi_{2D}(ik_{||})^2\tilde{\mathsf{V}}\delta(z) \\ &- \chi_d\left((ik_{||})^2 + \partial_z^2\right)\tilde{\mathsf{V}}\left[\Theta(z+d) - \Theta(z-h)\right] \\ &- \chi_m\left((ik_{||})^2 + \partial_z^2\right)\tilde{\mathsf{V}}\left[\Theta(-(z+d))\right] \end{aligned} \tag{B.23}$$

Since we know how to solve this equation inside each respective isolated medium, we make the plane-wave ansatz

$$\mathsf{V}(\boldsymbol{k}_{||}, z) = \begin{cases} Ae^{k_{||}z} & \text{, if } z < -d \\ Be^{k_{||}z} + Ce^{-k_{||}z} & \text{, if } -d \leq z \leq 0 \\ De^{k_{||}z} + Ee^{-k_{||}z} & \text{, if } 0 < z < h \\ Fe^{-k_{||}z} & \text{, if } z > h \end{cases} \tag{B.24}$$

and solve for the coefficients A through F. For this, we first integrate Eq.(B.23) in $\hat{z}$ in a wafer-thin slice

of length $\eta \to 0$ "around" each respective interface. Firstly, integrating from $-d-\eta$ to $-d+\eta$ yields

$$
\begin{aligned}
&-\partial_z \tilde{\mathrm{V}}\big|_{-d-\eta}^{-d+\eta} = -\chi_m \partial_z \tilde{\mathrm{V}}(z=-d-\eta) - \left(-\chi_d \partial_z \tilde{\mathrm{V}}(z=-d+\eta)\right) \\
\Rightarrow &-\left(Bk_{||}e^{-k_{||}d} - C(-k_{||})e^{+k_{||}d} - Ak_{||}e^{-k_{||}d}\right) = -\chi_m A k_{||} e^{-k_{||}d} + \chi_d (Bk_{||}e^{-k_{||}d} + C(-k_{||})e^{+k_{||}d}) \\
\Leftrightarrow &-B + Ce^{2k_{||}d} + A = -\chi_m A + \chi_d (B - Ce^{2k_{||}d}) \\
\Leftrightarrow &A(1+\chi_m) - (B - Ce^{2k_{||}d})(1+\chi_d) = 0
\end{aligned} \tag{B.25}
$$

Similarly, integrating instead from $-\eta$ to $+\eta$ yields

$$
\begin{aligned}
&-\partial_z \tilde{\mathrm{V}}\big|_{-\eta}^{+\eta} = -\frac{e}{\varepsilon_0} + \chi_{2D}(ik_{||})^2 \tilde{\mathrm{V}}(z=0) - \chi_d \partial_z \tilde{\mathrm{V}}(z=-\eta) - \left(-\chi_d \partial_z \tilde{\mathrm{V}}(z=+\eta)\right) \\
\Rightarrow &-\left((D-E)\,k_{||} - (B-C)\,k_{||}\right) = -\frac{e}{\varepsilon_0} - \chi_{2D} {k_{||}}^2 (B+C) - \chi_d (B-C)\,k_{||} + \chi_d (D-E)\,k_{||} \\
\Leftrightarrow &-D + E + B - C = -\frac{e}{\varepsilon_0}\frac{1}{k_{||}} - \chi_{2D} k_{||} (B+C) - \chi_d (B-C) + \chi_d (D-E) \\
\Leftrightarrow &B(1+\chi_{2D}k_{||} + \chi_d) + C(-1+\chi_{2D}k_{||} - \chi_d) - (D-E)(1+\chi_d) = -\frac{e}{\varepsilon_0}\frac{1}{k_{||}}
\end{aligned} \tag{B.26}
$$

And lastly, integrating from $h-\eta$ to $h+\eta$ yields

$$
\begin{aligned}
&-\partial_z \tilde{\mathrm{V}}\big|_{h-\eta}^{h+\eta} = -\chi_d \partial_z \tilde{\mathrm{V}}(z=h-\eta) \\
\Rightarrow &-\left(F(-k_{||})e^{-k_{||}h} - \left(Dk_{||}e^{k_{||}h} + E(-k_{||})e^{-k_{||}h}\right)\right) = -\chi_d \left(Dk_{||}e^{k_{||}h} + E(-k_{||})e^{-k_{||}h}\right) \\
\Leftrightarrow &F + De^{2k_{||}h} - E = -\chi_d D e^{2k_{||}h} + \chi_d E \\
\Leftrightarrow &F + (De^{2k_{||}h} - E)(1+\chi_d) = 0
\end{aligned} \tag{B.27}
$$

Thus, to find the coefficients A through F one needs to solve the system of equations

$$A(1+\chi_m) - (B - Ce^{2k_{||}d})(1+\chi_d) = 0 \tag{B.28}$$

$$B(1+\chi_{2D}k_{||} + \chi_d) + C(-1+\chi_{2D}k_{||} - \chi_d) - (D-E)(1+\chi_d) = -\frac{e}{\varepsilon_0}\frac{1}{k_{||}} \tag{B.29}$$

$$F + (De^{2k_{||}h} - E)(1+\chi_d) = 0, \tag{B.30}$$

together with the tangential continuity of the electric field at the interfaces,

$$Ae^{-k_{||}d} - (Be^{-k_{||}d} + Ce^{k_{||}d}) = 0, \tag{B.31}$$

$$(B+C) - (D+E) = 0, \tag{B.32}$$

$$(De^{k_{||}h} + Ee^{-k_{||}h}) - Fe^{-k_{||}h} = 0. \tag{B.33}$$

Directly from the system of equations we have,

$$Fe^{-k_{||}h} = -(1+\chi_d)\left(De^{k_{||}h} - Ee^{-k_{||}h}\right) \tag{B.34}$$

$$Fe^{-k_{||}h} = De^{k_{||}h} + Ee^{k_{||}h} \tag{B.35}$$

meaning that

$$D = \frac{\chi_d}{2+\chi_d} e^{-2k_{||}h} E \equiv G_d(k_{||}) E \tag{B.36}$$

where we defined a new function $G_d(k_{||})$. Also directly from the system of equations, we have

$$(1+\chi_m)\, A e^{-k_{||}d} = (1+\chi_d)\left(B e^{-k_{||}d} - C e^{k_{||}d}\right) \tag{B.37}$$

$$A e^{-k_{||}d} = B e^{-k_{||}d} + C e^{k_{||}d} \tag{B.38}$$

and thus

$$C = -\frac{\chi_m - \chi_d}{1+\chi_d+\chi_m} e^{-2k_{||}d} B \equiv G_m(k_{||}) B \tag{B.39}$$

where, once again, we defined another new function$G_m(k_{||})$ related to $G_d(k_{||})$ via

$$\left(1+G_m(k_{||})\right) B = \left(1+G_d(k_{||})\right) E \tag{B.40}$$

We obtain

$$\begin{aligned} &\left(1+\chi_{2D}k_{||}+\chi_d\right) B + \left(-1+\chi_{2D}k_{||}-\chi_1\right) G_m(k_{||}) B + \left(-1-\chi_d\right) G_d(k_{||}) E + \left(1+\chi_d\right) E = -\frac{1}{k_{||}} \frac{e}{\varepsilon_0} \\ \Rightarrow &\left[1+\chi_{2D}k_{||}+\chi_1 + \left(-1+\chi_{2D}k_{||}-\chi_d\right) G_m(k_{||}) + \left(1+\chi_d\right)\left(1-G_d(k_{||})\right) \frac{1+G_m(k_{||})}{1+G_d(k_{||})}\right] B = -\frac{1}{k_{||}} \frac{e}{\varepsilon_0} \end{aligned} \tag{B.41}$$

resulting in the potential

$$\tilde{\mathsf{V}} = B + C = \frac{-e}{k_{||}\varepsilon_0 \varepsilon_d} \left[\frac{\chi_{2D}k_{||}}{\varepsilon_d} + \frac{2 - G_d(k_{||}) G_m(k_{||})}{\left(1+G_d(k_{||})\right)\left(1+G_m(k_{||})\right)}\right]^{-1} \tag{B.42}$$

Now, in the special case of a 3D perfect metal, $\chi_m \to -\infty$, we have that

$$G_m(k_{||}) = -\frac{\chi_m - \chi_d}{1+\chi_d+\chi_m} e^{-2k_{||}d} \approx -\frac{\chi_m}{\chi_m} e^{-2k_{||}d} = -e^{-2k_{||}d} \tag{B.43}$$

and in the special case of the dielectric being actually a vacuum, $\chi_d = 0$ we have that

$$G_d(k_{||}) = \frac{\chi_d}{2+\chi_d} e^{-2k_{||}h} = -e^{-2k_{||}h} \tag{B.44}$$

In this cases, the effective potential, corresponding to the screened Rytova-Keldysh potential yields

$$\mathsf{V}(\boldsymbol{k}_{||}) = \frac{e}{2\varepsilon_0} \frac{1}{k_{||}} \frac{1}{r_0 k_{||} + \frac{1}{2}\frac{e^{k_{||}d}}{\sinh(k_{||}d)}} \tag{B.45}$$

This work was supported by Fundação para a Ciência e a Tecnologia, I.P., (FCT-Portugal) through the project EXPL/FIS-MAC/0953/2021.